GEORG-AUGUST-UNIVERSITÄT GÖTTINGEN IN PUBLICA COMMODA SEIT 1737

INSTITUT FÜR ASTROPHYSIK & GEOPHYSIK

3D Modelling of Coronal Mass Ejections and Simulation of Their Earthward Evolution – Developing Space Weather Forecasting Approaches for the ESA Vigil Mission

Abschlussarbeit im Rahmen der Prüfung
im Studiengang Physik (M.Sc.)
an der Georg-August-Universität Göttingen

vorgelegt am: 17.03.2025

von: Enno Müller
aus: Neubrandenburg

1. Gutachter: Dr. V. Bothmer
2. Gutachter: Prof. Dr. A. Reiners

Georg-August-Universität Göttingen
Institut für Astrophysik und Geophysik

Abstract

Coronal mass ejections (CMEs) are massive eruptions of solar plasma and magnetic fields. Their interplanetary counterparts, interplanetary coronal mass ejections (ICMEs), can trigger severe geomagnetic storms when Earth-directed. These storms pose significant risks to modern infrastructure such as power grids and satellite communications, highlighting the importance of developing forecasting approaches predicting arrival times with high accuracy. Single-viewpoint reconstructions of CME events are more vulnerable to misinterpretation due to projection effects, as demonstrated by the 2010-04-08 event, where the signatures of several events overlap. This underscores the necessity of multi-perspective observations to resolve event complexity—a challenge addressed in this work through rigorous event selection criteria isolating CME-ICME pairs showing minimal interaction with other phenomena, enabling a controlled assessment of model performance. By integrating multi-viewpoint coronagraph data from the Solar TErrestrial RElations Observatory (STEREO) and Solar and Heliospheric Observatory (SOHO) spacecraft with drag-based propagation models, this framework combines three dimensional (3D) Graduated Cylindrical Shell (GCS) reconstructions and Earthward-directed velocity calculations with evaluations of two propagation approaches: the established Drag-Based Model (DBM) and a novel Modified Drag-Based Model (MoDBM) incorporating updated solar wind density and speed profiles (Venzmer and Bothmer, 2018). Applied to five events, the models achieve mean absolute arrival-time errors of 3.73 h (DBM) and 3.84 h (MoDBM), surpassing the 9.8 ± 2.0 h benchmark (Vourlidas et al., 2019) under controlled conditions. Uncertainties in reconstruction parameters and propagation models are discussed. Though limited by sample size, the results validate the potential of the future European Space Agency (ESA) Vigil mission's Lagrange point 5 (L_5) perspective. By aligning with the mission's monitoring capabilities, the developed approaches provide an almost-complete foundation for operational forecasting.

Contents

List of Figures

List of Tables

List of Abbreviations

L_1	Lagrange Point 1
L_4	Lagrange Point 4
L_5	Lagrange Point 5
1D	One Dimensional
2D	Two Dimensional
3D	Three Dimensional
ACE	Advanced Composition Explorer
AU	Astronomical Unit
C1	LASCO Coronagraph 1
C2	LASCO Coronagraph 2
C3	LASCO Coronagraph 3
CAT	CME Analysis Tool
CCD	Charge-Coupled Device
CCOR	Compact CORonagraph
CME	Coronal Mass Ejection
COR1	STEREO/SECCHI CORonagraph 1
COR2	STEREO/SECCHI CORonagraph 2
COR2A	COR2 on board STA
COR2B	COR2 on board STB
CSHKP	Carmichael-Sturrock-Hirayama-Kopp-Pneuman
DBM	Drag-Based Model
DSCOVR	Deep Space Climate Observatory
EAR	Earthward-directed height to Apex-directed height Ratio
EPACT	Energetic Particles: Acceleration, Composition and Transport
ESA	European Space Agency
EUVI	Extreme UltraViolet Imager
FOV	Field of View
GCS	Graduated Cylindrical Shell
GSM	geocentric solar magnetospheric
GUI	Graphical User Interface
HI	Heliospheric Imager
ICC	Ice-Cream Cone
ICME	Interplanetary Coronal Mass Ejection
ID	IDentification

IDL	Interactive Data Language
INSTANT	INvestigation of Solar-Terrestrial Activity aNd Transients
KG event list	Kay and Gopalswamy's event list
LASCO	Large Angle and Spectrometric COronagraph
MAG	MAGnetometer
MFI	Magnetic Field Investigation
MHD	MagnetoHydroDynamics
MoDBM	Modified Drag-Based Model
NASA	National Aeronautics and Space Administration
ODE	Ordinary Differential Equation
OSO-7	Orbiting Solar Observatory 7
PLA	PLasma Analyzer
PMI	Photospheric Magnetic field Imager
RC ICME list	Richardson and Cane's ICME list
SDO	Solar Dynamics Observatory
SECCHI	Sun-Earth Connection Coronal and Heliospheric Investigation
SEP	Solar Energetic Particle
SMS	Solar Wind and Suprathermal Ion Composition Experiment
SOHO	SOlar and Heliospheric Observatory
SSN	international SunSpot Number
STA	STEREO-Ahead
STB	STEREO-Behind
STEREO	Solar TErrestrial RElations Observatory
ToA	Time of Arrival
UC	Use Case
UT	Universal Time

1 Introduction

Coronal mass ejections (CMEs) are among the most significant solar phenomena, consisting of large-scale eruptions of plasma and magnetic fields from the Sun's corona into the heliosphere. Their discovery in 1971 by the Orbiting Solar Observatory 7 (OSO-7) satellite (Tousey, 1973) marked the beginning of extensive international research efforts into their origins, properties, and impact on space weather (Howard et al., 2023). Since then, thousands of CMEs have been observed using coronagraphs on board space missions, relying on Thomson scattering to detect these optically thin structures (Chen, 2011).

The connection between CMEs and their interplanetary counterparts, interplanetary coronal mass ejections (ICMEs), was first established in 1980 when Helios 1 detected an ICME that had originated from a CME observed two days earlier by the Solwind coronagraph aboard P78-1 (Burlaga et al., 1982). The dynamics of ICMEs depend, e.g., on their interaction with the ambient solar wind, leading to either acceleration or deceleration depending on their relative speed (Vršnak et al., 2013). In-situ observations allow for their characterisation through plasma and magnetic field properties, elemental composition, and energetic particle behaviour (Gosling, 1990).

Understanding and forecasting ICMEs is a central goal of space weather research due to their role as the primary drivers of major geomagnetic storms on Earth (Bothmer and Schwenn, 1998). Their occurrence frequency follows the 11-year solar cycle (Webb and Howard, 1994), and their potential to disrupt modern technological systems—including GPS, power grids, aviation, and space missions—has made their study increasingly relevant (Bothmer and Zhukov, 2007). Accurate forecasting of ICME arrival times and properties is critical to mitigating their impacts (Siscoe et al., 2007).

Space weather forecasting has traditionally relied on single-viewpoint observations, particularly from Lagrange point 1 (L_1) along the Sun-Earth line, due to the availability of continuous measurements from this vantage point. The Solar and Heliospheric Observatory (SOHO) satellite (Domingo et al., 1995) positioned in a Halo orbit around L_1, although not conceptualised as a space weather mission, has been instrumental in providing near real-time CME imagery. However, relying on a single perspective introduces projection effects that can distort CME parameters (Burkepile et al., 2004; Schwenn, 2006). Studies have shown that disk events observed from a single viewpoint can lead to overestimations of CME mass (Pluta et al., 2018), width, and an underestimation of their speeds (Burkepile et al., 2004).

The launch of the Solar TErrestrial RElations Observatory (STEREO) mission in 2006 (Kaiser et al., 2008) significantly advanced CME research by providing multi-viewpoint observations from two nearly identical spacecraft orbiting the Sun at slightly different distances. Figure 1 presents a CME event observed by both spacecraft simultaneously.

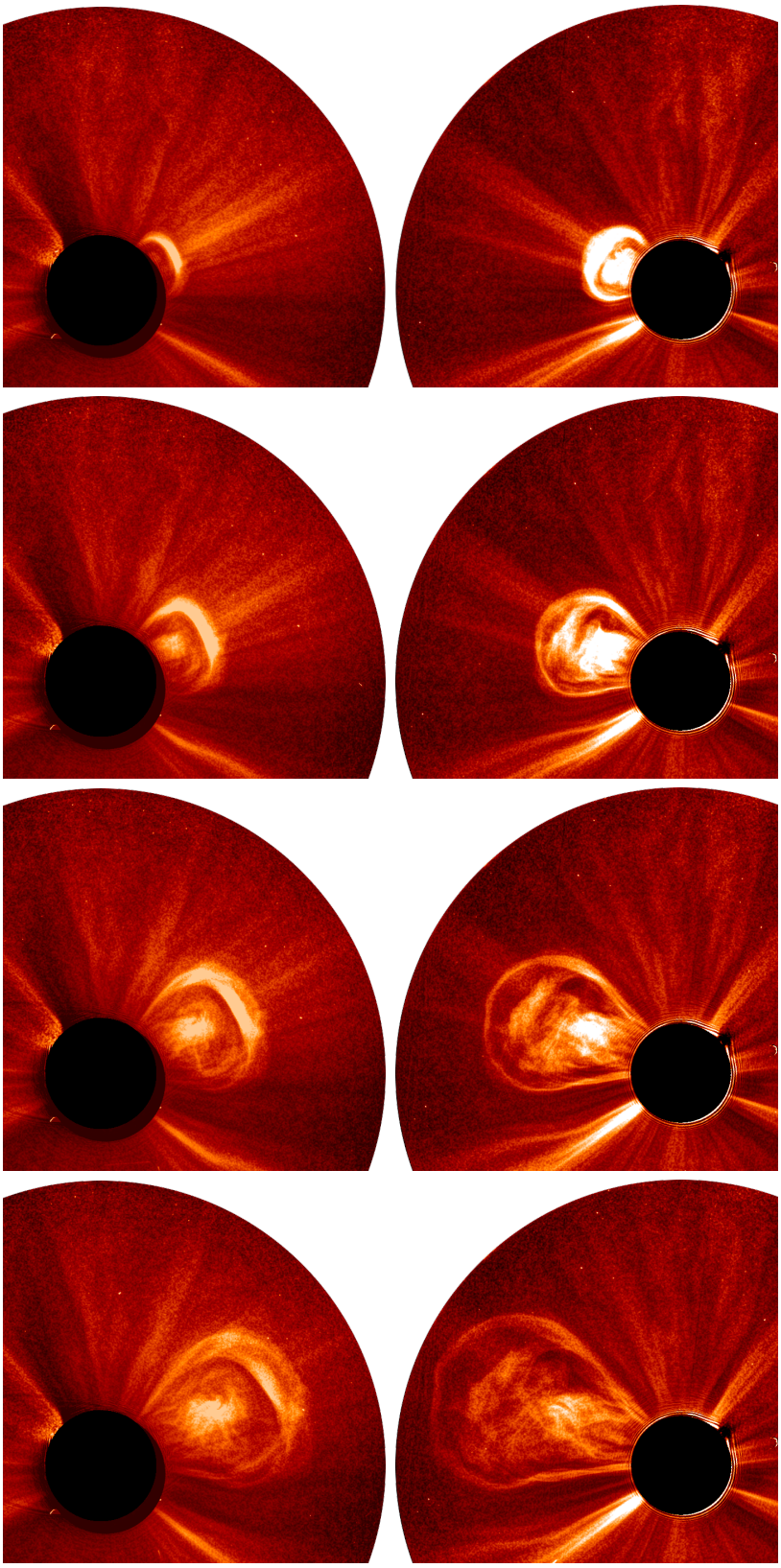

Figure 1: Coronagraph images of a CME event on September 14, 2011, captured simultaneously by STB (left panels) and STA (right panels). The rows show the images taken at 00:24 UT, 01:24 UT, 02:24 UT, and 03:24 UT (top to bottom). The sequence highlights the evolution of the CME as observed from two vantage points. The images were obtained and processed using JHelioviewer[3].

This mission enabled the first-ever full view of the Sun and drastically improved the accuracy of CME speed, as well as CME width and mass (Colaninno and Vourlidas, 2009) estimations. By reducing dependence on L_1 data, it also greatly aided in advancing space weather forecasting (Howard et al., 2023).

A promising future development in space weather monitoring is the upcoming European Space Agency (ESA) Vigil mission, formerly 'Lagrange', set to launch in the early 2030s. Mission concepts were proposed by, for example, Schmidt and Bothmer (1996) and Lavraud et al. (2016). Positioned at Lagrange point 5 (L_5), approximately 60° behind Earth, Vigil will provide an additional perspective that complements near-Earth observations, allowing for more accurate three dimensional (3D) reconstructions of CMEs, particularly when combined with other viewpoints. Separation angles of at least 10° have been identified as particularly beneficial for 3D reconstructions (Bosman, 2017, p. 91). Moreover, Vigil's vantage point will offer 4–5 days' advance warning of active regions rotating into Earth view, enhancing space weather forecasting capabilities.

Space weather forecasting can greatly benefit from forecasting approaches that combine CME reconstruction techniques and ICME propagation models to enhance prediction accuracy. These two steps involve distinct but complementary methodologies. Reconstruction models focus on deriving key CME parameters such as velocity, orientation, and spatial extent, with the Graduated Cylindrical Shell (GCS) model (Thernisien et al., 2006) being a widely used approach for characterising their 3D large-scale morphology. Its adaptability to multi-viewpoint data, supported by tools like 'GCS in Python' (Forstner, 2024), enhances its applicability for comprehensive reconstructions. The extracted parameters then serve as inputs for ICME propagation models, which estimate metrics such as arrival times and geoeffectiveness based on solar wind interactions and heliospheric conditions. By refining both aspects independently and integrating them effectively, space weather forecasting can achieve greater precision and reliability.

Different approaches exist for modelling ICME propagation through the heliosphere, ranging from empirical to physics-based and probabilistic frameworks. Among them, the Drag-Based Model (DBM) (Vršnak et al., 2013) has gained prominence due to its observational grounding and analytical formulation. This model provides a practical means of estimating ICME kinematics by accounting for interactions with the ambient solar wind. Enhancements to such models continue to refine space weather predictions by incorporating recent findings, including the variable nature of the solar wind and its influence on ICME dynamics. Further improvements can be achieved by integrating a more detailed representation of the solar wind structure, distinguishing between fast and slow wind regimes, and refining the dependence of solar wind proton density on radial distance from the Sun (Venzmer and Bothmer, 2018).

Quantitative evaluation of forecasting methods relies on comparisons between predicted ICME arrival times and in-situ solar wind measurements near Earth. In-situ measure-

ments provided by the WIND (Acuña et al., 1995) and Advanced Composition Explorer (ACE) (Stone et al., 1998) spacecraft at L_1 deliver high-resolution plasma and magnetic field data that allow for the detailed identification of ICMEs. Comparisons between predicted and observed arrival times offer a valuable benchmark for assessing model performance and guiding improvements in space weather forecasting (Vourlidas et al., 2019).

Selecting events that are suitable for evaluation of CME reconstruction and ICME forecasting methods is crucial. In particular, it is important to address common challenges more complex CME events might pose to the modelling and evaluation process. Between 2019 and 2023, ESA conducted a study on "Use of L5 Data in CME Propagation Models", which was coordinated by RAL Space (UKRI STFC) and successfully completed. It aimed to assess the benefits of incorporating additional viewpoints into space weather forecasting. I had the opportunity to participate in this study, with Dr. V. Bothmer leading the German contribution. During the study, we encountered significant difficulties when analysing events featuring more complex processes, such as multiple difficult-to-distinguish CMEs being observed. In some cases, this led to the nature of these events being misinterpreted, making it difficult to compare analyses and reducing the reliability of the evaluations.

This finding highlights the importance of carefully selecting events when assessing forecasting methods. Challenges such as multiple CMEs overlapping in coronagraphic images or having to account for interactions between multiple CMEs and ICMEs can make analysis more difficult. However, these complexities are often overlooked in existing event catalogues (e.g., near-Earth ICME list by Richardson and Cane (2024) or the 45-event dataset by Kay and Gopalswamy (2017)). These limitations suggest the need for better strategies and raise new scientific questions about how uncertainties affect the evaluation of forecasting approaches.

The integration of multi-viewpoint reconstructions with propagation models offers a promising path toward refining space weather predictions and mitigating the risks posed by solar transients. Leveraging advanced modelling techniques alongside an evaluation framework that distinguishes inherent model limitations from event-specific complexities not only aligns with the prospective use of data from future missions like Vigil, but also lays the foundation for more robust and reliable forecasting strategies to protect critical technological infrastructures.

This work is structured as follows: Chapter 2 provides an overview of the Sun's structure, including its basic characteristics and key solar phenomena. Chapter 3 introduces CMEs, covering their fundamental properties, observational features, and modelling approaches. Chapter 4 discusses relevant space missions and instrumentation used for remote and in-situ observations, with a focus on coronagraphs. The motivation for this study is outlined in Chapter 5, followed by a detailed description of the event selection process

in Chapter 6. Chapter 7 presents the methodology for event analysis, including 3D geometric modelling and propagation modelling techniques. The results and discussion are provided in Chapter 8, examining the selected events, modelling outcomes, and forecasted ICME arrival times. Finally, Chapter 9 summarises the key findings and provides an outlook on future research directions.

2 The Sun, its Structure and Solar Phenomena

To establish necessary context for this work, which focuses on the analysis of solar phenomena, particularly CMEs and ICMEs, fundamental aspects of the Sun—including its basic characteristics, structure, atmosphere, and activity phenomena—are introduced in this chapter.

2.1 Basic Characteristics

Classified as a G2V-type star, the Sun resides on the main sequence with a yellow hue and an absolute magnitude of 4.8. Approximately 4.6 billion years ago, its formation commenced through the gravitational collapse of an interstellar molecular cloud (Connelly et al., 2012). Over the next five billion years, hydrogen depletion will trigger thermonuclear fusion in a shell surrounding its core, leading to expansion to $166\,\mathrm{R}_\odot$. Ultimately, after losing substantial mass, the Sun will contract into an Earth-sized white dwarf roughly 12.5 billion years from now[1].

Table 1: List of basic parameters concerning the Sun. From Stix (2004, p. 2-9) and Carroll and Ostlie (2006, p. 364).

Quantity	Value
Distance to Earth	$1\,\mathrm{AU} = 149597870(2)\,\mathrm{km}$
Mass	$1\,\mathrm{M}_\odot = 1.9889(3) \cdot 10^{30}\,\mathrm{kg}$
Radius	$1\,\mathrm{R}_\odot = 696342\,\mathrm{km}$
Density	$\bar{\rho} = 1.408\,\mathrm{g\,cm^{-2}}$
Surface gravitation	$g_\odot = 274\,\mathrm{m\,s^{-2}}$
Solar constant	$S = 1367(3)\,\mathrm{W\,m^{-2}}$
Luminosity	$L_\odot = 3.844(10) \cdot 10^{26}\,\mathrm{W}$
Composition	92.1% H, 7.8% He and 0.1% Metals
Surface Temperature	$T_{\mathrm{eff}} = 5778(3)\,\mathrm{K}$
Rotation Period	25 d (Equator), 36 d (Poles)

Accurate models describing the Sun—critical for interpreting observations and solar phenomena—rely on precise parameter values. Advances in observational techniques have refined these measurements significantly, as summarised in Table 1. Notably, the mean Earth-Sun distance defines the Astronomical Unit (AU), a number used widely across heliophysical studies.

2.2 The Structure of the Sun

Compressed by self-gravitation, the Sun's high-temperature plasma spans multiple structural layers defined by energy transport mechanisms and magnetohydrodynamic

[1] Article by David Taylor (last accessed March 2025): https://faculty.wcas.northwestern.edu/infocom/The%20Website/end.html.

properties (Kivelson and Russell, 1995), and even beyond its atmosphere. As illustrated in Figure 2, these include the core, radiative zone, tachocline, convection zone, photosphere, chromosphere, transition region, and corona. Each region exhibits distinct thermodynamic behaviours.

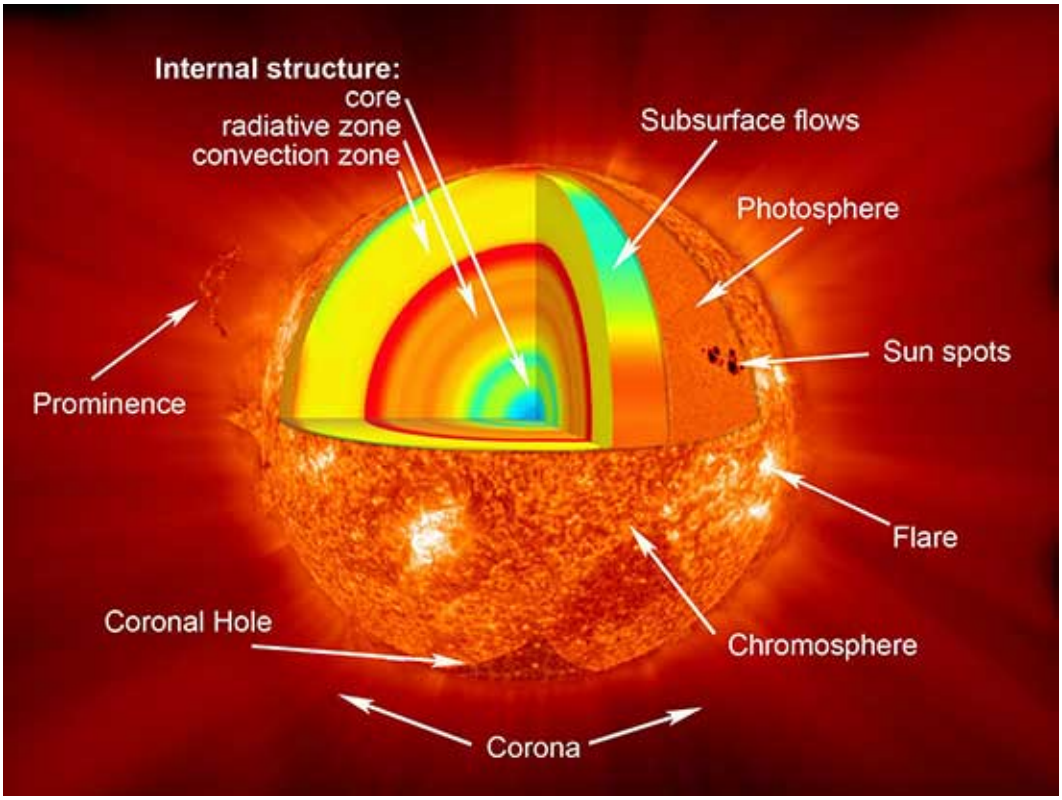

Figure 2: A schematic illustration depicting the various components of the Sun and associated solar phenomena. The diagram presents both the Sun's internal structure—comprising the core, radiative zone, and convection zone—as well as its external layers, including the photosphere, chromosphere, and corona. Additionally, solar features such as sunspots, coronal holes, flares, and prominences are highlighted. From NASA, https://imagine.gsfc.nasa.gov/science/objects/sun1.html (last accessed March 2025).

The core (Hathaway, 2025, The Interior) occupies the central $0.25\,R_\odot$, where hydrogen fusion at a temperature of roughly 1.5×10^7 K and a density of $1.5\times10^5\,\mathrm{kg\,m^{-3}}$ generates most solar energy. Surrounding the core, **the radiative zone** spans up to $0.7\,R_\odot$, with energy transported via radiation. Density here decreases from 2×10^4 to $200\,\mathrm{kg\,m^{-3}}$, while temperatures fall from 7×10^6 K to 2×10^6 K. Photons traversing this dense region require millennia to reach **the tachocline**, a transitional layer discovered in the 1980s, and now thought to be critical for the solar dynamo due to its combined radial and horizontal shear while being positioned between the radiative and convective zones (Garaud, 2020, p. 1).

Energy transport shifts to convection in **the convection zone**, which extends to the

visible surface ($1\,R_\odot$). Temperatures decline from 2×10^6 K to 5700 K, with density dropping to $2 \times 10^{-4}\,\mathrm{kg\,m^{-3}}$. Convective motions here produce granulation patterns observable on the photosphere (Kivelson and Russell, 1995).

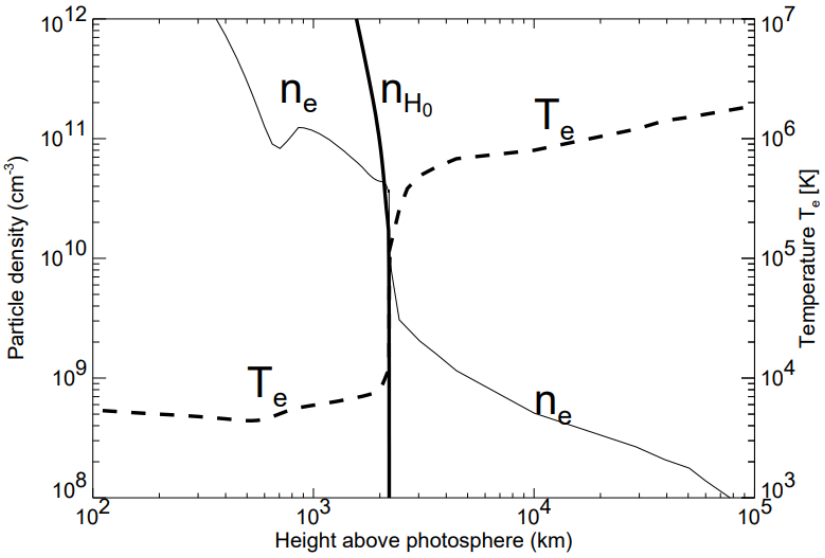

Figure 3: Diagram showing temperature and electron density models for the chromosphere and lower corona. The electron density is represented by n_e, while n_{H_0} denotes the neutral hydrogen density, reflecting the partially ionised nature of the chromospheric plasma. Adapted from Aschwanden (1966, Sec. 1.6).

The photosphere, defined as the Sun's surface, is approximately 100 km thick, and the coolest layer of the Sun with an effective temperature of $T_{\mathrm{eff}} = 5778$ K (Hathaway, 2025, The Photosphere). White-light observations reveal granules, sunspots, and faculae in this dynamic layer. This first layer of the solar atmosphere also exhibits intense magnetic activity.

Stretching $\sim$ 1600 km above the photosphere, **the chromosphere** shows a rise in temperature to 20000 K alongside decreasing density as shown in Figure 3 (Hathaway, 2025, The Chromosphere). Observations in the H_α line highlight its reddish colouration, a signature of excited hydrogen (Carroll and Ostlie, 2006, p. 364-365). A sharp temperature increase to 10^6 K occurs in **the transition region**, where ionised heavy elements emit light predominantly in UV and EUV wavelengths (Hathaway, 2025, The Transition Region).

Above this, **the corona**—the Sun's outermost atmosphere—reaches temperatures up to 5×10^6 K with particle densities of $10^{15}\,\mathrm{m^{-3}}$. Its plasma, emitting X-rays and EUV radiation, is categorised into **K**(continuum)-, **F**(Frauenhofer)- and **E**(Emission)-corona based on spectral features (Carroll and Ostlie, 2006, p. 366-370). The K-corona not only exhibits large Doppler shifts of the absorption lines from the photosphere, but also Thomson scattering (see Section 3.2) producing continuum radiation. A key unresolved question concerns the corona's extreme heating: while magnetic reconnection and wave

dissipation are proposed mechanisms, the precise drivers of the coronal heating problem remain elusive.

Table 2: Basic solar wind characteristics near Earth's orbit. Adapted from Schwenn (1990).

Characteristic	Slow Solar Wind	Fast Solar Wind
Speed w	$\lesssim 450\,\mathrm{km\,s^{-1}}$	$450 - 800\,\mathrm{km\,s^{-1}}$
Proton density n_p	$\sim 7 - 10\,\mathrm{cm^{-3}}$	$\sim 3\,\mathrm{cm^{-3}}$
Composition	$\sim 94\%$ H, 4% He, minor ions and same number of electrons	$\sim 95\%$ H, 5% He, minor ions and same number of electrons; great variability
Magnetic field strength B	$\sim 4\,\mathrm{nT}$	$\sim 5\,\mathrm{nT}$

The solar wind, a persistent outflow of coronal plasma (Hathaway, 2025, The Solar Wind), simultaneously fills and gives rise to the heliosphere (Hathaway, 2025, The Heliosphere), and was first discovered by Biermann (1951). The rotation of the Sun causes "toroidal spiralling" of the solar wind flowing outward radially, commonly referred to as Parker Spirals (Parker, 1958). At 1 AU distance, these flows come into contact with Earth and its magnetosphere at an angle of $\approx 45°$. Two types exist: the slow wind ($\lesssim 450\,\mathrm{km\,s^{-1}}$), compositionally similar to the corona, and the fast wind ($450 - 800\,\mathrm{km\,s^{-1}}$), resembling photospheric material (Bothmer and Zhukov, 2007, sec. 3.2.1). Their collision can generate shock waves. Some of their properties near Earth are detailed in Table 2. Open questions persist regarding the exact acceleration processes of both wind types.

2.3 Solar Activity and Phenomena

As the dominant energy source in the solar system, the Sun also showcases cyclical variability over an $\sim$ 11-year period—the solar cycle—marked by magnetic polarity reversals. Following the solar cycles periodicity, the activity of the Sun increases and decreases. Among the various solar activity phenomena at least partly tied to this process are sunspots, flares, prominences, CMEs, and solar energetic particle (SEP) events, with some capable of triggering geomagnetic disturbances at Earth.

Sunspots, transient dark regions often clustered in groups, signal underlying **active regions**, characterised by intense magnetic fields[2]. They are also illustrated in Figure 2. Systematic observations by Schwabe (1844) revealed the solar cycle's periodicity, quantified via the relative sunspot number (or Wolf number) introduced by Wolf (1856), nowadays more commonly known as the international sunspot number (SSN). It is

[2]Article by the University Corporation for Atmospheric Research (UCAR): https://scied.ucar.edu/learning-zone/sun-space-weather/sun-active-region (last accessed September 2022).

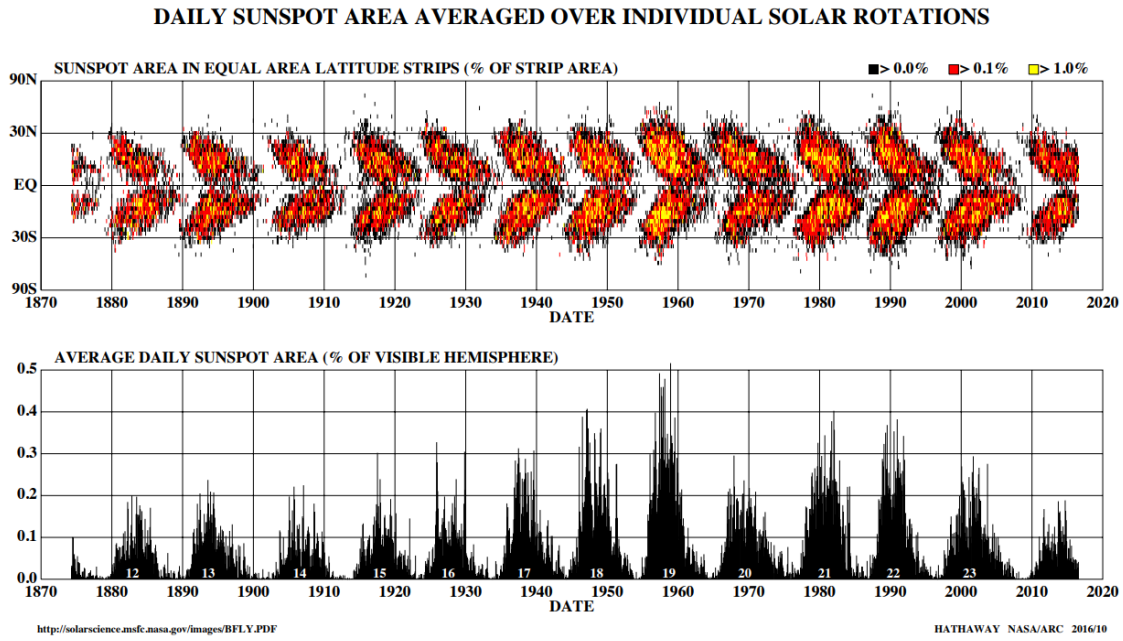

Figure 4: The top panel displays the butterfly diagram, showing the latitudes of sunspots recorded since May 1874 by the Royal Greenwich Observatory. Sunspots appear in two latitude bands near the equator, with their maximum latitudes decreasing as the solar cycle progresses. The bottom panel presents the 11-year sunspot cycle. From NASA, Dr. D. H. Hathaway, https://solarscience.msfc.nasa.gov/images/bfly.gif (last accessed March 2025).

computed via

$$\mathrm{SSN} = 10k \cdot (n_s + n_g)$$

where n_s, n_g, and k represent individual sunspot counts, the number of observed sunspot groups, and a scaling coefficient accounting for observational factors, respectively. Long-term studies typically use 13-month smoothed values of the SSN.

A consequence of solar activity is magnetic energy being transformed into other forms of energy, driving various solar phenomena. Magnetic reconnection in active regions drives phenomena like **flares**—sudden electromagnetic bursts across multiple wavelengths. First documented by Carrington (1859), flares often coincide with **CMEs** (see Chapter 3), large-scale ejections of coronal material. If directed Earthward, these can be the most geoeffective phenomena. Both, flares and CMEs frequently associate with **prominence eruptions** (Webb and Hundhausen, 1987), shown in Figure 2. **SEPs**, high-energy particles from eruptions (Droege and Schlickeiser, 1986), can ionise Earth's ionosphere upon magnetospheric penetration (Richard et al., 2002). Their composition resembles that of the solar wind, yet SEPs move at near-relativistic speeds.

3 Coronal Mass Ejections

This chapter provides an overview of CMEs and their interplanetary counterparts, ICMEs, covering their physical characteristics, observational techniques, and modelling frameworks for CME reconstruction and ICME propagation.

3.1 Overview

CMEs are eruptions of coronal plasma entangled within large, often flux rope-like magnetic structures. They represent drastic alterations in coronal configurations and appear as new, discrete, bright white-light features observable over timescales from a few minutes to several hours, according to the definition by Hundhausen et al. (1984). A key process in the initiation and evolution of CMEs is the reconnection of coronal magnetic field lines (Forbes, 2000), where oppositely directed magnetic field lines 'break' and realign, releasing stored magnetic energy and propelling the ejected material into the heliosphere. For solar flares—a phenomenon often accompanying CMEs—the occurrence of magnetic reconnection and the associated ejection of plasma, as interpreted via the Carmichael-Sturrock-Hirayama-Kopp-Pneuman (CSHKP) model, is illustrated in Figure 5. The CSHKP model, a collective term for four similar frameworks often referred to by a single name due to their shared features, "has been a standard model of flares" (Shibata and Magara, 2011).

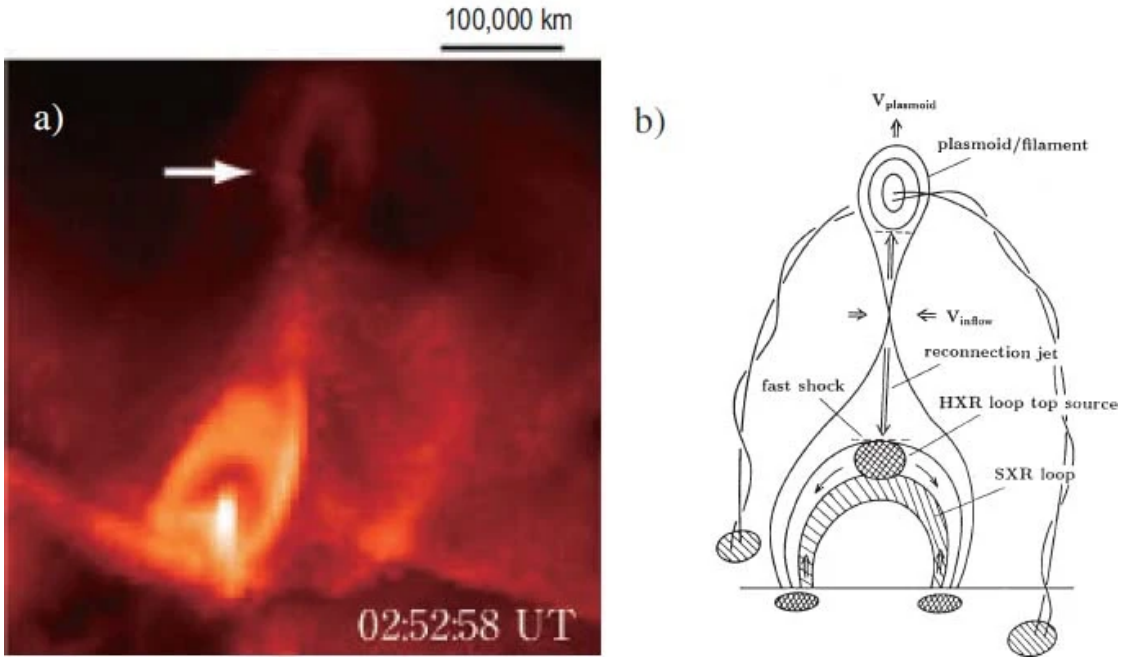

Figure 5: (a) Soft X-ray image of a solar flare captured by the satellite Yohkoh (from Shibata and Magara (2011)), and (b) a conceptual diagram illustrating a modified CSHKP model, integrating new features revealed by Yohkoh (from Shibata et al. (1995)).

Once accelerated beyond the Sun's gravitational force, CMEs traverse the solar wind as ICMEs (Cane and Richardson, 2003). These structures belong to one of two principal classes of large-scale interplanetary phenomena, the other being corotating interaction regions (Gopalswamy, 2007). The dynamics of ICMEs are influenced by their relative speed compared to the ambient solar wind: faster ICMEs are decelerated, while slower ones are accelerated (Vršnak et al., 2013).

Interplanetary shock waves ahead of ICMEs arise when an ICME's speed significantly exceeds that of the surrounding solar wind (Aschwanden, 1966, ch. 17.9.3). Sheeley et al. (1985) observed that interplanetary shock waves often accompany large ICMEs, which are considered their primary source. Typically, ICMEs propagate through space as magnetic clouds, preceded by a sheath region and an interplanetary shock front (Burlaga et al., 1981). According to the definition by Burlaga et al. (1981), an ICME is called a magnetic cloud if it has a magnetic flux rope structure.

Due to their high velocities and strong magnetic fields, ICMEs can cause substantial disturbances in Earth's magnetosphere. Earthward-directed ICMEs are the most geoeffective solar phenomena (Bothmer and Zhukov, 2007), capable of triggering intense geomagnetic storms that pose serious threats to space systems, communications, and navigation infrastructures (Schwenn, 2006). Consequently, accurate prediction of ICME arrival times and the refinement of models describing both ICMEs and their close-to-Sun counterparts, CMEs, are of critical importance.

3.2 Physics of Thomson Scattering

The phenomena of Thomson scattering is fundamental in imaging CMEs because these optically thin structures are observable through the scattering of photospheric white light by free electrons. The scattered light provides valuable insights into basic CME characteristics, such as mass (Colaninno and Vourlidas, 2009). Coronagraphs are specialised instruments designed to detect this faint light in comparison to the Sun's brightness. A comprehensive explanation of their mechanisms can be found in Section 4.5.

Generally, inelastic scattering involving free or quasi-free charged particles is described by Compton scattering. However, when dealing with visible light—where both the kinetic energy of the electron and the frequency of the photon are conserved during their interaction—the process approaches the low-energy limit of Compton scattering, resulting in an elastic collision. This specific case is referred to as Thomson scattering (Jackson, 1975).

Thomson scattering occurs under two primary conditions (Howard and Tappin, 2009):

1. The separation between scattering particles must be large compared to the coherence length of the incident radiation.

2. The rest mass energy of the scattering particle must be significantly greater than the energy of the photon.

The scattering processes in the Sun's corona and the solar wind within the heliosphere satisfy both conditions, making Thomson scattering the appropriate framework for these phenomena.

3.3 Observational Features of CMEs and ICMEs

Thousands of **CMEs** have been recorded using both ground-based coronagraphs and instruments onboard various space missions, such as the SOHO satellite (Section 4.2) and the STEREO probes (Section 4.3). This extensive number enables statistical investigations of their properties (Chen, 2011), e.g. their morphology, speed, mass, energy, angular width, and occurrence rate.

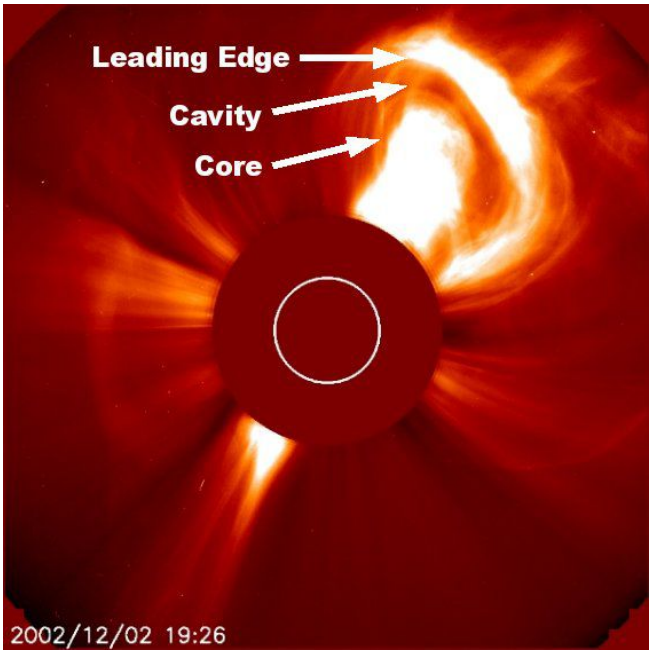

Figure 6: A CME exhibiting a clear three-part structure with a loop-like leading edge, a dark cavity, and a bright core, observed by C2 on December 2, 2002. From Colaninno (2012).

CMEs display a diverse range of **morphologies**, much of which is believed to result from projection effects (Schwenn, 2006). Nonetheless, fundamental differences exist between narrow CMEs and so-called 'normal' CMEs. Narrow CMEs display jet-like motions, likely along open magnetic field lines, whereas normal CMEs are characterised by a closed frontal loop (Chen, 2011). The morphology of a normal CME is generally described by the classical "three-part" structure (Illing and Hundhausen, 1985), consisting of a bright leading front curved into a loop with its bases anchored to the solar surface, followed by a dark cavity surrounding a bright core of prominence material. Figure 6

illustrates such a CME; however, it is important to note that not all normal CMEs possess all three components (Chen, 2011).

The **angular width** of CMEs as observed in the plane of the sky exhibits significant variation. Narrow CMEs have an angular width of less than 10°, while normal CMEs show values up to more than 120° (Yashiro et al., 2004), with an average of about 72° reported by Cremades and Bothmer (2004). CMEs may appear as outbursts surrounding the solar disk in the field of view (FOV) of the observer; these are called '**Halo CMEs**' or '**Halos**' and have an apparent angular width of or close to 360° (Chen, 2011). When only part of the solar disk is enclosed, the event is referred to as a 'partial Halo'. The most common interpretation of Halos is based on projection effects, defining Halos as events directed toward or away from the observer (Howard et al., 1982). Notably, Andrews (2002) described that significantly less Thomson scattered light is observed in the case of Halo events compared to non-Halo CME signatures, suggesting that many dim and slow Halos are missed by coronagraphs, which for example skews the observed average velocity of Halo events to higher values.

Table 3: Observational characteristics of CMEs. From Bothmer (2006).

Quantity	Value
Speed	$\sim 300 - 3000\,\mathrm{km\,s^{-1}}$
Mass	$5 \cdot 10^{12} - 5 \cdot 10^{13}\,\mathrm{kg}$
Kinetic Energy	$10^{23} - 10^{24}\,\mathrm{J}$
Angular Width	$\sim 24° - 72°$
Occurrence Frequency	$\sim 0.5 - 6$ per day (solar min. − solar max.)

The CME **velocity** is conventionally defined as the radial propagation speed of the apex of a CME frontal loop. However, in practice, measurements often rely on the projected motion of the CME frontal loop in the plane of the sky, yielding a projected velocity rather than the true radial speed. Plane of sky CME velocities range from approximately $20\,\mathrm{km\,s^{-1}}$ to over $3000\,\mathrm{km\,s^{-1}}$, occasionally reaching $3500\,\mathrm{km\,s^{-1}}$ (Chen, 2011). In halo events, it was frequently discussed that projection effects generally lead to an overestimation of the CME morphology and, consequently, to an underestimation of the CME speed (Gopalswamy et al., 2010). To correct the propagation velocity for projection effects, one approach involves modelling and tracking the evolution of CMEs in 3D space, taking into account their orientation and position on the Sun. This is achieved using, for example, the GCS model (see Section 3.4.1) (Thernisien et al., 2006), a method employed in this work.

The **occurrence rate** of CMEs closely follows the solar activity cycle (see Section 2.3, typically exhibiting a peak delay of approximately six to twelve months (Raychaudhuri, 2004). Most of the CME characteristics and observational features discussed above are summarised in Table 3.

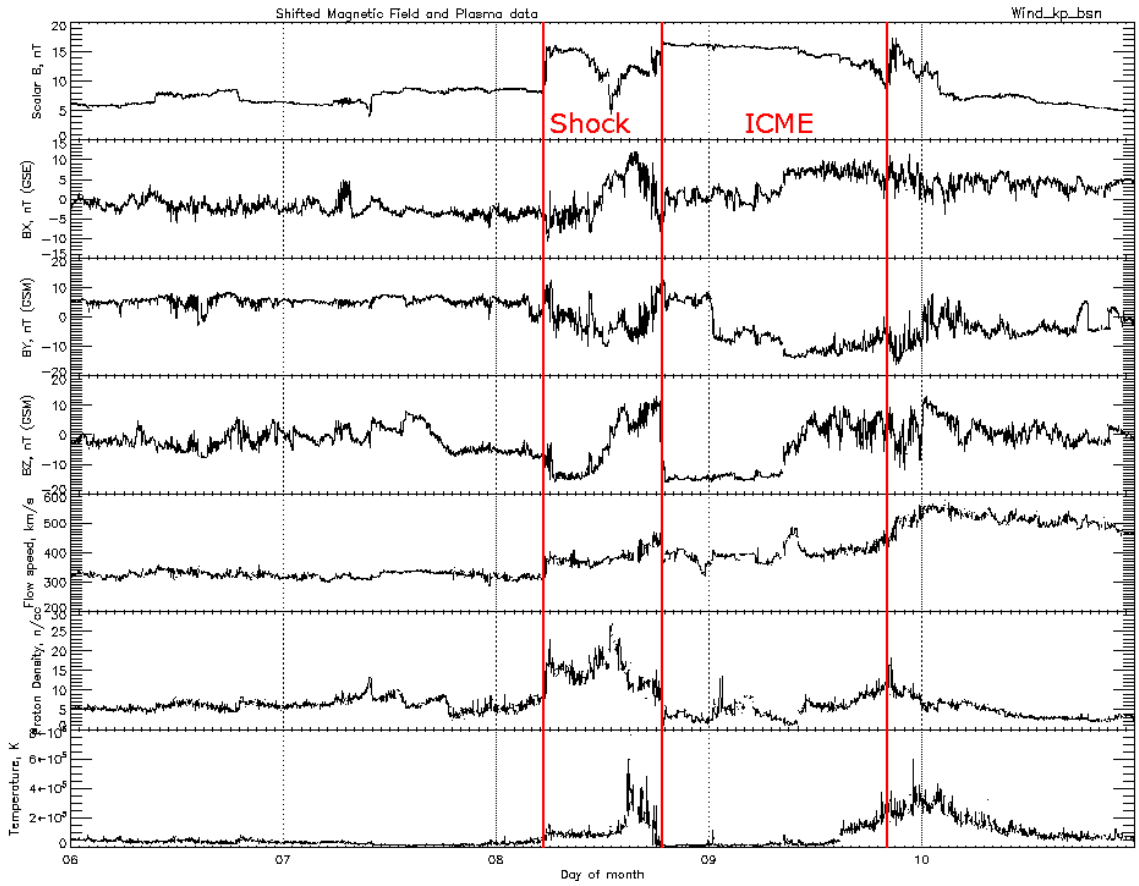

Figure 7: In-situ solar wind data of an ICME measured by the WIND spacecraft between October 6 and October 11, 2012. From top to bottom, the panels show the magnetic field strength (B) and its GSM components (B_x, B_y, B_z), along with the flow speed, density, and temperature. A shock signature is identified on 10/08 at approximately 05:00 UT, while the signature of the ICME is first identified at approximately 18:00 UT on the same day. The 1-minute averaged, bow-shock nose-shifted data were obtained from NASA's OMNIWeb Plus service[16].

Their interplanetary counterparts, **ICMEs**, are transient structures in the solar wind (Gopalswamy, 2007). These structures are most commonly detected through **in-situ** measurements of the near-Earth solar wind, conducted by satellites such as WIND (see Section 4.4) or ACE, positioned at L_1. These measurements typically analyse the solar wind's magnetic field components, temperature, proton density, and velocity.

Often, especially in the case of fast ICMEs, the following typical sequence of signatures is observed: a leading **shock front**, followed by a turbulent sheath region, and finally the ICME "driver gas" itself (Zurbuchen and Richardson, 2006). Compared to the shock disturbance, the ICME itself usually manifests as a longer-lasting disturbance in the solar wind parameters. In Figure 7, observations of an event exhibiting this structure are presented. Both the shock and the ICME show significantly enhanced magnetic field strengths compared to the ambient solar wind. In the case of the shock,

the plasma parameters—namely solar wind bulk velocity, proton density, and proton temperature—abruptly increase and remain strongly enhanced in the region between the shock and the ICME. Compared to those found for the shock and sheath region, the plasma parameters show lower values within the ICME. A lower than normal variance of the magnetic field, a classic signature for ICMEs (Bothmer, 2006), is detected for the magnetic field's components.

Table 4 presents key statistical values in various solar wind parameters for shock-driving ICMEs. These values can be compared to the characteristics of the common background solar wind types introduced in Section 2.2 and listed in Table 2. So-called **compound**

Table 4: Statistical properties of shock-driving ICMEs, a population of 109 events was considered. Adapted from Gopalswamy (2007).

Quantity	Value
Avg. Speed	$466\,\mathrm{km\,s^{-1}}$
Avg. Density	$7.4\,\mathrm{cm^{-3}}$
Avg. Duration	38.8 hr
Avg. Peak Magnetic Field Strength	15.6 nT

streams in the interplanetary medium are believed to form when two or more distinct flows of solar material, such as transient ejecta or corotating streams, interact with each other. This interaction can cause a "piling-up" effect, where multiple colliding ICMEs overlap. According to Burlaga et al. (1987), these interactions are often characterised by the presence of multiple ICME features within a short period. For example, they may produce multiple peaks in magnetic field strength or multiple distinct boundaries (see Figure 27 for example). Additionally, Burlaga et al. (1987) suggest that a significant number of geomagnetic storms are associated with these compound streams.

3.4 Modelling of CMEs and ICMEs

Modelling CMEs is critical for characterising their structure, dynamics, and key parameters, which in turn serve as essential input for estimating ICME propagation and forecasting space weather impacts on Earth. Among the primary parameters are CME velocity, orientation, angular width and height (Verbeke et al., 2019). Numerous methods and models have been developed to derive these properties from CME image data and other measurements. For example, Low et al. (1982) investigated the quasi-static evolution of an ascending loop-shaped CME structure, providing insights into early-stage CME dynamics. A comprehensive overview of CME initiation models can be found in Forbes (2000).

A well-known model is the two dimensional (2D) Ice-Cream Cone (ICC) model (Xue et al., 2005), which enables a quick estimation of radial speeds, angular widths, and

heliospheric positions. The CME Analysis Tool (CAT) (Millward et al., 2013) goes a step further by employing a 3D reconstruction with a tear-drop-like shape to capture orientation and spatial extension more accurately. Based on the results by Cremades and Bothmer (2004), the GCS model (Thernisien et al., 2006) infers a 3D flux rope-like structure. It defines the topology of an ascending CME early on while assuming a self-similar expansion (Chen, 1996).
For forecasting ICME arrival times and potential impacts, dedicated propagation models are formulated. These often utilise parameters derived from CME modelling, such as (2D or 3D) orientation, geometry, size, velocity, and/or position (Verbeke et al., 2019). A wide variety of such models exists, capable of predicting not only the arrival time and impact speed of an ICME at Earth but also plasma and magnetic properties over the course of its travel through the heliosphere (Vourlidas et al., 2019). The underlying assumptions and simplifications differ among models and approaches.
Common types of ICME propagation models include:

- Drag-based models
- Empirical models
- Expansion speed models
- Physics-based models
- Time-dependent magnetohydrodynamic (MHD) models

Zhao and Dryer (2014), and more recently Vourlidas et al. (2019), provide a detailed discussion of these model types in the context of arrival time predictions. This work employs the DBM (Vršnak et al., 2013) due to its extensibility and high relevance in the field. Its analytic solution facilitates rapid computation of ICME arrival times and speeds. A modified version, the Modified Drag-Based Model (MoDBM), incorporates recent findings to more accurately describe the ambient solar wind density and speed from the Sun to 1 AU, but is only solvable numerically (see Section 3.4.3).
These two models, as well as the GCS model, will be introduced and examined in detail in the following chapters. Nonetheless, it is important to note that no single model can perfectly represent every CME structure or every ICME propagation scenario. For example, CMEs do not always evolve in a self-similar manner, as assumed in the GCS model (Thernisien et al., 2006), and some events might deviate substantially from the assumptions embedded in other models. For instance, CME deflection, possibly caused by interactions with fast solar wind flows at higher latitudes (Cremades and Bothmer, 2004), can alter their apparent trajectory. Additionally, Lugaz et al. (2012) found that interactions between multiple CMEs may result in significant deflections.

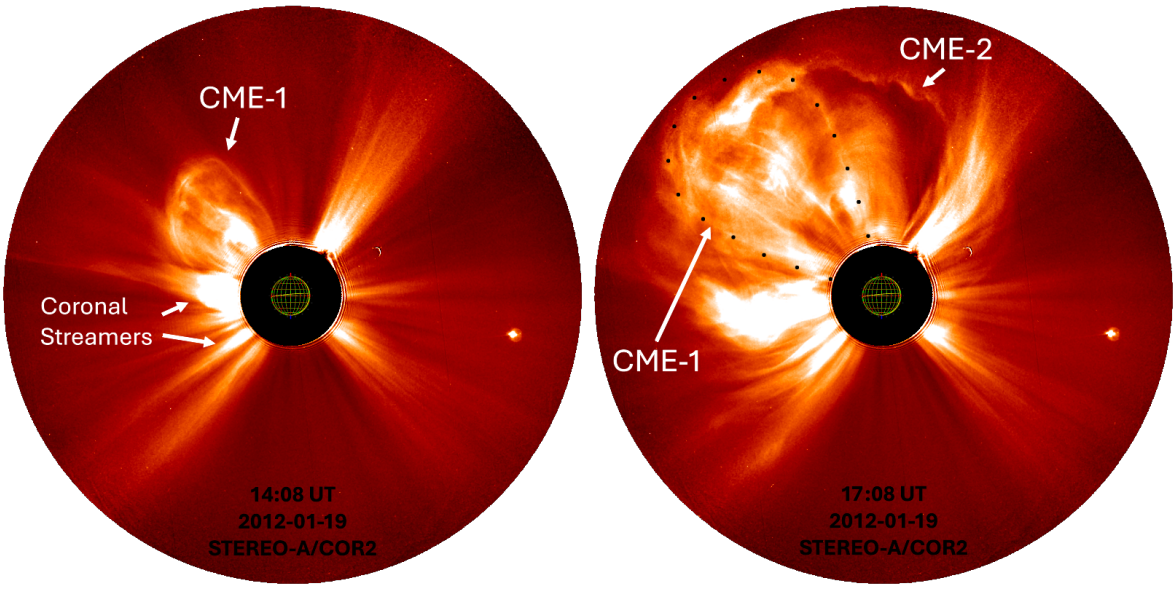

Figure 8: Overlapping CME signatures and coronal streamers captured on January 19, 2012, by COR2A. Left: a slowly erupting CME (annotated as CME-1) and several coronal streamers imaged at 14:08 UT. Right: a second, faster CME (annotated as CME-2) expanding in the same plane-of-sky direction completely superimposes on the slower CME from this perspective at 17:08 UT. Plain images were obtained using JHelioviewer[3], annotations were added.

Moreover, the interpretation of CME signatures in coronagraph images is further complicated by the optically thin nature of the solar corona. That is because multiple structures along the line of sight can contribute to the observed brightness, making it challenging to disentangle the signatures of CMEs from those of other solar phenomena. For example, multiple CMEs, a CME and helmet streamers, may overlap along the line of sight, as illustrated in Figure 8 via a set of observations retrieved using JHelioviewer[3]. Halo CMEs exhibit large angular expansions than other events, appear more faint due to significantly reduced Thomson scattered light being observed (see Section 3.3). Another difficulty arises from distinguishing the CME's shock front from its leading edge, as confusion between these features can alter the fitted morphology (Bosman, 2017, ch. 5.4.7).

An ICME's propagation through the heliosphere may be affected by similar complexities. Interactions with solar wind streams and other ICMEs may induce deflections or rotations (Kay et al., 2013), and such interactions can drastically alter the kinematics, magnetic properties, and space weather impacts of the ICME (Liu et al., 2014). Because most models cannot fully account for these effects, predicting ICME arrival times and impacts becomes increasingly uncertain under these conditions.

[3]Homepage (last accessed December 2024): https://www.jhelioviewer.org

3.4.1 The Graduated Cylindrical Shell Model

The Graduated Cylindrical Shell (GCS) modelling technique (Thernisien et al., 2006) is an empirically defined method designed to help investigate the idea of reconstructing the large-scale, 3D structure of CMEs as a flux rope in coronagraph images. Among the more complex geometrical models describing CME morphology, the model is widely used in the field of space weather, especially when combined with stereoscopic imaging data from missions like STEREO. Developed based on the findings of a systematic study by Cremades and Bothmer (2004), the GCS model is utilised in this work to approximate a CME's physical dimensions, spatial orientation, and derive its kinematics.

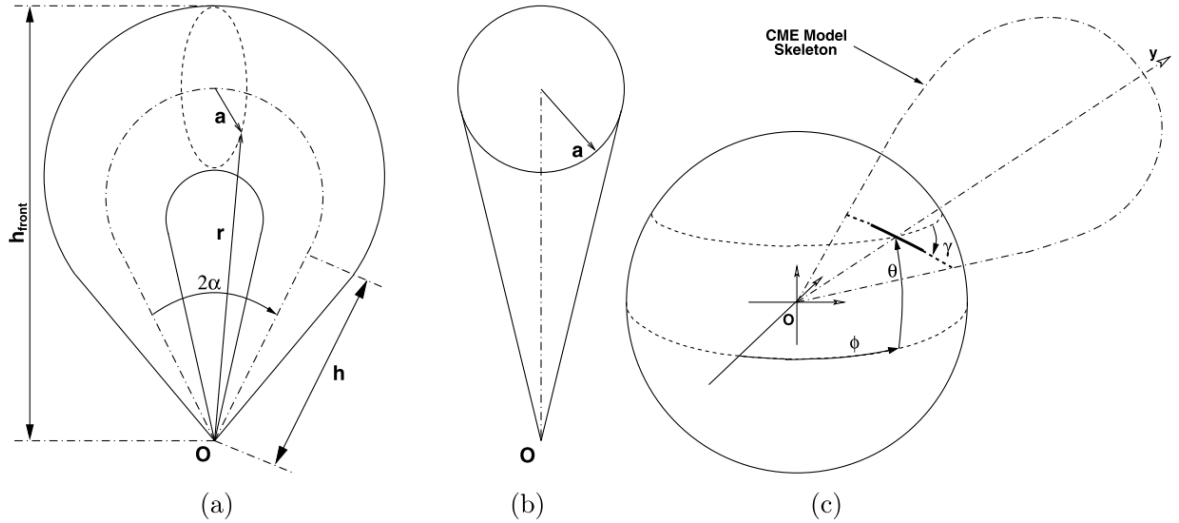

(a) (b) (c)

Figure 9: The GCS model in three views: (a) face-on, (b) edge-on, and (c) the positioning parameters in 3D space. Views (a) and (b) display the model with parameters a, r, α, and h marked (see Equation 1 and Equation 2). The dash-dotted line indicates the axis through the center of the shell, while the solid line shows a planar cut through the cylindrical shell and the origin. View (c) illustrates the positioning and orientation parameters ϕ_C, θ, and γ of the model's skeleton. From Thernisien et al. (2009).

As shown in Figure 9, the GCS geometry consists of two cone-shaped legs connected to a tubular section, the radius of which decreases towards the ends, resulting in a shape reminiscent of a croissant. The centre of the tube is indicated by a dash-dotted line, while the solid lines represent the outline of the model. The model is bilaterally symmetric with respect to its central axis.

The circular annulus of the tubular section has a varying radius a that is determined by

$$a(r) = \kappa r \tag{1}$$

with r representing the distance from the centre of the Sun to a point at the outer edge of the GCS model shell. The constant κ is the first free parameter of the model and describes the aspect ratio of the two orthogonal CME sizes a and r. Determining κ

effectively adjusts the 'thickness' of the models legs and tubular section to match the CME structure observed in coronagraphic images.

Equation 1 also embodies the simplifying assumption that flux rope-like CMEs expand in a self-similar fashion after around $12\,\mathrm{R}_\odot$ (e.g., Chen (1996), Cremades and Bothmer (2004)). This means that the size of a given CME feature scales proportionally with its distance from the centre of the Sun, maintaining a consistent ratio. Consequently, as the CME propagates through interplanetary space, its expansion preserves the angular width (or solid angle), ensuring that the overall shape remains geometrically similar throughout its evolution. This concept is applied once more and discussed further in Section 7.3.

The ends of the legs originate from the centre of the Sun, and the angle between the two legs is twice the half-angle α, the second free parameter of the model. Using the leg height h and the previously described parameters, the third parameter, the height of the leading edge of the model relative to the centre of the Sun, also known as the front height or apex height h_{apex}, can be calculated via

$$h_{\mathrm{apex}} = h\frac{1+\kappa}{1-\kappa^2}\frac{1+\sin\alpha}{\cos\alpha}\,. \tag{2}$$

A common measure of the CME size, utilised in propagation models such as the DBM (see Section 3.4.2) to estimate CME dynamics, is the cross-sectional area A. While Thernisien (2011) details numerical calculations for determining A, the added complexity does not justify the marginal gains in precision. This work employs a faster analytic approach via

$$A(r) = \pi r_c^2 \tan(\alpha)\tan(\delta) \tag{3}$$

where $\delta = \arcsin(\kappa)$ and $r_c = \frac{r}{(1+\kappa)}$ (Pluta, 2018, p. 111). Here, A is approximated using the base area of an elliptical cone at the flux rope centre height (r_c) and the two half-angles (α and δ) of the cone's main axes. A depends on the distance r [km] of the CME or ICME apex from the Sun.

Three additional parameters of the GCS model describe the position and orientation of the flux rope in 3D space (see Figure 9 (c)). The Carrington longitude ϕ_C and heliographic latitude θ are commonly used to specify the exact position of a projection on the solar surface, in this case the projection of the CME apex. Rotating the model results in a non-zero tilt angle γ; when $\gamma = 0°$, the tubular section of the model is parallel to the solar equator, and when $\gamma = \pm 90°$, it is perpendicular. Due to the axial symmetry of the model, the direction of rotation is irrelevant for γ.

Besides the Carrington longitude, the Stonyhurst longitude ϕ is also commonly used. The Stonyhurst coordinate system remains fixed with respect to the Earth while the Sun rotates beneath it synodically; its origin is at the intersection of the solar equator

and the central meridian as seen from Earth. In contrast, the Carrington coordinate system rotates with the solar surface and is not fixed relative to Earth. Therefore, the Carrington longitude is offset from the Stonyhurst longitude by a time-dependent scalar value given by

$$\phi_C = \phi + L_0 \tag{4}$$

where L_0 is the Carrington longitude of the central meridian as seen from Earth. The latitude θ is defined identically in both the Stonyhurst and Carrington coordinate systems (Thompson, 2006).

While Thernisien et al. (2006) describe how a synthetic white-light image obtained from the model using an asymmetric Gaussian density profile can be compared to the white-light signature of a CME in real coronagraph images, it is more common to compare a simple 3D mesh representing the GCS model to the signature instead. This approach, along with a Python tool, is described in Section 7.1.1.

3.4.2 The Drag-Based Model

The Drag-Based Model (DBM) is a one dimensional (1D) model primarily designed for estimating the heliospheric propagation of ICMEs from the Sun to 1 AU (Vršnak et al., 2013). It relies on the observational fact that slow CMEs are accelerated, while fast CMEs are decelerated due to MHD drag forces. This interaction leads to an adjustment of the CME's velocity towards that of the ambient solar wind.

Although the DBM is simplistic compared to other models, it compares well in prediction accuracy and remains highly relevant in the field (Vourlidas et al., 2019). The model assumes that the driving Lorentz force responsible for launching a CME decreases significantly in the upper corona. Cargill (2004) suggest that beyond 15–20 $\mathrm{R}_\odot$, the interaction between the ICME and the ambient solar wind becomes the dominant factor in the propagation dynamics.

The MHDs drag arises from the collisionless transfer of momentum and energy between the ICME and the solar wind. It is assumed to take a quadratic form, meaning that the drag force is considered proportional to the square of the relative speed between the ICME and the solar wind (Vršnak et al., 2013). The drag acceleration is given by

$$a = -\gamma\,(v - w)\,|v - w| \tag{5}$$

where v is the instantaneous ICME velocity, w is the ambient solar wind speed, and γ is the drag parameter. The equation of motion, depending on the radial distance r

from the Sun, then reads

$$\frac{\mathrm{d}^2 r}{\mathrm{d}t^2} = -\gamma(r)\left(\frac{\mathrm{d}r}{\mathrm{d}t} - w(r)\right)\left|\frac{\mathrm{d}r}{\mathrm{d}t} - w(r)\right| . \tag{6}$$

Assuming a constant drag parameter (γ = const.) and ambient solar wind speed (w = const.), the analytic solution to the equation of motion is

$$r(t) = \pm\frac{1}{\gamma}\ln\left[1 \pm \gamma\left(v_0 - w\right)\right] + wt + r_0 \tag{7}$$

where v_0 is the initial ICME velocity at time $t = 0$, and r_0 is the initial radial distance. Given that it is a 1D equation, the propagation of a single point is considered, typically corresponding to the CME apex. Most importantly for this work, the model is also well-suited to determine the propagation of an arbitrary, non-apex point on the CME leading edge, if it is combined with the assumption of self-similar expansion of the CME (see Section 3.4.1) (Dumbović et al., 2021). This is achieved by substituting the initial velocity v_0 in the DBM equation with the velocity of the non-apex point of interest on the CME leading edge. This procedure is detailed in Section 7.3.

The assumptions of a constant drag parameter and ambient solar wind speed are not always good approximations, especially in cases where more complex processes and associated interactions between CME and solar wind must be considered (see Section 3.3). To obtain the best results, it is crucial to determine the solar wind speed in close temporal proximity to the ICME, and to choose an appropriate take-off distance r_0. An approach for estimating the ambient solar wind speed is detailed in Section 7.4.1, and acceptable value ranges for the take-off distance are discussed further down in this section.

Generally, the drag parameter γ, given by

$$\gamma(r) = \frac{c_d A \rho_w}{M} \tag{8}$$

changes with distance (see Section 3.4.3). However, in the simplest form of the DBM model, which uses a constant drag parameter, the following assumptions are made (Vršnak et al., 2013):

- At large distances, e.g. $r > 15\,\mathrm{R}_\odot$, the drag coefficient c_d is constant (c_d = const.).
- The cross-sectional area A of ICMEs scales as $A \propto r^2$.
- The ambient solar wind density ρ_w follows $\rho_w \propto r^{-2}$.
- The ICME mass M remains constant (M = const.).

MHD simulations suggest that beyond 15–20 $\mathrm{R}_\odot$, it is reasonable to assume that ICME motion can be modelled by a drag force that is approximately independent of radial

distance, with a drag coefficient c_d of the order of unity (Cargill, 2004). Taking that under consideration, Dumbović et al. (2021) recommend $r_0 \geq 20\,\mathrm{R}_\odot$ as the optimal value range. Nonetheless, choosing an appropriate starting height r_0 is often difficult, as it is not always the case that the Lorentz force has ceased at heights below this range. In some cases, significant acceleration of a CME is observed even beyond $20\,\mathrm{R}_\odot$ (Vršnak et al., 2004). Moreover, since a GCS+DBM modelling approach is utilised in this work, the data available for stereoscopic reconstruction might present an upper limit due to the CME only being observed up to a certain height. How the starting height is chosen on a per-event basis is further explained in Section 7.4.1.

The cross-sectional area A depends on the model used for CME reconstruction. The quadratic scaling law shown above can be derived, among other approaches, by approximating the cross-section of the GCS model via Equation 3 (see Section 3.4.1).

The ambient solar wind density $\rho_w(r)$ is calculated via

$$\rho_w(r) = m_p n_0(r) \tag{9}$$

where $m_p \approx 1.672621925 \times 10^{-27}\,\mathrm{kg}$ is the proton mass[4]. According to the first-order approximation of the empirical solar wind model (Leblanc et al., 1998), the particle density $n_0(r)$ is modelled as

$$n_0(r) \simeq 3.3 \cdot 10^5\,[\mathrm{cm}^{-3}] \cdot \frac{1}{r^2}\,. \tag{10}$$

with r in units of $\mathrm{R}_\odot$.

Pluta et al. (2018) used the GCS model to estimate CME masses and analyse suitable CME characteristics. They proposed an empirical correlation between CME masses and velocities that reads

$$\log_{10}(M) = 3.4 \cdot 10^{-4} \cdot v_{\mathrm{apex}} + 15.479 \tag{11}$$

where M is the CME mass in kg, and v_{apex} is the CME apex-directed velocity (as defined in Section 3.4.1) in $\mathrm{km\,s}^{-1}$. This correlation was derived from analysis on an extensive dataset of CMEs with diverse properties, and enables fast and simple estimation of the CME mass based on the apex-directed velocity.

Lastly, it is common to substitute γ with

$$\Gamma = \gamma \cdot 10^7\ [\mathrm{km}^{-1}]\,. \tag{12}$$

Under the above assumptions, values for Γ typically range between 0.1 and $2\,\mathrm{km}^{-1}$ for magnetic ejecta (Vršnak et al., 2013).

[4]Published by the CODATA Task Group on Fundamental Constants: https://physics.nist.gov/cgi-bin/cuu/Value?mp (last accessed October 2024).

3.4.3 The Modified Drag-Based Model

The Modified Drag-Based Model (MoDBM) is an adaptation of the DBM designed to determine the heliospheric propagation of ICMEs from the Sun to 1 AU. It integrates more recent scientific insights into various components of the DBM, and was developed collaboratively with my supervisor, Dr. V. Bothmer, at the Institute for Astrophysics and Geophysics at Georg-August-University of Göttingen. While retaining its foundational assumptions, the MoDBM modifies key parameters within the DBM's drag acceleration (see Equation 5) and equation of motion (see Equation 6). These adjustments refine the parameters to more accurately account for dependencies on solar distance.

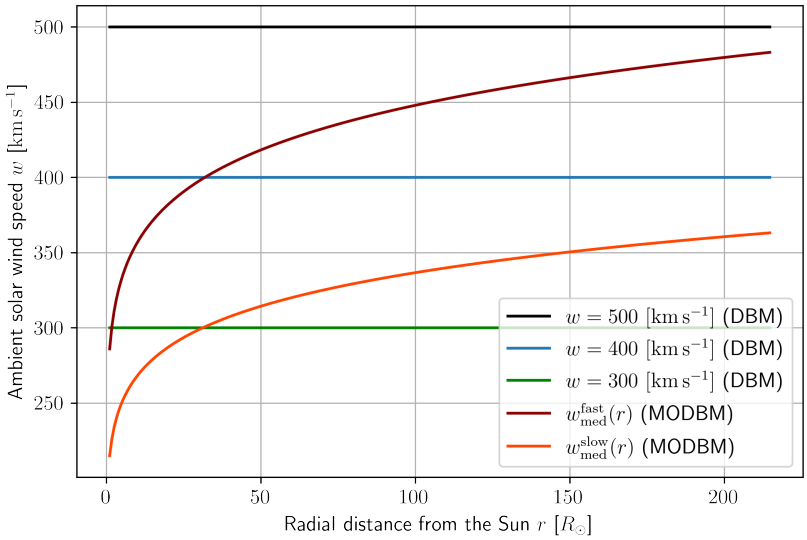

Figure 10: Comparison of ambient solar wind speed models between the DBM and MoDBM in the range from the Sun to 1 AU. In the DBM, w is considered constant and is displayed for values of 300, 400 and 500 km s^{-1}. In contrast, the MoDBM introduces distinct distributions for the slow and fast solar wind regimes.

A significant modification is the treatment of the ambient solar wind speed w. Contrary to the DBM's assumption of a constant solar wind speed from 0 to 1 AU, the MoDBM employs distance-dependent distributions, as derived by Venzmer and Bothmer (2018) using data from the Helios missions in preparation for the launch of the Parker Solar Probe. The authors assume time-independent scaling laws for simplicity, treating yearly variations in exponents as uncertainties. The median ambient solar wind speed profiles for slow and fast solar wind are given by

$$w_{\mathrm{med}}^{\mathrm{slow}}(r) = 363\,[\mathrm{km\,s^{-1}}] \cdot r^{0.099} \quad \text{and} \quad w_{\mathrm{med}}^{\mathrm{fast}}(r) = 483\,[\mathrm{km\,s^{-1}}] \cdot r^{0.099} \tag{13}$$

where r represents the solar distance in AU. In Figure 10, both the slow and fast solar wind speed distributions, along with several distributions consistent with the DBM, are presented.

To apply the model, either $w_{\text{med}}^{\text{slow}}$ or $w_{\text{med}}^{\text{fast}}$ is selected as the ambient solar wind speed distribution interacting with the propagating ICME. The appropriate distribution is chosen by determining the ambient solar wind speed in close temporal proximity to the ICME (similar to how the most accurate value of w is determined in the DBM, described in Section 3.4.2), and selecting the distribution that best matches the observed value. For a more detailed approach, refer to Section 7.4.1.

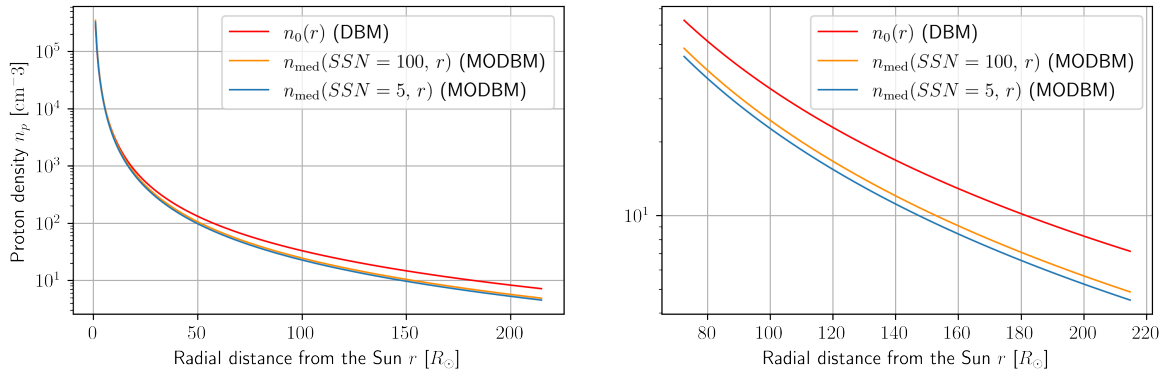

Figure 11: Comparison of proton density models between the DBM and MoDBM in the range from the Sun to 1 AU. The models are displayed logarithmically as a function of the distance from the Sun, r. The proton density model in the MoDBM is presented for two different SSN values. The right panel provides a zoomed-in view, focusing on the range between 0.34 and 1 AU.

An important factor in calculating the drag parameter γ via Equation 8 is the ambient solar wind density ρ_w, which is determined by multiplying the ambient particle density by the proton mass (see Equation 9). The DBM employs a first-order approximation of the empirical solar wind model to estimate the particle density (see Equation 10). In their study, Venzmer and Bothmer (2018) found a more precise proton density relation dependent on both the distance from the Sun r in AU and the SSN (see Section 2.3) via

$$n_{\text{med}}(SSN, r) = \left(0.0038\,[\text{cm}^{-3}] \cdot SSN + 4.50\,[\text{cm}^{-3}]\right) \cdot r^{-2.11}\,. \tag{14}$$

The SSN is utilised to account for solar cycle variations. Its impact is relatively small, even when comparing significant solar activity (SSN = 100) to very low activity (SSN = 5). Figure 11 highlights this, while also comparing the proton density models of the DBM and MoDBM across a range from 0 to 1 AU. Moreover, a zoomed-in version of the plot (from 0.34 to 1 AU) is also shown.

The other parameters that make up the drag parameter γ, such as the cross-section A and the CME mass M are calculated in accordance with the DBM. The newer findings introduce more complex dependencies on distance compared to the dependencies in the DBM. Crucially, this results in a drag parameter that is not constant with respect to the solar distance r. When the new expressions are substituted into the equation of motion (Equation 6), the analytic solution available in the original DBM (see Equation 7) is no

longer valid, and the equation can only be solved numerically. As a result, The MoDBM requires solving a homogeneous linear second-order ordinary differential equation (ODE) initial value problem. This is achieved by:

1. Converting the equation into a system of two homogeneous linear first-order ODEs by defining two new unknown functions $r_1 = r$ and $r_2 = \frac{\mathrm{d}r}{\mathrm{d}t}$.

2. Integrating this system with defined initial values for the starting height and velocity of the ICME.

The 2D system of first-order coupled ODEs then reads

$$\frac{\mathrm{d}r_1}{\mathrm{d}t} = r_2 \tag{15}$$

$$\frac{\mathrm{d}r_2}{\mathrm{d}t} = -\gamma(r_1)\left(\frac{\mathrm{d}r_1}{\mathrm{d}t} - w(r_1)\right)\left|\frac{\mathrm{d}r_1}{\mathrm{d}t} - w(r_1)\right| \tag{16}$$

$$\text{with } \gamma(r_1) = -\frac{c_d}{M}\cdot\left(\frac{r_1}{1+\kappa}\right)^2 \pi\tan(\alpha)\tan(\arcsin(\kappa)) \cdot m_p \cdot \left(0.0038\,[\mathrm{cm}^{-3}]\cdot SSN + 4.50\,[\mathrm{cm}^{-3}]\right)\cdot r_1^{-2.11}$$

$$\text{and } w(r_1) = w_0 \cdot r_1^{0.099} \quad \text{with} \quad w_0 = \begin{cases} 363\,\mathrm{km\,s^{-1}}, & \text{for slow ambient solar wind.} \\ 483\,\mathrm{km\,s^{-1}}, & \text{for fast ambient solar wind.} \end{cases}$$

This system incorporates Equation 3, Equation 9, Equation 13 and Equation 14.
While the overall drag acceleration in the MoDBM can be higher near the Sun, it decreases significantly with distance compared to the DBM due to the $r^{-2.11}$ dependence of the proton density. Limitations of the DBM that are not directly addressed by the changes described above are inherited by the MoDBM. For example, determining an appropriate take-off distance r_0 for each ICME remains equally challenging.

4 Missions and Instrumentation

In this chapter, the missions and instruments central to this work are introduced. Data from the coronagraphs on board SOHO and STEREO are used for 3D CME reconstruction, while WIND provides solar wind and ICME measurements. These analyses support the development of the upcoming Vigil mission, whose concept and objectives are also outlined.

4.1 The Vigil Mission

The European Space Agency (ESA) is developing the Vigil mission, which aims to position a spacecraft at the Sun-Earth Lagrange point 5 (L_5). Scheduled for launch in the early 2030s[5], Vigil (formerly known as the Lagrange mission) is designed to enhance space weather forecasting by providing early warnings of solar activity.

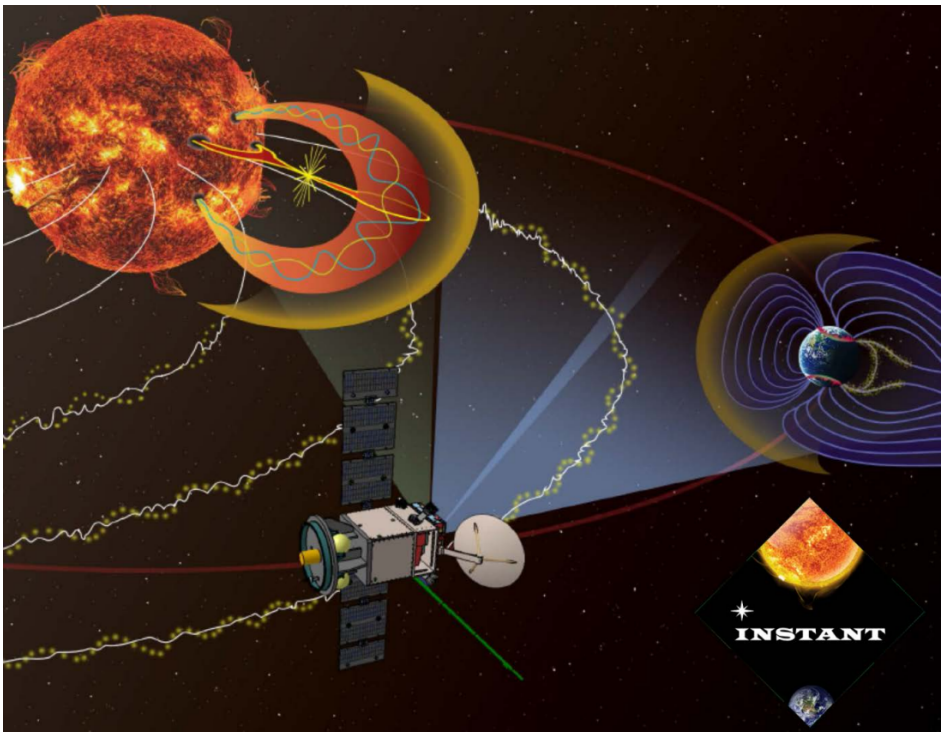

Figure 12: Artistic rendering of the INSTANT mission concept, highlighting space weather monitoring capabilities from L_5. From Lavraud et al. (2016).

Several mission concepts have previously targeted L_5, notably the Investigation of Solar-Terrestrial Activity and Transients (INSTANT) mission proposal (Lavraud et al., 2016). While sharing the goal of utilising the L_5 vantage point to monitor solar activity and track CMEs, INSTANT was primarily geared toward scientific research. In contrast, Vigil is conceived as an operational space weather warning system. An artistic depiction of the INSTANT mission concept is shown in Figure 12. Another early concept was

[5] Official Vigil Mission Website (last accessed October 2024): https://www.esa.int/Space_Safety/Vigil

outlined by Schmidt and Bothmer (1996) and submitted to an ESA mission call in 1993. It shared similarities with INSTANT, particularly in terms of its constrained payload budget, although it differed in instrumentation, scientific objectives, and mission profile. As a technical note[6] published by ESA states, Vigil's primary objectives are to:

- Improve estimation of CME motion, direction, speed, and density.
- Enhance detection of solar activity onset by monitoring the development of active regions.
- Enable early detection of solar disk activity several days before it becomes visible from Earth.

L_5 offers significant advantages for space weather observation. By imaging 60° of the solar disk unseen from Earth, Vigil can provide 4–5 days' advance warning of active regions. This early detection is crucial for preparing and mitigating the impacts of space weather events on Earth. Furthermore, Vigil's position allows it to supply real-time magnetogram data, extending the coverage to two-thirds of the photosphere in conjunction with already operating missions, thereby enhancing space weather models and improving ICME tracking as they approach Earth. The L_5 location also enables advance measurement of recurrent solar wind disturbances, leading to more accurate space weather predictions (Vourlidas, 2015).
ESA's technical note further outlines five baseline instruments Vigil will carry:

1. Photospheric Magnetic Field Imager (PMI): Captures photospheric magnetic field data to predict solar wind and CMEs.
2. Compact Coronagraph (CCOR): Detects the onset of CMEs.
3. Heliospheric Imager (HI): Provides wide-angle imaging to track CME propagation.
4. Plasma Analyzer (PLA): Measures solar wind characteristics.
5. Magnetometer (MAG): Measures the interplanetary magnetic field.

The remote sensing instruments (PMI, CCOR, HI) focus on tracking solar activities, while the in-situ instruments (PLA, MAG) measure local solar wind conditions and magnetic fields. They make forecasting space weather disturbances and predicting magnetic storms possible.
This work analyses CME events and simulates their Earthward evolution using data obtained by STEREO when it was in proximity to L_5, or at least when it offered a

[6]Technical Note by ESA on Vigil's Objectives + Payload Description (last accessed October 2024): https://lws.larc.nasa.gov/vfmo/pdf_files/ESA-S2P-LGR-MO-0002_i2r0_Vigil_mission_objectives_and_payload_description.pdf

perspective significantly different from Earth's viewpoint (see Section 4.3). Although this work employs three viewpoints for the 3D reconstruction of CMEs, the methods developed and applied here are highly relevant for optimising predictive capabilities in space weather forecasting from the L_1 and L_5 perspectives. Therefore, the findings may aid in meeting Vigil's objectives. Further discussion on this topic is presented in Chapter 9.

4.2 The SOHO Mission

The Solar and Heliospheric Observatory (SOHO) mission (Domingo et al., 1995) was developed collaboratively by ESA and National Aeronautics and Space Administration (NASA) and launched in December 1995. The principal scientific objectives of the mission are to study the solar interior, investigate the processes involved in shaping and heating the solar corona, and understand the solar wind. The main focus is on helioseismology. To enable continuous observation of the Sun, the spacecraft was placed in a halo orbit around L_1, which is positioned along the Sun-Earth line, about 1.5×10^6 km from Earth.

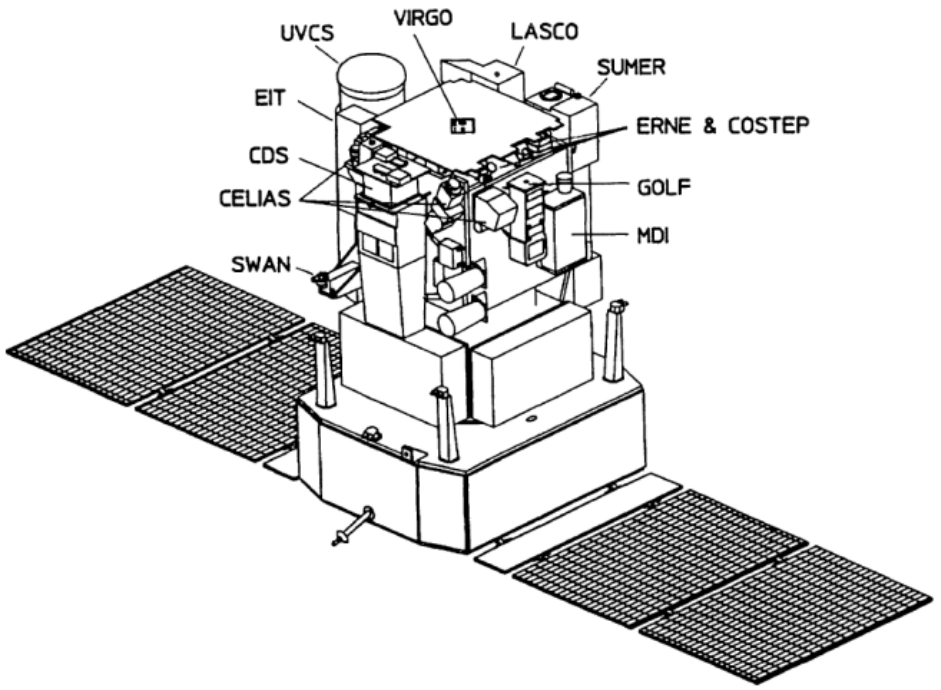

Figure 13: Schematic diagram of the SOHO spacecraft an on board instrumentation. From Domingo et al. (1995).

SOHO is equipped with twelve scientific instruments designed to observe different aspects of the Sun, from its interior to the outer corona and the solar wind. A schematic representation of these instruments is provided in Figure 13. Among the remote-sensing instruments on board is Large Angle and Spectrometric Coronagraph (LASCO) (Brueckner et al., 1995), which comprises three coronagraphs with overlapping FOVs.

LASCO's combined observations cover a wide range of distances from the Sun's surface, making it a key instrument for studying the solar corona and CMEs. The data obtained from LASCO is crucial for this work and is discussed in more detail in Section 4.5.1.
SOHO's continuous monitoring of the Sun and its ability to detect CMEs have made it an invaluable asset for space weather forecasting and providing early warnings of potential solar storms. Beyond these operational contributions, the mission has led to numerous scientific discoveries, including the identification of more than 5.000 comets[7].
Although SOHO was originally planned for a three-year mission ending in 1998, its operation at L_1 has been extended several times due to its ongoing scientific value. As of now, SOHO has observed two full 11-year solar activity cycles and has entered into the monitoring of a third cycle, continuing to provide valuable data on solar phenomena.

4.3 The STEREO Mission

The Solar TErrestrial RElations Observatory (STEREO) mission (Kaiser et al., 2008), developed by NASA, was successfully launched in October 2006. The investigation of the causes and mechanisms behind the initiation and propagation of CMEs from the Sun through the inner heliosphere to Earth is among the primary objectives of the mission. It consists of two nearly identical satellites, named STEREO-Ahead (STA) and STEREO-Behind (STB), each positioned to provide unique vantage points for observing solar phenomena.
Each spacecraft is equipped with a comprehensive set of instruments, including optical, radio, and in-situ particles and fields detectors. One of the four instrument suites on board is the Sun-Earth Connection Coronal and Heliospheric Investigation (SECCHI) suite (Howard et al., 2008). It contains two coronagraphs, namely STEREO/SECCHI Coronagraph 1 (COR1) and STEREO/SECCHI Coronagraph 2 (COR2), an Extreme Ultraviolet Imager (EUVI), and two wide-angle Heliospheric Imagers (HIs). This combination of instruments on both STA and STB enables the 3D tracking of the white-light signatures of CMEs from their origins in the solar corona to their propagation through the heliosphere. For the purposes of this work, images taken with the COR2 coronagraphs on both STEREO spacecraft are utilised, detailed information on which is provided in Section 4.5.2.
A notable milestone of the STEREO mission was achieved on February 6, 2011[8], when it provided the first complete stereoscopic view of the Sun. This achievement allowed researchers to observe and search for connection between solar phenomena across the entirety of the Sun. To gain stereoscopic views of the Sun and its corona, the STA and STB spacecraft were placed in heliocentric orbits with slightly different orbital periods.

[7] Up-to-Date Article by NASA (last accessed November 2024): https://science.nasa.gov/mission/soho
[8] Article published by NASA/Goddard Space Flight Center on February 6th, 2011: https://svs.gsfc.nasa.gov/10718/ (last accessed November 2024).

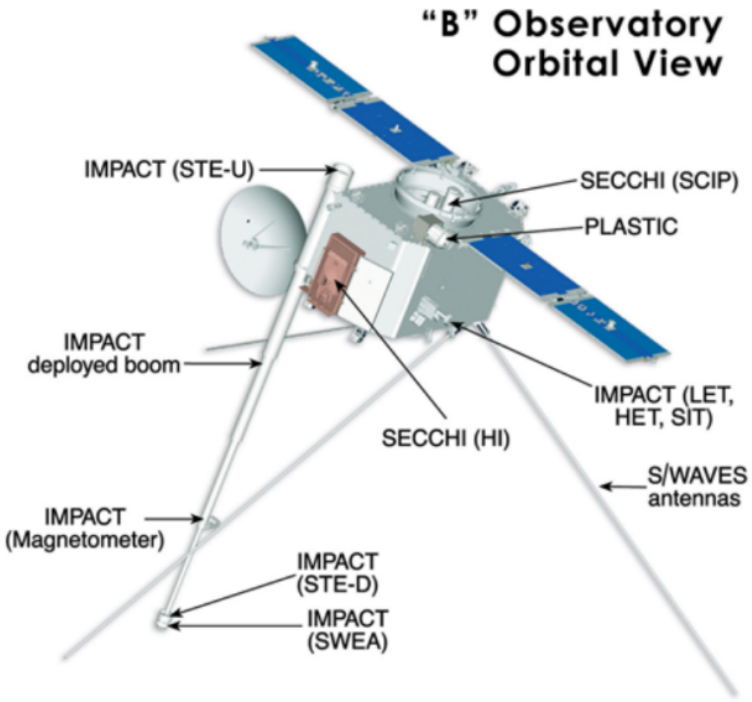

Figure 14: Schematic of the STB spacecraft with its on board instruments. From Kaiser et al. (2008).

STA orbits closer to the Sun than Earth and moves ahead of Earth in its orbital path, while STB orbits slightly further from the Sun and trails behind Earth. As a result, the separation angle between STA and STB increases by approximately 44° to 45° per year, $\approx 22°$ with respect to the Sun-Earth line for each spacecraft individually. Thus, the spacecraft drifted across positions near the Lagrange point 4 (L_4) and L_5 of the Sun-Earth system over time[9].

Table 5: Notable STEREO spacecraft configurations in the Sun-Earth system and their corresponding time frames. Created with data from NASA's STEREO Orbit Tool[10].

Date Range	Configuration Description
$\sim$ 06/2007 – 09/2014	The combined observations of STA, STB and SOHO allow for robust 3D CME reconstruction.
$\sim$ 08/2008 – 01/2011	STB traversed a region approximately $\pm 30°$ around L_5.
$\sim$ 07/2019 – 05/2022	STA traversed a region approximately $\pm 30°$ around L_5.

The varying geometric configurations of STA and STB have been particularly valuable for the reconstruction of large-scale structures like CMEs. The 3D reconstruction of CMEs can be effectively performed only when a configuration of multiple spacecraft

[9]Report on the STEREO Spacecraft visiting the Lagrange Points (last accessed November 2024): https://svs.gsfc.nasa.gov/3591

with separation angles of at least 10° are utilised (Bosman, 2017, p. 91). The separation angles between the STEREO probes and SOHO near Earth spanning 10° to 170° provide unprecedented opportunities for achieving accurate 3D reconstructions. However, it is important to recognise that the effectiveness of reconstructing an event from these viewpoints depends on various event-specific factors, such as the uniformity of its density distribution, making the separation angles invaluable yet approximate indicators. The time periods during which the spacecraft exhibit these unique constellations are listed in Table 5 and were determined using data from NASA's STEREO Orbit Tool[10].

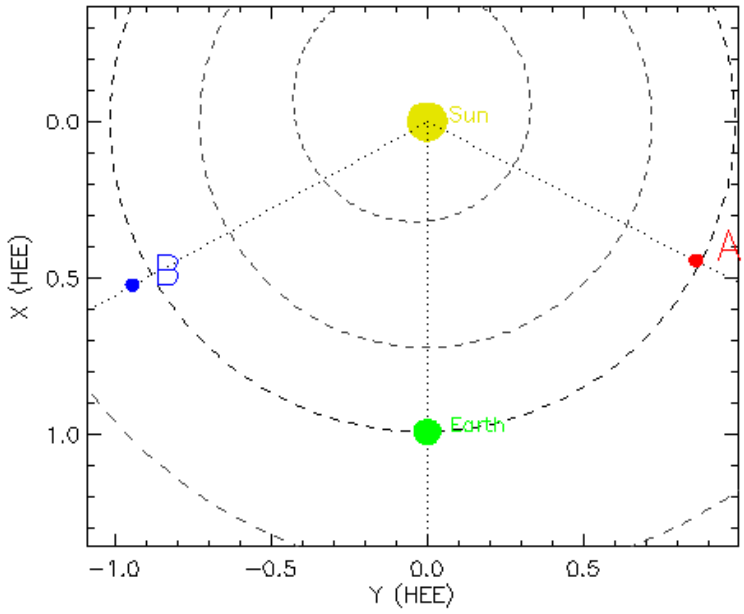

Figure 15: Positions of the STEREO spacecraft relative to the Sun and Earth on November 1, 2009. STB was located near L_5, enabling stereoscopy. Created with NASA's STEREO Orbit Tool[10].

Additionally, the STEREO mission is the only mission that has performed measurements near L_5, representing another noteworthy configuration of the mission. These periods of observation are of special interest to ESA in the development of the upcoming Vigil mission (see Section 4.1 and Chapter 5), as they mimic Vigil future perspective, allowing for stereoscopic imaging and enhanced modelling of Earthward-directed CMEs with the goal of operational space weather forecasting. STB observed the Sun from near the L_5 region, between approximately August 2008 and January 2011[8], as shown in Figure 15, while STA observed the Sun from near the L_5 region between around July 2019 and May 2022 (see Table 5). Importantly, these observations occurred after the prime mission phase of STEREO, which already concluded in 2009, highlighting the extended utility and scientific value of the mission beyond its initial operational timeline.

[10]NASA's STEREO Orbit Tool (last accessed November 2024): https://stereo-ssc.nascom.nasa.gov/cgi-bin/make_where_gif

On October 1, 2014, contact with STB was lost behind the Sun following a planned hard reset. Unfortunately, STB lost its orientation, began spinning uncontrollably, and eventually ceased communication with Earth[11]. The loss of STB significantly reduced the availability of stereoscopic observations helpful for the 3D reconstruction of CMEs after 2014. Nevertheless, STA remains operational and continues to provide invaluable data, aiding both ongoing solar research and informing space weather forecasting models and studies.

4.4 The WIND Mission

The WIND spacecraft (Acuña et al., 1995) was launched on November 1, 1994, as part of the Global Geospace Science (GGS) program. Initially placed in a Lissajous orbit around L_1, WIND was inserted into a halo orbit around L_1 in 2020. The primary science objectives of the WIND mission include providing comprehensive studies of plasma, energetic particles, and magnetic fields, investigating fundamental processes occurring in the near-Earth solar wind, and offering baseline ecliptic plane observations for heliospheric missions[12]. WIND, together with several other missions, is part of the International Solar Terrestrial Physics (ISTP) program, which aims to improve our understanding of solar-terrestrial relations. Over its operational lifetime, WIND has contributed to numerous scientific discoveries, including refining knowledge about solar wind structure, magnetic reconnection, and interplanetary shocks.

To achieve its objectives, WIND carries a range of instruments to measure and analyse the solar wind environment. The WAVES suite (Bougeret et al., 1995) measures radio and plasma waves using three orthogonally arranged magnetic search coils. The Magnetic Field Investigation (MFI) (Lepping et al., 1995) uses fluxgate magnetometers to measure DC vector magnetic fields, the Energetic Particles: Acceleration, Composition and Transport (EPACT) instrument (von Rosenvinge et al., 1995) observes energetic particles over a wide range of energies, and the Solar Wind and Solar Wind and Suprathermal Ion Composition Experiment (SMS) (Gloeckler et al., 1995) monitors the composition, temperature, and speed of major solar wind ions. Combined data from these instruments provide a multifaceted view of the solar wind and its interactions with Earth's magnetosphere, enhancing our understanding of fundamental plasma processes and supporting other heliospheric missions.

While the WIND mission has been a cornerstone in solar wind and heliospheric research, other missions such as the Advanced Composition Explorer (ACE) (Stone et al., 1998) and Deep Space Climate Observatory (DSCOVR) (Burt and Smith, 2012) missions, both still in operation, have also made significant contributions to the field. ACE,

[11] STB Report on the Website of the STEREO Science Center (last accessed November 2024): http://stereo-ssc.nascom.nasa.gov/behind_status.shtml

[12] NASA WIND Homepage (last accessed November 2024): https://wind.nasa.gov/index.php

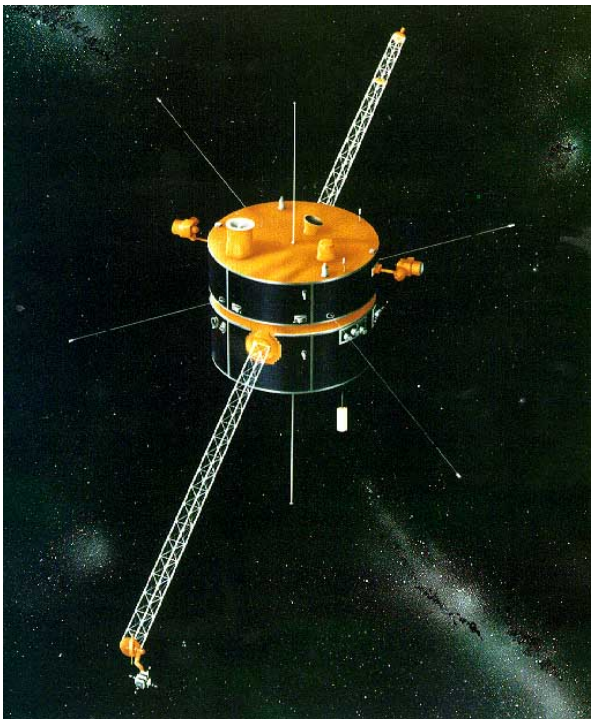

Figure 16: Image of the WIND probe. From NASA (2005).

launched in 1997, has provided detailed measurements of solar wind composition and magnetic fields, complementing WIND's observations. DSCOVR, launched in 2015, focuses on real-time solar wind monitoring and with a secondary role in Earth climate observations from the L_1 point. Although these missions share similar objectives and operational locations with WIND, they are not discussed further in this work, yet their data remains invaluable for advancing space weather research.

4.5 Coronagraphs

A coronagraph is a specialised telescope designed to observe the solar corona by blocking the intense light from the visible solar disk. By simulating a solar eclipse, coronagraphs enable the study of faint coronal details that would otherwise be obscured by the Sun's overwhelming brightness, primarily through isolating Thomson scattered light (see Section 3.2). The concept of the coronagraph was first introduced by Bernard Lyot in 1930 (Lyot, 1939).

Externally occulted Lyot coronagraphs are particularly effective in reducing stray light compared to internally occulted designs. However, due to diffraction limitations, these externally occulted systems are unable to image the innermost regions of the corona. A notable example of an externally occulted Lyot coronagraph is the LASCO Coronagraph 2 (C2) aboard the SOHO spacecraft, its design is depicted in Figure 17.

In the design of the C2 coronagraph (Brueckner et al., 1995), beams of light enter from the left and form a coronal image at the focal plane (F). The external occulter ($D1$)

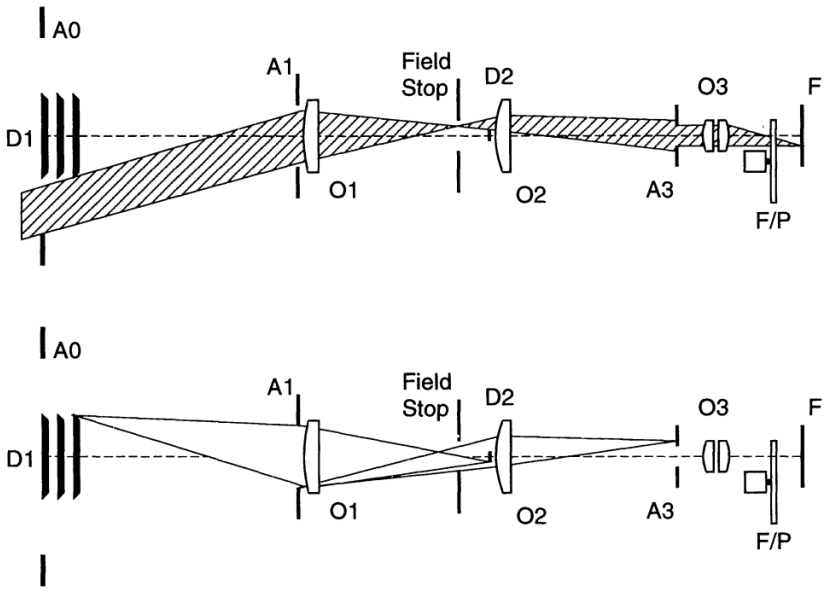

Figure 17: Diagram illustrating the optical components and light paths in the C2 coronagraph on the SOHO spacecraft. From Brueckner et al. (1995).

blocks direct light from the solar disk, allowing coronal light to pass around it. The objective lens ($O1$) reduces scattering and projects an image of the external occulter onto the internal occulter ($D2$), which further suppresses residual light from the solar disk. The light then passes through the 'Lyot stop' ($A3$), which blocks diffracted light originating from the entrance aperture ($A1$). Finally, the camera objective ($O3$) forms the final image. This design effectively demonstrates the suppression of stray light, enhancing the clarity and contrast of the coronal images.

4.5.1 SOHO/LASCO C2 and C3

The Large Angle and Spectrometric Coronagraph (LASCO) instrument (Brueckner et al., 1995) on board the SOHO spacecraft constitute a triple coronagraph system with nested, concentric annular FOVs. Each of the three coronagraphs—LASCO Coronagraph 1 (C1), C2, and LASCO Coronagraph 3 (C3)—is externally occulted and utilises a 1024×1024 Charge-Coupled Device (CCD) camera as a detector.

Following the loss and subsequent recovery of the SOHO spacecraft, C1 ceased operations. Consequently, observations have relied on C2 and C3. C2, as depicted in Figure 17, images the solar corona between heliocentric distances of $1.5\,\mathrm{R}_\odot$ and $6\,\mathrm{R}_\odot$. Extending the observational range, C3 images the corona from $3.7\,\mathrm{R}_\odot$ to $30\,\mathrm{R}_\odot$. The overlapping FOVs between C2 and C3 enable uninterrupted tracking of CME evolution, particularly valuable in this work. Both C2 and C3 have an image cadence of 12 minutes.

To significantly reduce stray light, observations are conducted in three distinct linear polarisation states, and the polarised brightness is computed from these images (Billings, 1966). Each imaging sequence includes three images captured with different polarisers.

Additionally, C2 and C3 are equipped with seven broadband and narrowband filters covering a spectral range from 400 nm to 1050 nm. This extensive spectral coverage provides detailed information not only about white-light scattering by free electrons but also about the composition, temperature, and density of the coronal plasma.

4.5.2 STEREO/SECCHI COR2

The STEREO/SECCHI Coronagraph 2 (COR2) is an externally occulted Lyot coronagraph developed based on the successful operation of C2 and C3. It is part of the SECCHI instrument suite (Howard et al., 2008) on board the STEREO spacecraft, alongside the STEREO/SECCHI Coronagraph 1 (COR1). While COR1 images the corona between $1.4\,R_\odot$ and $4\,R_\odot$ at a cadence of 8 minutes, COR2 has a nested angular FOV of 8°, imaging the corona between $2.5\,R_\odot$ and $15\,R_\odot$ with a cadence of 15 minutes. The combination of COR1 and COR2 provides comprehensive imaging of the inner and outer corona, enabling detailed studies of CME propagation through the extended corona and their transition into interplanetary space. Both coronagraphs utilise 2048 × 2048 pixel CCD arrays.
Similar to C2 and C3 on SOHO, COR2 captures sequences of three linearly polarised images. This polarisation sequence is completed in eleven seconds, ensuring sufficient signal-to-noise ratio while minimising motion blur for dynamic events like CMEs. Low-resolution total brightness images from COR2, computed on board, are continuously transmitted to Earth and are valuable for space weather forecasting purposes.

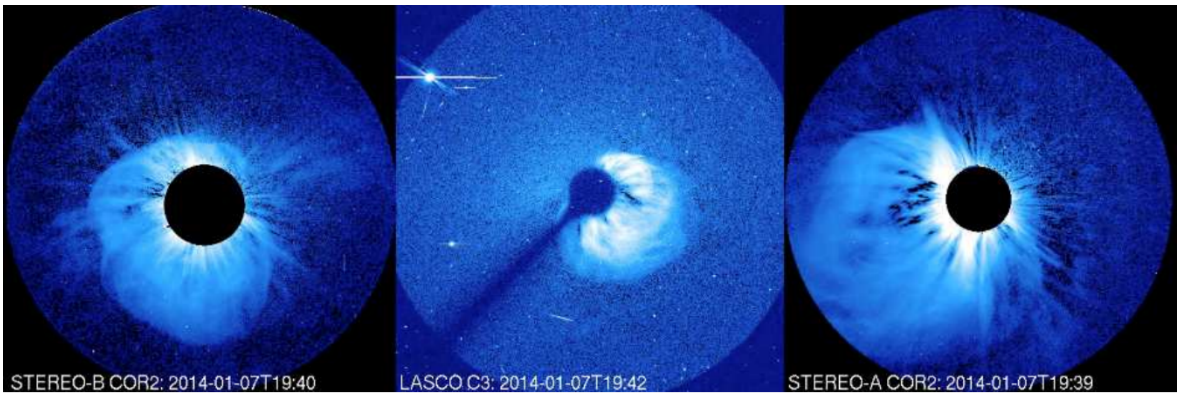

Figure 18: Observations of a CME on January 7, 2014 around 19:40 UT recorded by (left to right) COR2B, C3 and COR2A. From Mays et al. (2015).

The COR2 on board STA (COR2A) and COR2 on board STB (COR2B) telescopes are identical except for slight differences in the sizes of their occulters and offsets in their boresights. Figure 18 shows images of the same CME recorded by COR2A and COR2B, as well as an image taken by C3 from a near-Earth perspective.

5 Motivation

This chapter outlines objectives and results of an ESA study assessing multi-viewpoint observations for space weather forecasting. It highlights challenges in interpreting events of complex nature, particularly through a 2010 CME case study. The need for robust methodologies to evaluate forecasting approaches is emphasised, which informs and motivates the subsequent analysis in this thesis.

5.1 The 'L5 Data Utilisation' Study: Successes and Unresolved Challenges

Between 2019 and 2023, ESA conducted a study on "Use of L5 Data in CME Propagation Models", also called *L5 Data Utilisation* study[13], coordinated by RAL Space (UKRI STFC). An international team, centered around a project group from a consortium involved in developing ESA's planned operational space weather mission Vigil (see Section 4.1), collaborated to systematically and quantitatively evaluate the benefits of combining data from L_5 with L_1 and near-Earth observations. Their work aimed to enhance operational space weather forecasting capabilities by assessing the added value of multiple viewpoints being available. The study also explored how these data sources could be integrated into existing models, improving prediction accuracy. As part of the German contribution lead by Dr. V. Bothmer, I took part in the study from 2022 onwards.

The study employed a series of Use Cases (UCs) to assess the potential utilisation of Vigil coronagraph and HI data within current space weather forecasting operations. The UCs focussed, among other things, on:

- Improving operational CME onset detection.
- Improving operational predictions of ICME arrivals at Earth.
- Improving operational solar wind predictions.
- Enhancing forecasts of SEP events.

Additionally, these UCs considered the effects of varying image resolutions and cadences on CME analyses.

Our contribution centred on UC1, which investigated the potential improvements in CME onset detection and characterisation when integrating data from multiple vantage points (L_1 and L_5). The assessments in UC1 are based on a standard set of 15 CMEs selected from intervals when one of the STEREO spacecraft (see Section 4.3) provided an L_5-like viewing geometry.

[13] ESA webpage on the study: https://swe.ssa.esa.int/de/use-of-l5-data-in-cme-propagation-models (last accessed March 2025)

Table 6: List of the 15 CME events analysed in the 'L5 Data Utilisation' study, showing the first time each CME was observed in the COR2 FOV and the spacecraft's approximate heliolongitude relative to Earth's position. Negative values indicate that the observing STEREO spacecraft was trailing behind Earth on a similar orbit, thus simulating an L_5-like vantage point close to $-60°$.

CME-ID	COR2 entry time (UT) y/m/d:hm	STEREO location [deg]
UC1-CME-1	2010/04/08:0439	−71 (ST-B)
UC1-CME-2	2010/10/26:0709	−81 (ST-A)
UC1-CME-3	2021/11/02:0253	−37 (ST-A)
UC1-CME-4	2010/05/24:1439	−70 (ST-B)
UC1-CME-5	2009/12/16:0339	−67 (ST-B)
UC1-CME-6	2011/06/14:0754	−93 (ST-B)
UC1-CME-7	2010/03/19:1224	−71 (ST-B)
UC1-CME-8	2010/04/03:1009	−71 (ST-B)
UC1-CME-9	2021/10/28:1553	−37 (ST-A)
UC1-CME-10	2020/12/07:1624	−57 (ST-A)
UC1-CME-11	2020/09/30:0309	−61 (ST-A)
UC1-CME-12	2021/02/10:1139	−56 (ST-A)
UC1-CME-13	2011/05/25:0454	−93 (ST-B)
UC1-CME-14	2011/07/11:1139	−93 (ST-B)
UC1-CME-15	2011/10/28:2159	−101 (ST-B)

The event selection process followed these criteria:

- A sufficiently large number of events to support robust statistical conclusions about L_5 data usage.
- A diverse range of CME types.
- Inclusion of Halos, to examine the influence on velocity and Earth arrival time estimates.
- Inclusion of CMEs narrowly missing Earth, to study improvements in orientation and direction estimates.

Coronagraph data from the C2 and C3 instruments are available since 1996 (see Section 4.5.1), providing a long-term observational baseline. Both STEREO spacecraft have traversed regions approximately $\pm 30°$ around the L_5 point for about 2.5 years each (further detailed in Table 5), thus offering suitable observational phases for the study. The final set of selected events is listed in Table 6.

The study's results show that determining the initial conditions of CMEs is still challenging, even with multi-perspective views. However, integrating L_5 coronagraph observations appears to improve both CME characterisation and arrival time forecasts,

though the degree of enhancement remains difficult to quantify. Further, using HI data from larger elongations refines prediction accuracy but also reduces the available lead time[13].

Several potential next steps have been identified, future efforts may focus on integrating currently independent models and tools into a unified framework, facilitating model intercomparison and the development of ensemble predictions. Other prospective directions include the increased use of data assimilation methods and machine learning techniques, with the aim of automating analyses and providing enhanced decision support for space weather forecasters.

While the Study demonstrated clear benefits of multi-viewpoint observations, our analyses encountered challenges in handling events of a more complex nature. A recurring difficulty arose when having to interpret the nature of events involving multiple, overlapping CMEs—a scenario where a single, and in one case even multiple perspectives could not always immediately resolve resolve ambiguities in feature identification. These interpretive uncertainties directly impacted the results obtained when applying reconstruction techniques, complicating model comparisons and highlighting fundamental limitations in current forecasting methodologies.

This underscores the need for systematic strategies to avoid interpretation-driven uncertainties, a requirement that extends beyond this study to forecasting evaluation generally. The following subsection examines these challenges through a case study: the ambiguities encountered during the analysis of the April 8, 2010 event, illustrating how observational limitations and interpretive subjectivity can influence the resulting reconstruction of the CME, and ultimately propagate into forecasting uncertainties.

5.2 Ambiguities in Interpreting the 2010-04-08 Event: A Case Study

One of the events included in the *L5 Data Utilisation* study's standard set (see Table 6 is a CME observed by SOHO and both STEREO spacecraft on April 8, 2010, identified in Table 6 as UC1-CME-1. A more detailed account is provided by Kay et al. (2016), who note that "At 3:30 UT on 2010 April 8 a CME erupted from AR 11060, which was located at N25° E16° as viewed from Earth".

Accurate 3D modelling of this event using tools such as the GCS model (see Section 3.4.1) requires a well-founded interpretation of the observed signatures. In other words, anyone applying the model to coronagraph images must carefully distinguish which bright structures represent the CME of interest and which do not. This distinction is crucial, as it determines the validity of the GCS reconstruction.

Figure 19 shows images created with of the 'GCS in Python' tool which a user attempting to reconstruct the CME from all three viewpoints simultaneously at 05:54 UT on April

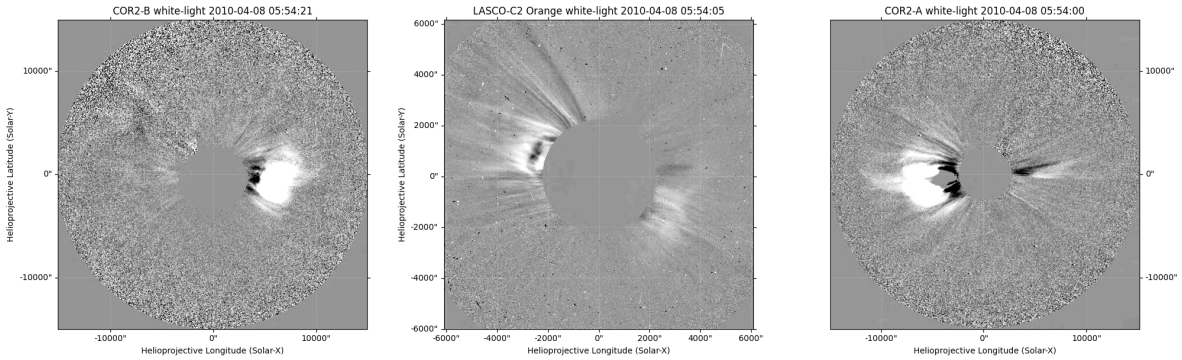

Figure 19: Coronagraph observations of CME signatures at 05:54 UT on April 8, 2010, recorded by (left to right) COR2B, C2, and COR2A. The presented images are running-difference images created with the 'GCS in Python' tool; see Section 7.1.1 for details on image processing and data origin.

8, 2010 is presented with. The tool itself, and procedures for fitting the GCS model in multiple viewpoints are described in Section 7.1.1 and Section 7.1.2, respectively. In the COR2A and COR2B FOVs, a strong, Earthward-directed CME structure is visible. Moreover, the C2 perspective shows strong brightness to the upper-left of the occulting disk and a weaker brightening to the lower-right of it. Without considering a longer time interval or additional data sources, this might lead one to conclude that the features visible to either side of the C2 occulting disk at 05:54 UT belong to a single CME of large angular width.

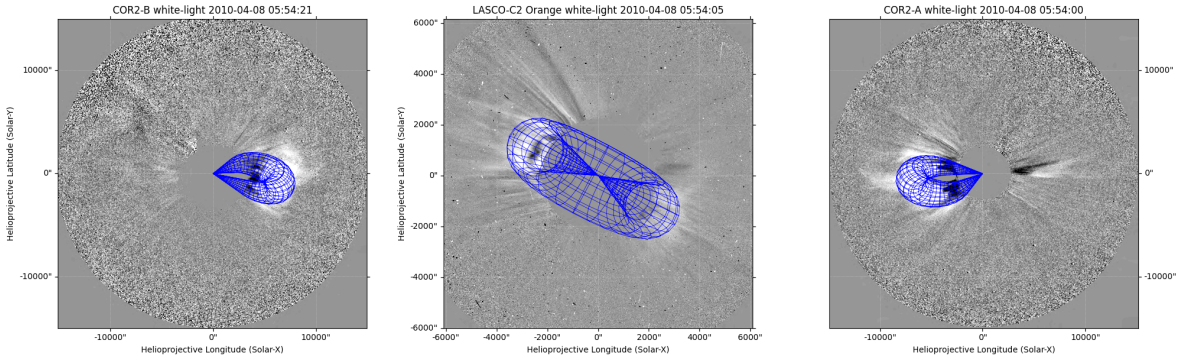

Figure 20: GCS fit interpreting coronagraph observations at 05:54 UT on April 8, 2010, recorded by (left to right) COR2B, C2, and COR2A, as a Halo CME of large angular width. The presented images are running-difference images created with the 'GCS in Python' tool; see Section 7.1.1 for details on image processing and data origin.

Following this line of interpretation, a reconstruction via the GCS model can be obtained to encompass both signatures seen in C2 at that time as part of the same CME, yielding a wide full-Halo reconstruction. An example of such a result is shown in Figure 20. In the 'L5 Data Utilisation' study, similar reconstructions were created by project group members using either only one or two of the three available viewpoints, since the study

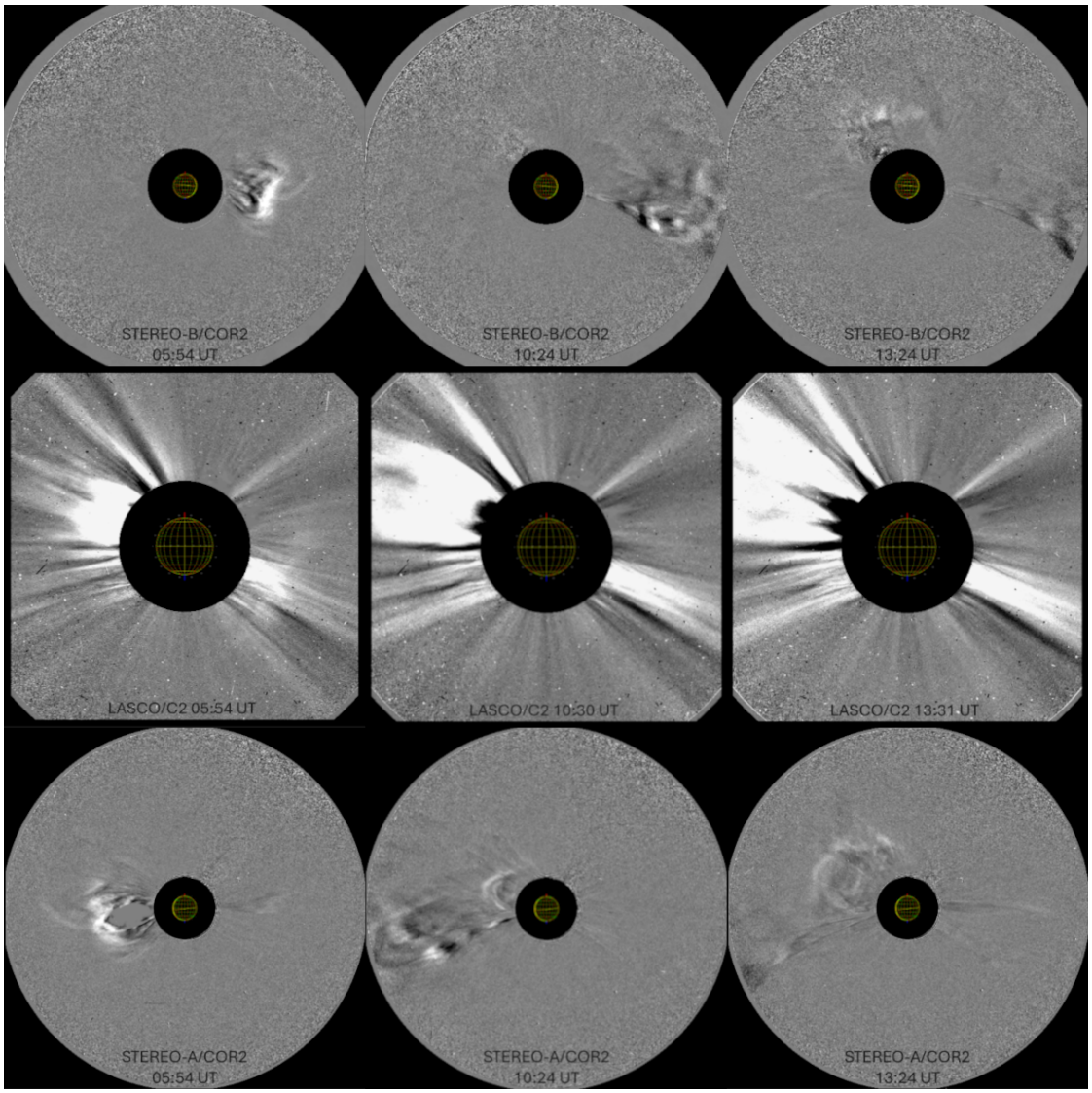

Figure 21: Composite image depicting the evolution of two CMEs observed on April 8, 2010, as captured by (from top to bottom) COR2B, C2, and COR2A. Observation times are approximately (from left to right) 05:54 UT, 10:24 UT, and 13:24 UT. Images were obtained using JHelioviewer[3].

focused on the combined L_5+L_1 vantage point scenario, with the single L_1 viewpoint serving as a control reference.

However, this single-event interpretation aligns only with the STEREO viewpoints and not with the LASCO observations. Kay et al. (2016) point out that "A separate CME without a strong EUV signature erupts more than 40° westward of the CME considered". They further note "Their separation is sufficient that we can model the evolution of the 2010 April 8 CME without considering their interaction. However, the two CMEs overlap in coronagraph images". By examining a more extended time range, particularly when considering the data provided by COR2A, the existence of this second CME, CME-2, becomes evident.

Figure 21 presents images recorded at later times, where CME-2 is clearly visible in

COR2A from 10:24 UT onwards. While its also identifiable in COR2B, the additional signature is much fainter and appears even later than in COR2A. These observations reveal why CME-2 can be easily overlooked, even when considering the three viewpoints together: (1) Typically, later times may not be considered because CME-1 is already leaving the FOVs of COR2A and COR2B at 10:00 UT, and (2) even if these later observations are included, CME-2 is faint in COR2B, while CME-1 is faint in LASCO images, and an overlap exists, making them harder to recognise and easier to confuse. Most significantly, even when accounting for reason (1), relying solely on the L_1 perspective of SOHO, or in the special case of this event, even just on the combination of the near-L_5 perspective of STB and L_1, makes recognising the existence of two distinct CMEs exceedingly difficult, as reason (2) obscures their distinction (in both of these scenarios) heavily.

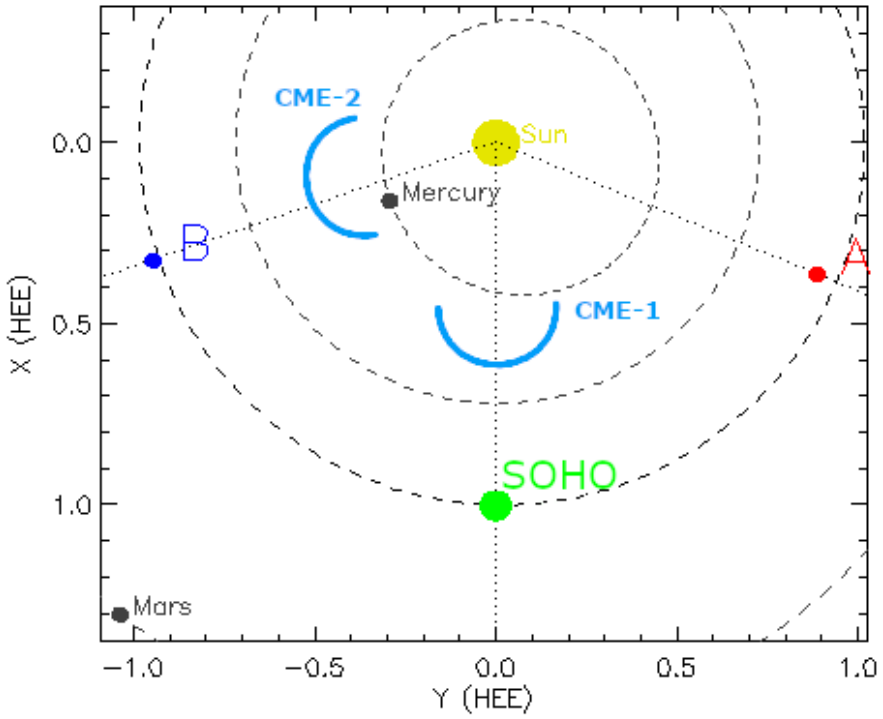

Figure 22: Approximate longitudinal directions of two CME fronts observed on April 8, 2010, along with the positions of STA and STB relative to the Sun and SOHO near Earth. The height and spatial dimensions of the CME fronts are not to scale and included for illustrative purposes only. The plot of the positions was obtained using NASA's STEREO Orbit Tool[10], the CME fronts and annotations were added.

At first it may seem counter-intuitive that both CMEs are already visible in C2 around 05:54 UT, yet CME-2 only starts to appear in COR2A at about 10:24 UT and in COR2B at around 13:24 UT. This discrepancy arises from two factors: the difference in their projected velocities and the different inner FOV limits of the coronagraphs.

Figure 22 illustrates, in a top-down perspective of the ecliptic plane, the positions of the STEREO spacecraft relative to Earth (and thus SOHO), and the approximate longitudinal directions of the two CMEs. The height of the CME fronts (or distances from the Sun) and spatial extension (or angular width) are not to scale.

On April 8, 2010, the separation angle between STA and Earth was about 68°, and the angle between the two STEREO spacecraft was around 139°. Under these geometric conditions, CME-1 appears as a (close to) plane-of-sky event in STA and STB, while CME-2 does not, leading to lower projected velocities and a delayed entrance into the FOVs of their COR2 instruments. From SOHO's vantage point, CME-2 appears more like a plane-of-sky event in C2, so it is detected there earlier than CME-1's Halo-like signature, and a similar reasoning applies to COR2B, with the roles of the two CMEs reversed.

These viewing-angle effects are magnified by the differing FOVs: The COR2 instruments start observing from $2.5\,R_\odot$, whereas C2's observation starts from $1.5\,R_\odot$. The faint appearance of CME-2 in COR2B (and similarly CME-1 in C2) can be attributed to the reduced Thomson scattering efficiency for Halos, as discussed in Section 3.3.

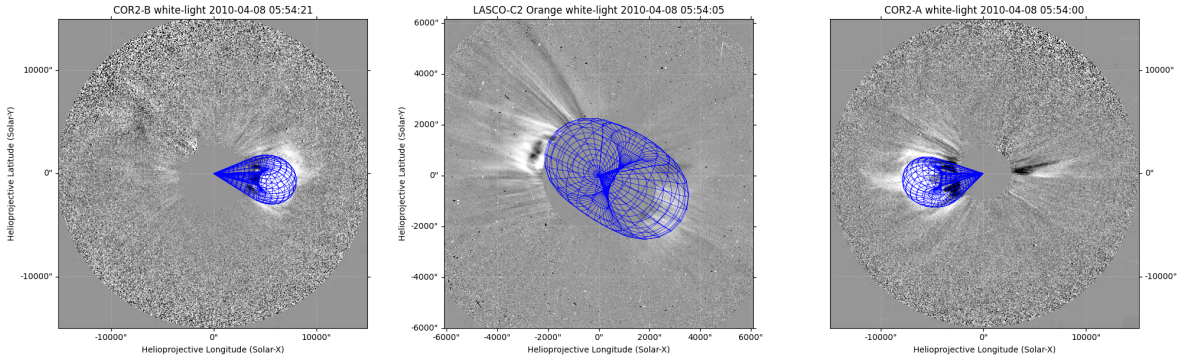

Figure 23: GCS fit interpreting coronagraph observations at 05:54 UT on April 8, 2010, recorded by (left to right) COR2B, C2, and COR2A, as a Halo CME of small angular width. The feature in the upper left of C2's view is excluded as belonging to a separate CME. The presented images are running-difference images created with the 'GCS in Python' tool; see Section 7.1.1 for details on image processing and data origin.

This more refined interpretation—one that accounts for both CMEs—led to an improved reconstruction proposed by us in the project, presented in Figure 23. In this new fit, the brightness feature to the upper-left of C2's occulting disk is identified as CME-2 and thus, was not considered in the modelling process. The views of COR2A and COR2B are considered for the fit similarly as before in Figure 20, since the visible signature at 05:54 UT can be associated with CME-1.

To return to the greater difficulties encountered when relying on more limited vantage points, such as solely SOHO, or even the combination of SOHO and STB: Correctly identifying the two distinct CMEs from the coronagraphic images becomes significantly

more difficult. The faintness of the Halo-like signatures and partial overlap between the two signatures obscures the true nature of the event, which is, in this case, much easier understood in conjunction with the view of COR2A.

5.3 Addressing Common Challenges with Multi-Viewpoint Analysis

The 2010-04-08 event highlights a less obvious but crucial advantage of multi-viewpoint observations. As detailed in Section 5.1, combining data from multiple vantage points not only enhances CME reconstruction accuracy but also minimises potential errors that propagate into ICME arrival-time predictions in coupled reconstruction and propagation workflows. Critically, multi-perspective analysis helps resolve ambiguities and prevent misinterpretations of fundamental event characteristics that might persist when only one viewpoint, in more rare cases also when only two viewpoints are available.

Current event catalogues, such as the near-Earth ICME list by Richardson and Cane (2024) and the 45-event dataset by Kay and Gopalswamy (2017), often include events susceptible to these dangers without adequately acknowledging it. This oversight mixes inherent model limitations with event-specific complexities, complicating efforts to evaluate models and improve forecasting accuracy. Moreover, uncertainties in geometric reconstructions themselves remain insufficiently quantified. While Verbeke et al. (2022) established lower error bounds for GCS parameters using synthetic data, models applied to real coronagraphic imagery likely face higher uncertainties. Catalogue collections like LLAMACoRe (Kay and Palmerio, 2024) partially address this by aggregating multiple reconstructions, but persistent misinterpretations, such as those encountered in the 2010-04-08 case, remain unresolved, potentially yielding different reconstruction outcomes.

This work addresses these challenges through two key strategies. On one hand, the three simultaneous perspectives from STA, STB, and SOHO are used to minimise projection effects and enables accurate interpretation of the true 3D structure, as described in Chapter 7. On the other hand, focusing on isolated CME-ICME pairs with unambiguous signatures (see Chapter 6) creates a controlled dataset that isolates model performance from confounding factors like misinterpretations or interactions with other solar phenomena. All together, this establishes an ideal baseline for evaluating the developed forecasting approaches, as discussed in Chapter 8.

The resulting insights provide a foundation for incrementally introducing complexities in future studies while maintaining analytical clarity. Also, this methodology aligns with the anticipated capabilities of the Vigil mission, as well as offers a framework for distinguishing between model-dependent uncertainties from true physical processes in space weather forecasting.

6 Event Selection

This chapter defines three criteria for selecting CME events suitable for the analysis performed in Chapter 7. Using two reference catalogues, a list of five events is compiled, supporting reliable evaluation of forecasting methods in Chapter 8 with minimal confounding factors.

6.1 Criteria for Selecting Events

To identify CME events that align with the specific objectives of this study, a well-defined set of selection criteria is established. These criteria aim to isolate well-observed events that appear distinct from other concurrent solar activities, thereby minimising commonly known challenges in CME modelling and ICME arrival time predictions (e.g., those discussed in Section 5.2). By ensuring a controlled event selection, this approach reduces uncertainties arising from complex interactions between multiple solar events. It is important to emphasise that the selection criteria do not favour or exclude CMEs or their interplanetary counterparts based on intrinsic properties such as size, velocity, or magnetic structure. Instead, the focus is on identifying cases where complicating factors are absent, ensuring that the selected events provide the clearest possible basis for analysis. The necessity of such clear criteria is underscored by the fact that these factors are rarely addressed in the literature (see Section 5.3). Given these considerations, a new set of selection criteria is proposed here:

Criterion 1: Three-viewpoint observations must be available from at least one day before until one day after the first appearance of the event in the respective coronagraphic FOV, with the satellites positioned in a constellation that enables effective 3D reconstruction of CME structures.

Criterion 2: The CME signature should be identifiable in the coronagraphic images as a discrete feature, with minimal interference from other solar activity and no temporally adjacent CME events that are likely to introduce interactions.

Criterion 3: A reliable identification of an isolated, single-event ICME signature as the CME's interplanetary counterpart must be present in near-Earth solar wind measurements.

Criterion 1 ensures that sufficient data are available for a thorough evaluation of Criterion 2 and Criterion 3. For instance, Section 5.2 illustrates how observations from three different viewpoints are crucial to uncover the true nature of certain CME events that might otherwise be misinterpreted if data from only one or two viewpoints are

used, especially if coupled with an extended temporal window around the event. Multi-viewpoint data also help reveal signatures of other solar phenomena that might overlap with a CME events signature from a specific viewpoint, as well as determine whether interactions with additional CMEs or ICMEs might be occurring due to temporal or spatial proximity.

A further motivation for using data in accordance with Criterion 1 is that CMEs appearing as Halos in a single viewpoint often show significantly diminished scattering of light toward the observer, thereby reducing their visibility and making accurate assessments more challenging (see Section 3.3). Since many ICMEs detected near Earth originate from CMEs that appear as Halos in SOHO's FOV, a combination of multiple vantage points is imperative for maximising accuracy in the determination of CME parameters, adding information to distinguish between projection effects and actual 3D structures. (see Section 5.1). In part, this is due to multi-viewpoint observations reducing ambiguity in reconstructing the 3D structure of CMEs, provided the spacecraft separation angle is at least 10° (see Section 4.3). Such observations can also improve the distinction between a CME's shock and its leading edge (see Section 3.4). The time span during which events were captured under a suitable spacecraft constellation for Criterion 1 is provided in Table 5.

Criterion 2 and Criterion 3 serve to exclude events that exhibit specific indicators of interactions likely to interfere with the application or performance of the models, as introduced in Section 3.4. In particular, concerning Criterion 2, significant deflection or interactions with additional CMEs may alter CME evolution. From an observational standpoint, multiple CMEs may overlap or combine with other solar phenomena (e.g., coronal streamers), complicating analyses (see Figure 8). For Criterion 3, similar deflections or rotations can affect ICME kinematics when interactions with other ICMEs occur, underscoring the importance of isolating single-event signatures for this study.

Even within the time frame defined by Criterion 1, near-Earth satellites and other spacecraft have recorded a substantial amount of data that might fulfill the aforementioned requirements. General compilations of observed CME events, such as the *SOHO LASCO CME Catalog* (Gopalswamy et al., 2025), likewise encounter an overload of data entries that must be carefully filtered. Consequently, to achieve an effective selection that aligns with the objectives of this study, established lists and catalogs of events that have already been filtered according to certain criteria are utilised. In the following, existing catalogues that aid in selecting events that meet the criteria outlined above are introduced.

6.2 Reference Catalogues of CMEs and ICMEs

6.2.1 The List of Near-Earth ICMEs by Richardson and Cane

The *Near-Earth Interplanetary Coronal Mass Ejections Since January 1996* catalogue[14] (Cane and Richardson, 2003; Richardson and Cane, 2024; Richardson and Cane, 2010), referred to as the RC ICME list, compiled and maintained by Ian Richardson and Hilary Cane, serves as a critical resource for heliospheric, solar, and space weather research. As of this writing, it includes approximately 580 ICMEs observed from 1996 through the end of 2023.

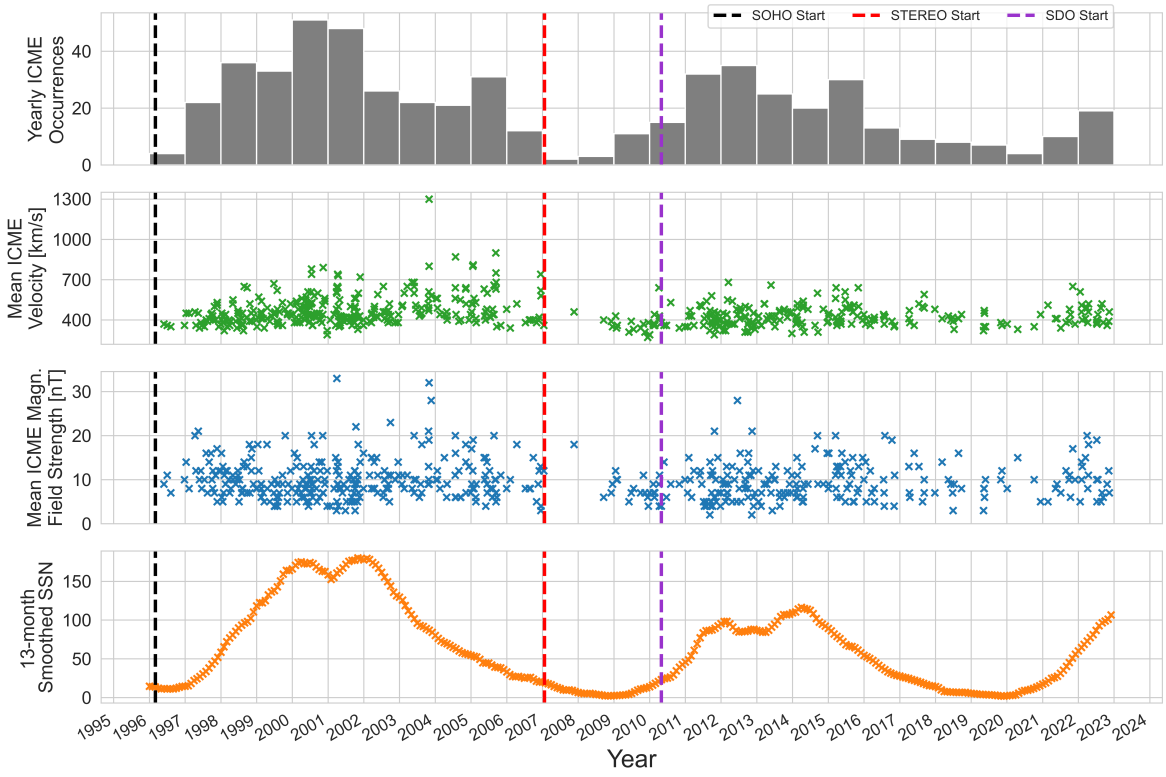

Figure 24: Overview of the ICMEs listed in the RC ICME list (slightly outdated version). Presented are the annual number of detected ICMEs, along with their mean velocities and mean magnetic field strengths, measured from 1996 through the end of 2022. The 13-month smoothed SSN is shown to contextualise ICMEs occurrence within the solar cycle's phases. Dashed vertical lines indicate the operational start of key spacecraft, including SOHO, STEREO, and SDO.

The catalogue provides detailed information about each ICME event, including, for example, the first time a disturbance is measured, and start and end times of the ICME derived from plasma and magnetic field data. It also records solar wind parameters, including average ICME speed and magnetic field strength within the event. The

[14]Dataset is available at (last accessed January 2025): https://doi.org/10.7910/DVN/C2MHTH and https://izw1.caltech.edu/ACE/ASC/DATA/level3/icmetable2.htm

quality of boundary time estimates is classified, and marginal events or those with weak signatures are flagged. For many events, a CME most likely associated with it as being the near-Sun counterpart is identified using observations from instruments like LASCO onboard SOHO. Halos are explicitly noted when observed.
Inclusion in the catalogue is based primarily on solar wind plasma and magnetic field signatures, supplemented by data on solar wind composition and charge state anomalies. Typical ICME signatures show low proton temperatures, enhanced helium-to-proton ratios, magnetic field enhancements with smooth rotations, and bidirectional suprathermal electron flows, which indicate closed magnetic field structures (Richardson and Cane, 2010). Events lacking clear ICME-like plasma or field signatures, such as corotating interaction regions, as well as marginal events with weak characteristics, are excluded.
Figure 24 illustrates trends in the catalogue data as of an earlier version only covering events until end of 2022. It depicts the annual number of detected ICMEs, mean velocity, and magnetic field strength measured in the listed events. The 13-month smoothed SSN provides context for the solar cycle, while dashed lines indicate the start of operations for key spacecraft, including SOHO, STEREO, and Solar Dynamics Observatory (SDO).

6.2.2 The 45 Events List by Kay and Gopalswamy (2017)

The event list compiled by Kay and Gopalswamy (2017) comprises 45 CME events with ICME counterparts and is scientifically valuable due to its selection criteria and comprehensive multi-spacecraft coverage. The list, hereafter referred to as the KG event list, is derived from and a subset of the RC ICME list. The events included in the list occurred between November 2007 and June 2014.
The most important of their event selection criteria states that all events have to show a clear LASCO coronal CME signature and are observed in both COR2A and COR2B coronagraph data from the STEREO spacecraft. The authors stress that they "fully rely on the RC [ICME list] identifications" for the CME counterparts (Kay and Gopalswamy, 2017). The resulting 45 events cover diverse space weather conditions, spanning two key phases of solar activity. The list further features both magnetic clouds and non-magnetic clouds or ejecta. For all featured events, the GCS model can be applied to coronagraphic images captured simultaneously from three different viewpoints, enabling robust 3D reconstructions of the CMEs.
The authors identify and document all parameters employed in their reconstruction and subsequent event analysis. These parameters include, for instance, the first observation time of each CME in COR1, the time of arrival (ToA) of the associated ICME, the reconstructed angular width, and the estimated "coronal velocity". The latter refers to the velocity assumed to follow a linear trajectory between the two time points at which

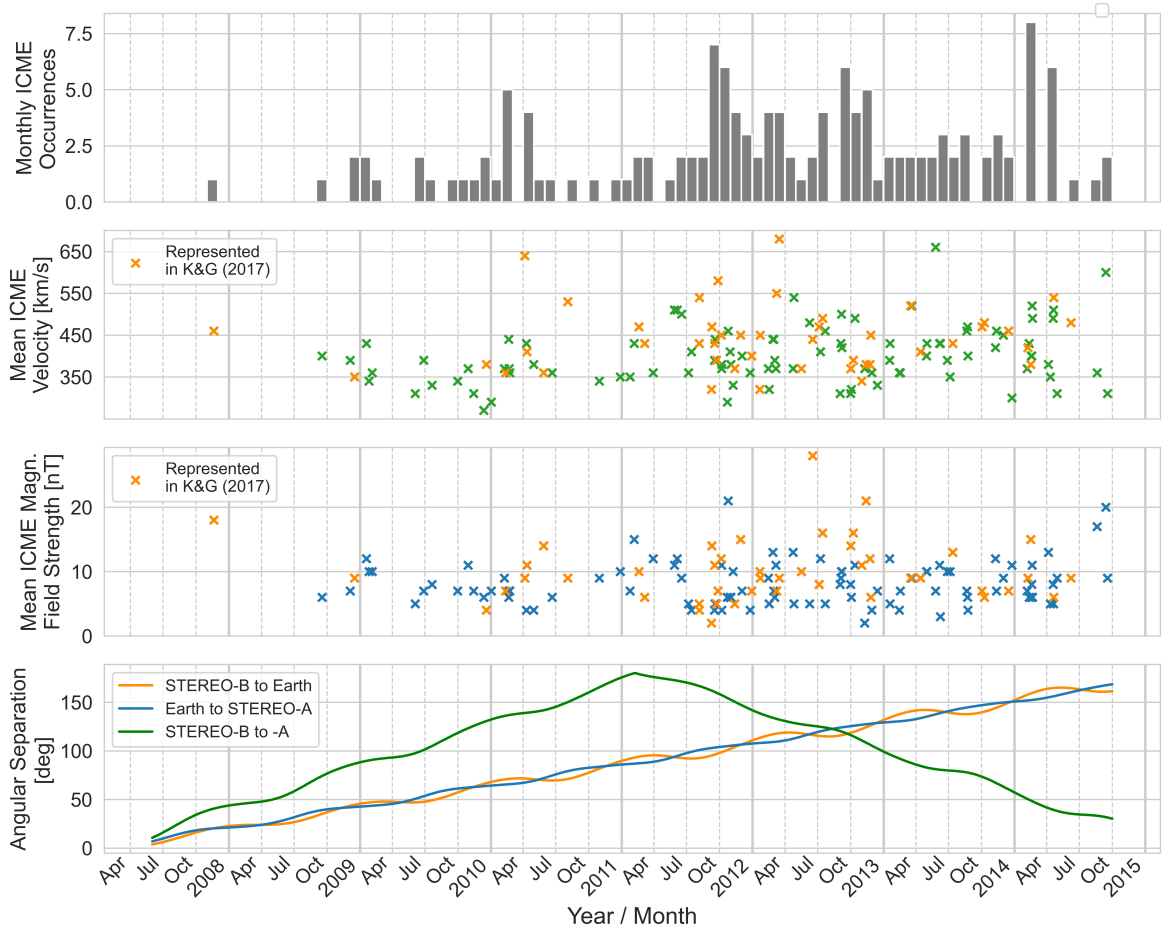

Figure 25: Subset of the RC ICME list covering June 2007 through September 2014, with events included in the KG event list highlighted in orange. Shown are the monthly counts of ICMEs, along with their mean velocities and mean magnetic field strengths. The relative separation angles between STA, STB, and Earth are also plotted, illustrating the vantage points that enabled robust 3D geometrical modelling of CMEs by the combined STA, STB, and SOHO constellation over this period.

each event was reconstructed, as defined by the authors.

Kay and Gopalswamy (2017) considered data from the ACE and WIND spacecraft for a reevaluation of the start and stop times of the ICME disturbances featured in the RC ICME list. They used conservative boundary determinations, sometimes merging times from multiple sources to capture the full extent of each event.

Figure 25 provides summarises the RC ICME list data from June 2007 to September 2014, highlighting the events also featured in the KG event list. It shows monthly ICMEs counts, mean velocities, and magnetic field strengths. Additionally, it displays the relative separation angles between STA, STB, and Earth, providing a reference for their positions during a period suitable for robust 3D CME modelling using STA, STB, and SOHO observations. The data was obtained via the `get_horizon_coord` routine from the *SunPy* package, version 5.1.5 (The SunPy Community et al., 2020).

6.3 Selection Process and Final List of Events

The selection of events for this study is a manual process that begins with the KG event list, as it already fulfils Criterion 1 as defined in Section 6.1. A detailed description of the KG event list can be found in Section 6.2.2. To satisfy the remaining two criteria, each event in the KG event list is systematically examined for compliance.

Given the intensive analytical effort required in this study, the goal is to identify a small yet representative subset of five events. Events that fail to meet any of the selection criteria are excluded from further consideration. The 45 events in the KG event list are referenced in this work using their identification (ID) numbers, consistent with the original list compiled by Kay and Gopalswamy (2017).

To evaluate the events, coronagraphic images and near-Earth solar wind data are examined using specific data products. The coronagraph images are available in movie format for different instruments. For COR2A and COR2B, the movies can be accessed at the STEREO daily movies archive. Similarly, for C2 and C3, the corresponding movies are available in the SOHO LASCO CME CATALOG -Version 2[15].

The 'STEREO movies' provide customisable options, allowing users to adjust the time coverage and playback speed. This flexibility facilitates an interactive and detailed examination of the images, enabling a more precise assessment of the observed event or eruption.

Additionally, data from the WIND spacecraft (see Section 4.4) is utilised to provide near-Earth solar wind measurements. WIND offers continuous coverage of various solar wind parameters throughout the entire time span of the KG event list, making it a valuable resource for this analysis. The OMNIWeb Plus data service[16] maintained by NASA provides 1-minute averaged magnetic field and plasma data from WIND.

The data is accessed via an interactive interface, detailed on a dedicated website[17]. For the evaluation of the 45 events in this study, the selected parameters include the total magnetic field strength and its components, as well as the plasma flow speed, proton density, and temperature. Figure 7 was generated using this interface and features the same set of parameters. As discussed in Section 3.3, this dataset is also crucial for determining precise ICMEs in-situ arrival times, which are utilised in Chapter 8.

These data products provide detailed information on each event, enabling an early evaluation of whether they meet the event selection criteria. Specifically, in relation to Criterion 2, the analysis of movies focuses on determining whether the CME signature in question can be clearly identified and distinguished from other solar phenomena. If

[15]This CME catalog is compiled and maintained at the CDAW Data Center by NASA and The Catholic University of America, in collaboration with the Naval Research Laboratory. SOHO is a joint project of international cooperation between ESA and NASA.

[16]OMNIWeb Plus Website: https://omniweb.gsfc.nasa.gov (last accessed March 2025)

[17]About-website for the interface (last accessed March 2025): https://omniweb.gsfc.nasa.gov/html/sc_merge_interface1.html

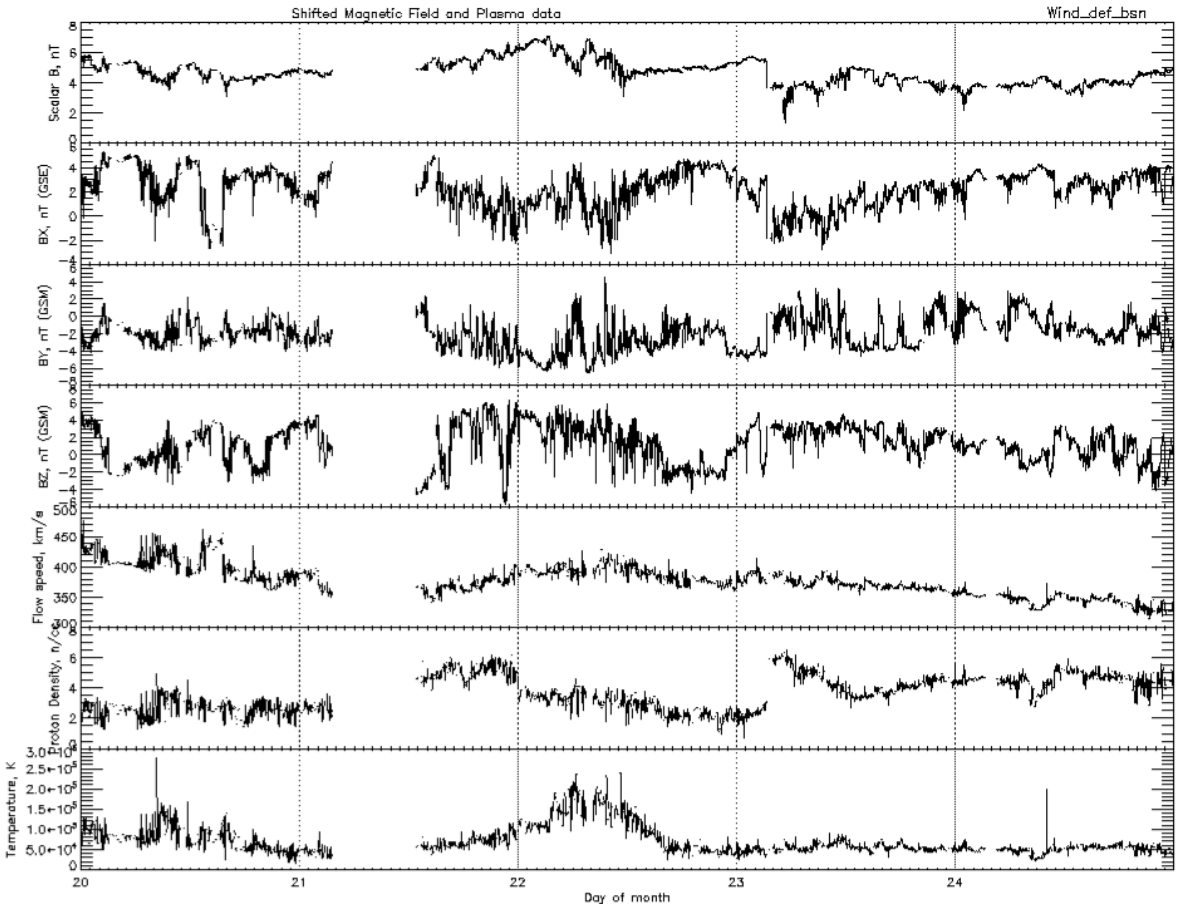

Figure 26: Solar wind data collected in-situ by the WIND spacecraft from September 20 to September 25, 2011. The panels, from top to bottom, show the magnetic field strength (B) and its GSM components (B_x, B_y, B_z), along with the flow speed, density, and temperature. While weak indicators of an ICME are present, no clear ICME signature is detected in this interval. The 1-minute averaged, bow-shock nose-shifted data were obtained from NASA's OMNIWeb Plus service[16].

multiple CMEs occur in rapid succession and the target CME cannot be unambiguously identified, the event is excluded. Two prime examples of this are event IDs 23 and 28, the first of which is illustrated in Figure 8.

To enhance visibility, slow-evolving structures such as coronal streamers can later be removed using running difference imaging (see Section 7.1.1). However, the primary concern remains the likelihood of interactions between the CME and other solar phenomena or CMEs. In cases like ID 6, where two CME signatures appear simultaneously and in close proximity, the event fails to meet Criterion 2. Similarly, for events such as IDs 7 and 33, slower CMEs erupting just hours earlier or faster ones erupting shortly afterward indicate potential interactions through drag-like forces. These scenarios prevent a clear assessment of the target CME, leading to their removal from further analysis.

Several factors can lead to events from the KG event list failing to meet Criterion 3.

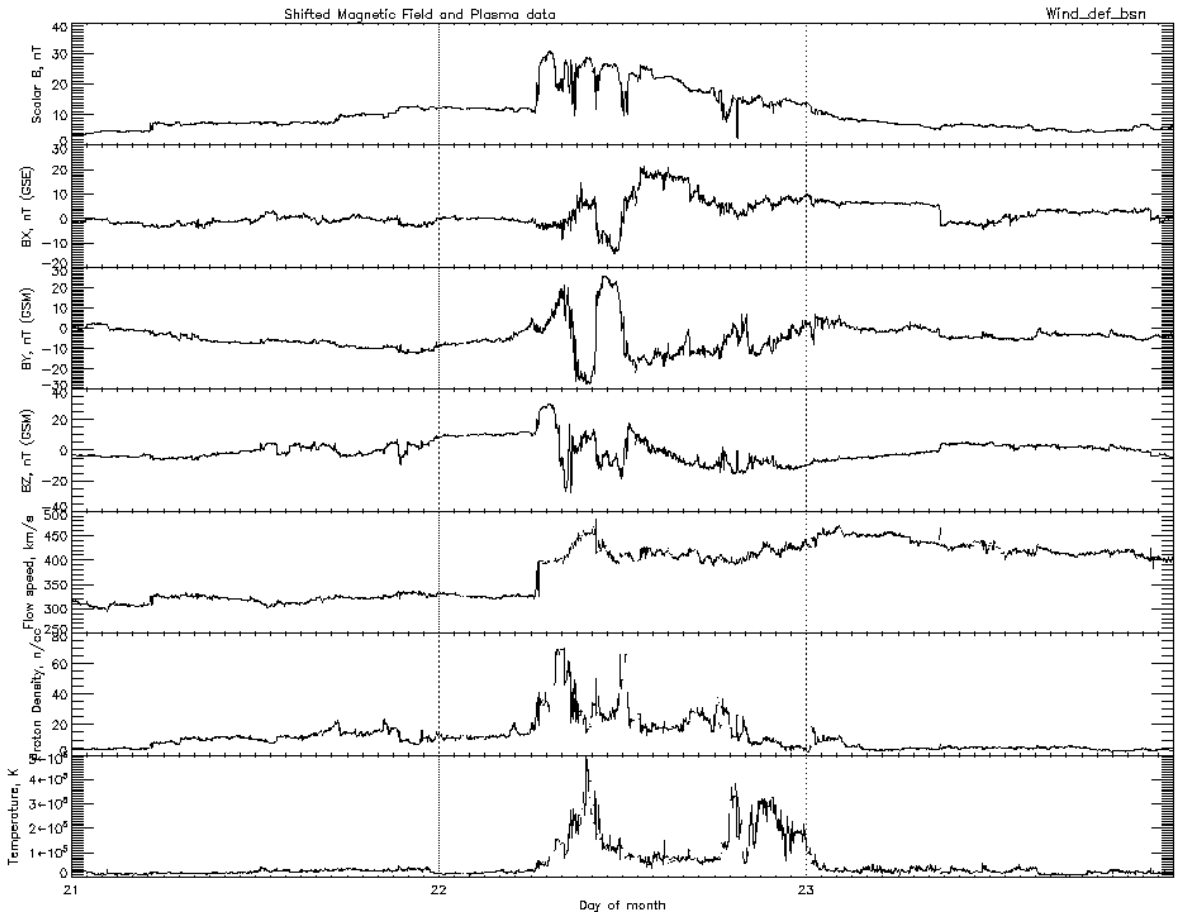

Figure 27: In-situ solar wind measurements recorded by the WIND spacecraft between January 20 and January 25, 2012. The panels, arranged from top to bottom, display the magnetic field strength (B), its components (B_x, B_y, B_z) in the GSM coordinate system, as well as the flow speed, density, and temperature. The presence of multiple distinct peaks in B strongly suggests the detection of a compound stream, where several ICMEs likely interacted and 'merged' during their propagation toward Earth. The 1-minute averaged, bow-shock nose-shifted data were obtained from NASA's OMNIWeb Plus service[16].

The first issue arises when WIND registers a weak or ambiguous ICME signature. In such cases, the event cannot be reliably analysed and must be excluded. Examples of this include event IDs 4 and 16, the latter of which is presented in Figure 26.

Another common reason for exclusion is the presence of a compound stream (see Section 3.3) instead of a distinct single-event signature. This indicates interaction between multiple structures, violating the criterion. A clear example of such a case is event ID 23. Figure 27 shows its signature.

Finally, significant gaps in the solar wind data during the event prevent a definitive validation of Criterion 3. Events such as IDs 9 and 41 fall into this category. Although some aspects of an ICME signature may be observable, the data gaps introduce uncertainty, making it impossible to rule out the influence of additional factors not captured in the dataset. As a result, these events cannot be considered for further

analysis.

Table 7 presents the final set of events analysed in this work. Each entry includes the original ID from the KG event list, along with the CME entry time into the FOV of COR2. This entry time, extracted from the previously mentioned STEREO movies, is often determined with greater precision than the actual CME launch time.

Table 7: An overview of the CME events examined in this work, listing event characteristics along with select parameters as determined in previous studies. The original event ID from the KG event list, the time at which the CME entered for the first time the FOV of any of the COR2, and the spacecraft separation angle between the two STEREO probes are listed. Additionally, the near-Earth ToA of the corresponding ICME, the "coronal velocity", and the angular width, as determined by Kay and Gopalswamy (2017), are provided.

ID	COR2 entry time (UT) y/m/d:hm	Near-Earth ToA (UT) y/m/d:hm	STEREO separation [deg]	Coronal velocity [km/s]	Angular width [deg]
15	2011/09/13:2310	2011/09/17:1535	161	460	25
31	2012/10/05:0239	2012/10/08:1800	115	800	50
34	2012/11/20:1209	2012/11/24:1200	107	650	30
36	2013/03/15:0654	2013/03/17:1500	87	1250	55
37	2013/04/11:0739	2013/04/14:1700	85	860	40

In addition, the table lists the spacecraft separation between the two STEREO probes, as obtained from the STEREO Science Center[10]. Furthermore, it includes key parameters defined by (Kay and Gopalswamy, 2017), namely the CME's coronal velocity, angular width, and the near-Earth ToA of the corresponding ICME. For a more detailed description of these parameters, refer to Section 6.2.2.

Despite the limited number of five events, they cover a substantial time range and variation in the separation angles of the STEREO probes. Kay and Gopalswamy (2017) determined the angular widths of these events range from 25° to 55°, while their approximate velocities near the Sun span from 460 to 1250 $\mathrm{km\,s^{-1}}$. This broad distribution suggests the inclusion of different CME morphologies and types.

7 Event Analysis

This chapter presents the in-depth methodology employed in this work. It describes the application of the GCS model to coronagraph images for 3D CME reconstructions and subsequent derivation of the apex- and Earthward-directed CME velocity. Moreover, this chapter presents how the other input parameters for the propagation models are determined, as well as how the DBM and MoDBM are implemented.

7.1 3D Geometric CME Modelling

Until recently, fitting the GCS model to coronagraphic observations of a given CME event required a bulky software installation and using graphical user interface (GUI) with a rather steep learning curve. However, a new implementation in *Python 3* by Freiherr von Forstner et al. (2021) has significantly streamlined the process, making the model more accessible and user-friendly. Despite these improvements, applying it to images remains challenging, as results can vary depending on the approach and expertise of the user. The following sections introduce this implementation, discuss the intricacies of the modelling process, and describe how height-time profiles, and subsequently apex-directed velocities, are derived for the events listed in Table 7.

7.1.1 Implementation of the GCS Model in Python 3

The GCS model was originally implemented in Interactive Data Language (IDL) by Thernisien et al. (2006) as part of the *SolarSoft* software package (Freeland and Handy, 1998) under `scraytrace`[18], including a GUI for model interaction. SolarSoft, developed in the 1990s, comprises a collection of IDL libraries created by members of the Yohkoh and SOHO missions and the NASA Solar Data Analysis Center (SDAC).
Python 3 shows rapid development and a large open-source community, reviewed in detail by Burrell et al. (2018) for the field of heliophysics, while being easy to read and offering powerful libraries for scientific computing. Freiherr von Forstner et al. (2021) developed a Python-based implementation of the GCS model, alongside a corresponding GUI application (see Figure 28) for reconstructing CMEs in coronagraphic images, named *GCS in Python*[19] (Forstner, 2024). It is based on functionality of the Python library *SunPy* (The SunPy Community et al., 2020) for accessing image data from different providers and performing coordinate transformations. The scientific validity of the 'GCS in Python' tool was confirmed by successfully reproducing CME reconstructions generated with the original IDL implementation (Freiherr von Forstner, 2020).

[18] Source Code is available at (last accessed February 2025):
https://hesperia.gsfc.nasa.gov/ssw/stereo/secchi/idl/scraytrace/
[19] Source Code is available at (last accessed February 2025):
https://github.com/johan12345/gcs_python

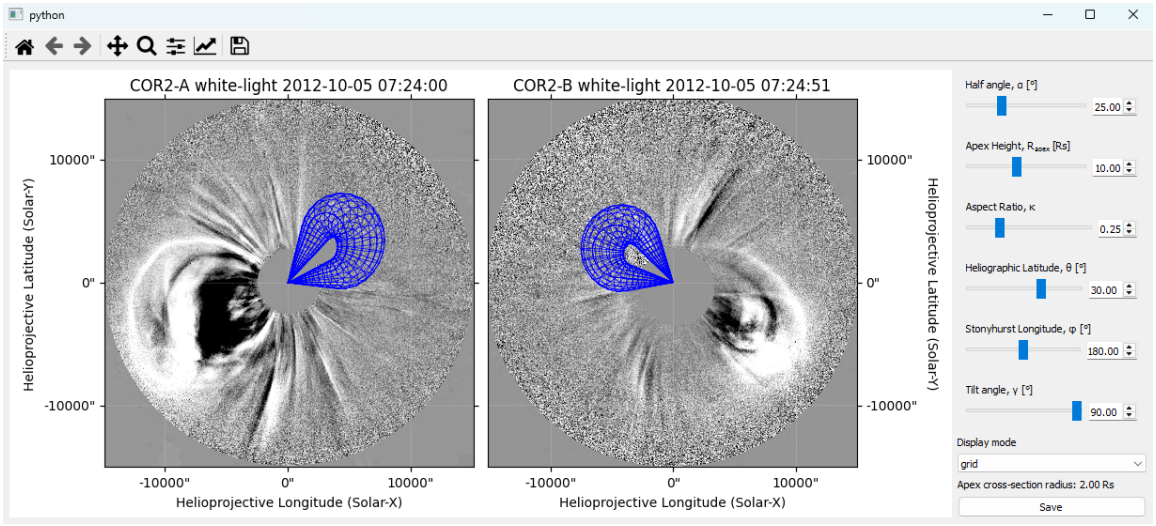

Figure 28: GUI of the 'GCS in Python' tool. Example running-difference coronagraphic images of the October 5, 2012 event observed simultaneously by COR2A (left) and COR2B (right) at around 07:24 UT are loaded. Developed by Freiherr von Forstner et al. (2021).

The GUI of the tool is launched via the command line and supports the following options:

- Specifying a date and time (UT) for image retrieval: `"YYYY-MM-DD HH:MM"`
- Selecting spacecraft, individually or in combination: `STA`, `STB`, `SOHO`
- Defining coronagraph instruments per spacecraft: `−soho C2`, `−soho C3`, `−stereo COR1`, `−stereo COR2`
- Specifying whether to compute and use running difference images: `−rd`

Coronagraph images are obtained via the *Helioviewer.org* Application Programming Interface (API)[20]. Helioviewer.org provides pre-calibrated Joint Photographic Experts Group 2000 (JPEG 2000) images that incorporate background subtraction and essential metadata. Compared to the IDL version, this approach significantly accelerates the fitting process by eliminating the need for manual Flexible Image Transport System (FITS) file downloads and local calibrations.
The default image resolutions for each instrument are:

- COR2 images: 2048 × 2048 pixels
- C2 and C3 images: 1024 × 1024 pixels

The GCS model mesh is superimposed onto the coronagraph images, or, in the case of using a running difference images via '`-rd`', onto the difference between two temporally

[20]Documentation: https://api.helioviewer.org/docs/v2/ (last accessed February 2025)

adjacent coronagraph images. This results in a 3D mesh composed of circles surrounding the central axis, or skeleton, of the flux rope. The six governing parameters of the GCS model (see Section 3.4.1) can be adjusted interactively using the slider controls shown in Figure 28.
As a consequence of the image cadences between the instruments (see Section 4.5.1 and Section 4.5.2) being different, timestamps for C2/C3 and COR2 images do not always align perfectly. Upon completing the fitting process, the resulting GCS parameter values are stored in JavaScript Object Notation (JSON) format, which is widely supported in modern programming languages for ease of data handling.
A notable limitation of the tool is the occasional inaccessibility of certain images, even when correctly specified in the command line execution, for unknown reasons. Thus, the model cannot be applied in those cases, leading to gaps in the available dataset. This issue is not uncommon and restricts the user from utilising all of the coronagraphs' temporal coverage for many events. While applying the software for this work, around 20% of the images were missing for long time frames.
Currently, other tools for applying the GCS model implemented in Python 3 are being developed. One recently released example, which makes use of the original implementation by Freiherr von Forstner et al. (2021), is called *PyThea* (Kouloumvakos, 2025).

7.1.2 Modelling Process and Challenges

The goal of the modelling process is to achieve high-accuracy 3D reconstructions of the events by leveraging the stereoscopic capabilities of the STA, STB, and SOHO spacecraft constellation. The GCS model is applied to images captured simultaneously from the three vantage points at a given time and repeatedly across multiple observation times. This approach allows for the analysis of temporal evolution and the estimation of the CME's velocity (see Section 7.2).

Setup

Prior to fitting the model, the coronagraph images were viewed and examined in movie format. These movies are available as referenced in Section 6.3. Compared to static images, they provide a more comprehensive understanding of the CME's size, orientation, and morphological evolution. Additionally, they aid in determining whether to utilise the images captured by C2 or C3 for any given event alongside those captured by COR2, depending on the extent and evolution of the CME.
Then, the coronagraph images of interest from STA, STB, and SOHO are loaded into the GUI application of the 'GCS in Python' tool. For most events, running-difference images are used to enhance the visibility of CME features, as rapid variations are

accentuated by the technique, while simultaneously suppressing signatures of slower-evolving structures such as coronal streamers. These can overlap with the CME in the FOV of one or more coronagraphs, making differentiation helpful.

Fitting Procedure

Now, the fitting process begins. The GCS model is adjusted simultaneously for all three viewpoints using the GUI's slider controls to match the observed signature. The model is governed by six free parameters described in Section 3.4.1. To optimise the fit, the following sequence recommended by Thernisien et al. (2009) for adjusting the parameters is emulated:

1. Set $\alpha = 0$ initially.
2. Adjust ϕ, θ, and h_{apex} to match the observed orientation and height of the CME.
3. Modify κ to characterise the lateral expansion.
4. Fine-tune α and γ, then refine other parameters as needed.

Key Challenges and Model Constraints

Reconstructing CMEs presents several significant challenges, some inherent to the nature of the task and others arising from the design of the process described here. One common issue is that many CMEs show slightly varying morphologies across the time frame they are observed. In cases where the fit obtained for an earlier stage of evolution does not adequately represent later observations of the event, adjustments are necessary. To ensure a consistent representation across all observed time frames, a compromise is achieved by slightly modifying the fit.

Two examples of GCS model fits are presented for events IDs 31 and 34 in Figure 29 and Figure 30, respectively, along with a description of each event and the applied model. These examples exhibit significantly different morphologies, resulting in varying levels of reconstruction difficulty. In the following, common challenges encountered in event reconstruction and how they are addressed in the modelling process, particularly for cases with characteristics similar to those analysed in this study. Any uncertainties that arise and to what extent are discussed in Section 8.2.

All analysed events exhibit either a Halo or partial-Halo signature when observed from SOHO's perspective, which introduces additional intricacies (see Section 3.3). One of them is that the events signature tends to appear dimmer in the FOV of SOHO, making accurately reconstructing it more challenging.

Furthermore, the GCS model was specifically designed to investigate the idea of a flux rope-like morphology to fit CMEs (see Section 3.4.1). Consequently, applying this

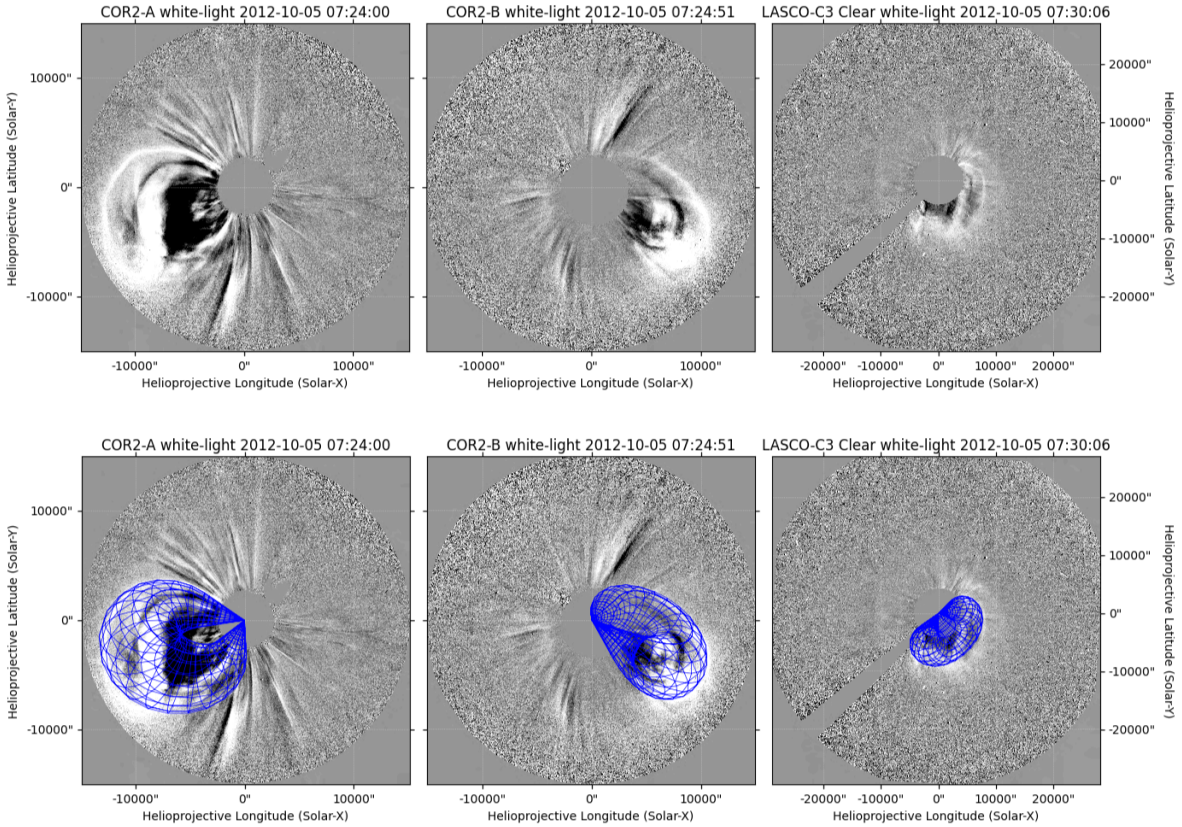

Figure 29: Application of the GCS model to event ID 31, observed simultaneously by (left to right) COR2A, COR2B, and C3 at around 07:24 UT on October 5, 2012. The medium-fast CME shows a distinct flux-rope structure visible from all perspectives. A surrounding shock signature is also discernible, particularly within the FOV of C3, where the CME appears as a partial Halo. The model fits the CME's leading edge, while excluding the shock front, and accurately captures its 3D spatial extension. The presented images are running-difference images created with the 'GCS in Python' tool.

model to events with other morphologies leads to increased ambiguity and uncertainty. The event ID 34 expands in a more spherical manner rather than exhibiting a flux rope-like configuration (see Figure 30), complicating its interpretation within the GCS framework.

Another frequent challenge lies in distinguishing the CME's leading edge from brightness enhancements associated with the shock wave. This issue is particularly common for fast CMEs, where shocks are more common and its front appears as a secondary bright structure near the leading edge (see Section 3.3). The overlap of these features makes it difficult to accurately determine the CME's boundaries, further complicating the reconstruction process. In Figure 29 a shock waves is visible in the FOV of C3, but the model successfully aligns with the CME's boundaries rather than the shock's front.

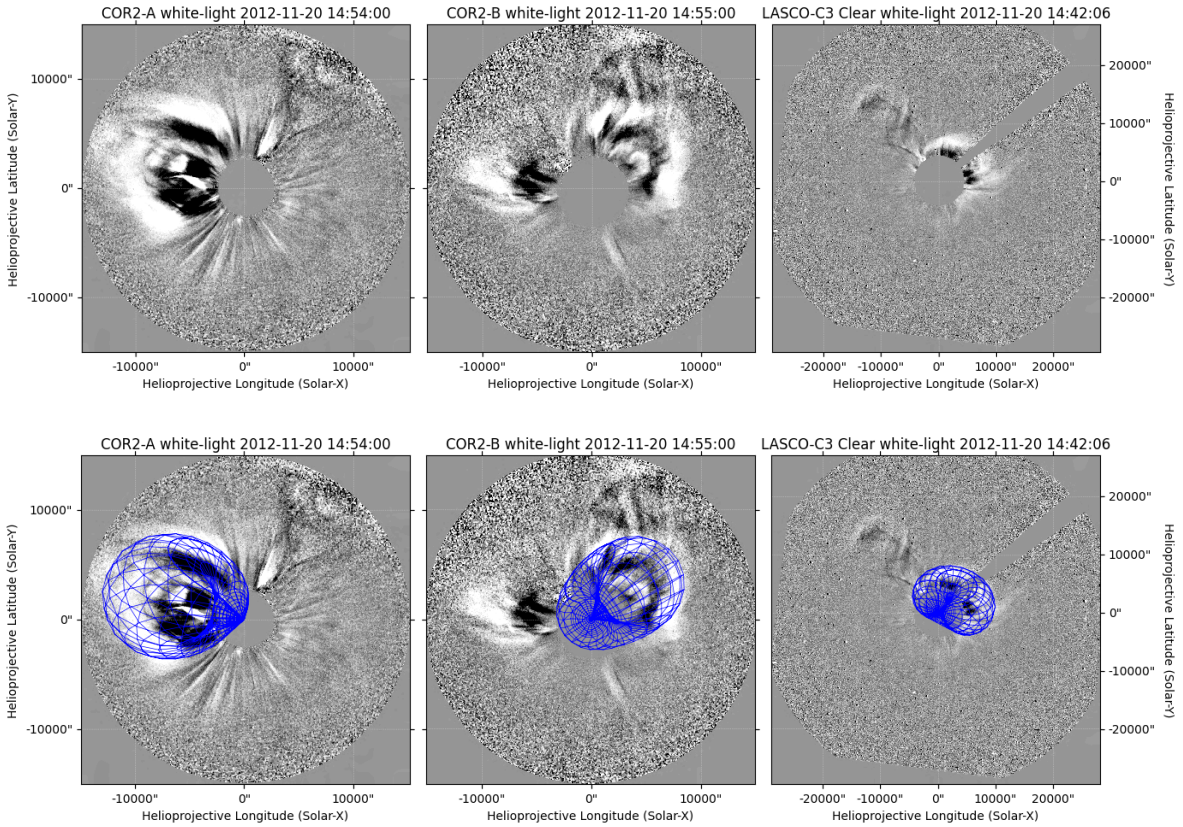

Figure 30: Application of the GCS model to event ID 34 observed simultaneously by (left to right) COR2A, COR2B, and C3 at around 09:39 UT on November 20, 2012. This medium-fast CME displays a non-flux-rope-like, more spherical morphology. It appears as a partial Halo in COR2B and C3. The model successfully captures the overall 3D spatial extension of the CME, but does not align with its signature everywhere. The presented images are running-difference images created with the 'GCS in Python' tool.

7.2 Estimating the Apex-Directed CME Velocity from Height-Time Profiles

Accurate modelling of CMEs propagation requires a precise estimation of their initial velocity. One such estimate is the apex-directed CME velocity, v_{apex}, which is not directly used in the forecasting approaches employed in this work, but as an intermediate result.

To investigate the evolution of h_{apex}, a height-time plot is constructed, where the GCS-derived apex heights are plotted against their corresponding observation times. An example of such a plot is presented in Figure 31. Here, v_{apex} is determined by fitting the GCS model to a sequence of coronagraph observations while assuming a steady rate of expansion beyond a certain CME height (or radial distance from the Sun). This sequence includes all images available in the 'GCS in Python' tool where the CME signature is clearly visible in at least one of three perspectives.

Building on the information in Section 3.4.2, the velocity would ideally be estimated only

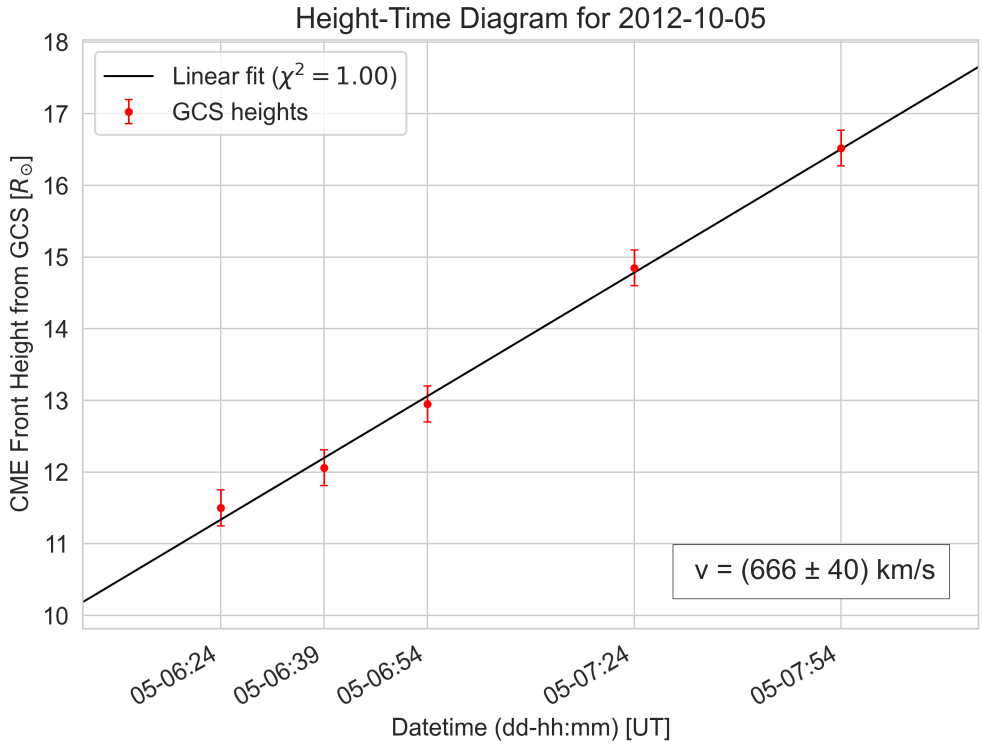

Figure 31: The apex heights of the event observed on October 5, 2012, as modelled via the GCS technique, are plotted as a function of the observation times from coronagraph data. An uncertainty of $\pm 0.25\,\mathrm{R}_\odot$ is assumed for the height measurements. A least-squares fit of a linear function, $f(t) = v \cdot t + b$, is performed, where the slope v represents the apex-directed CME velocity.

at larger distances, where the CME apex height exceeds 15–20 $\mathrm{R}_\odot$. At these distances, the influence of the Lorentz force is expected to have diminished significantly, providing a more stable velocity estimate. However, due to limitations in data availability within the 'GCS in Python' tool (see Section 7.1.1), a minimum height within this range cannot always be ensured. To balance data sufficiency with optimal velocity estimation, a lower limit of $11\,\mathrm{R}_\odot$ is adopted. This threshold represents a necessary compromise, ensuring that enough data points are available for a reliable velocity estimation while minimising the impact of early-stage forces on the measurement.

As discussed in Section 3.4.1, flux rope-like CMEs generally expand self-similarly beyond approximately $12\,\mathrm{R}_\odot$. This implies that five of the six parameters describing the GCS model, namely α, κ, and the three parameters describing its position and orientation, should remain close to constant. Consequently, for subsequent GCS modelling at later observational times, only the apex height, h_{apex}, needs to be treated as a free parameter. In this work, this assumption is extended to heights beyond $11\,\mathrm{R}_\odot$, as previously justified.

A linear function of the form

$$f(t) = v \cdot t + b$$

is fitted to these data points using the least-squares method. This fitting procedure is implemented in Python 3 using the *SciPy* library[21] via the function `optimize.curve_fit`. In this context, the slope v represents the apex-directed velocity, v_{apex}, while the intercept b accounts for any initial acceleration phase prior to the first observation.
A result obtained with this approach is illustrated in Figure 31. For the event ID 31, observed on October 5, 2012, the apex-directed velocity measures $v_{\text{apex}} \approx 670\,\text{km}\,\text{s}^{-1}$ after rounding. For a more in-depth discussion on the assumed errors and the evaluation of the quality of the applied linear fits, see Section 8.3. In this case, the corresponding linear fit yields a χ^2 value of approximately 1.00, indicating that the assumed uncertainty for the height measurements is well-aligned with the linear model used for fitting.

7.3 Computing the Earthward-Directed CME Velocity

A number of propagation modelling approaches in the literature directly employ the apex-directed velocity as derived in the previous chapter (e.g. Shi et al. (2015)). However, to maintain consistency with the assumption of self-similar expansion (see Section 3.4.1) and to improve the accuracy of the estimated initial CME velocity, an additional step is introduced: the computation of the Earthward-directed velocity, h_{Earth}.
This approach leverages the constraint imposed by self-similar expansion. Since this assumption dictates that the size of any given feature of a CME scales proportionally with its distance from the Sun, it follows that the expansion speed of different regions remains proportional as well. Consequently, the ratio of the CME height in the Earth's direction to its apex height directly determines the corresponding velocity ratio in these directions. Applying this principle, the velocity in the Earth's direction can be expressed as

$$v_{\text{Earth}} = \frac{h_{\text{Earth}}}{h_{\text{apex}}}\, v_{\text{apex}} \ . \tag{17}$$

At the time of this analysis, no readily available and well-implemented method was found in the literature for accurately determining the Earthward-directed CME height, h_{Earth}, without requiring additional manual effort or modifications. A previous approach used an exact 3D GCS model fitted to the CME, but the height was estimated visually with a slider, introducing uncertainties. The software was implemented in an IDL program developed by former members of Dr. V. Bothmer's research group, called the

[21] SciPy Documentation: https://docs.scipy.org/doc/scipy/index.html (last accessed February 2025)

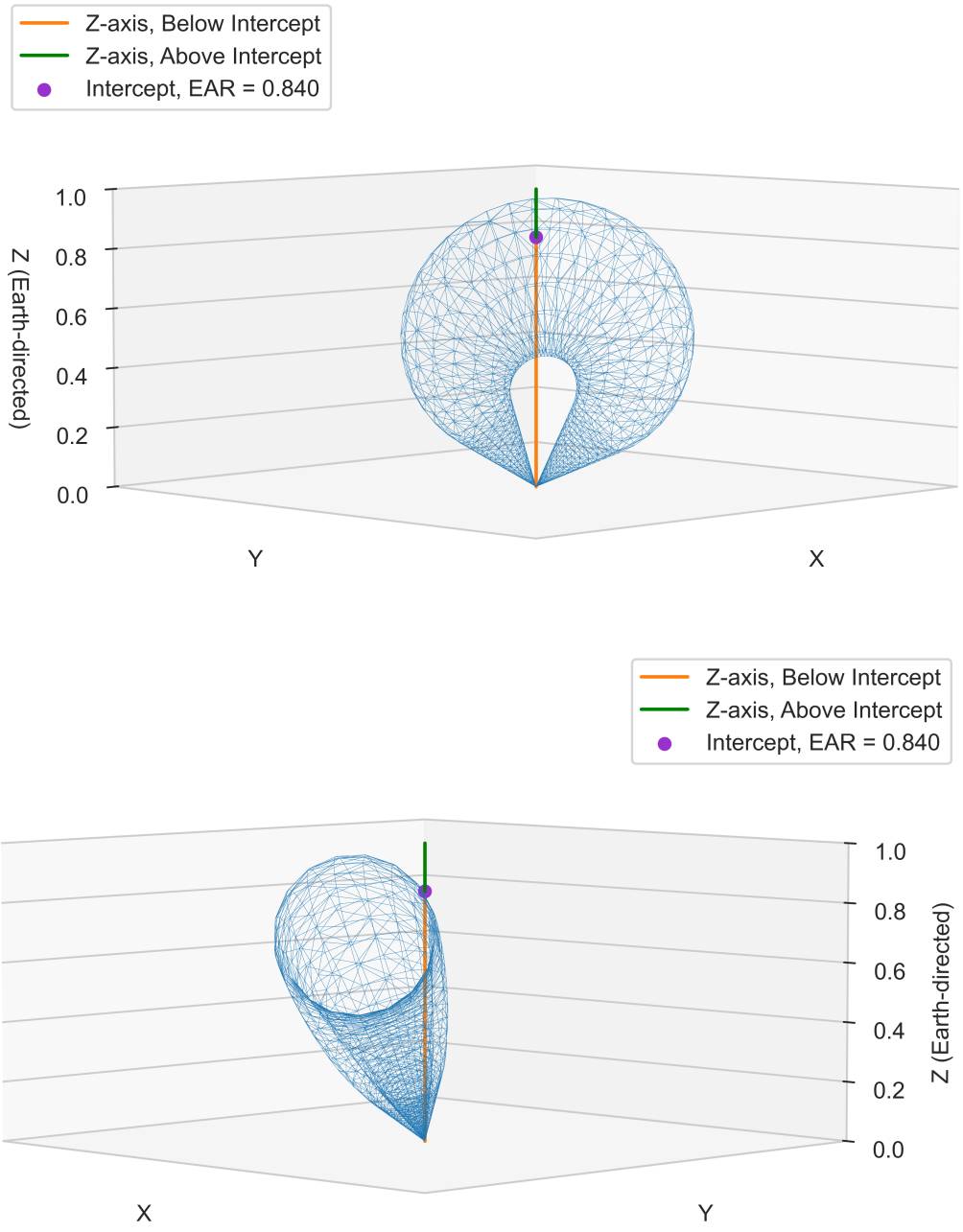

Figure 32: Numerical determination of the Earthward-directed CME velocity for the event observed on October 5, 2012, shown from two perspectives. The GCS model, derived through fitting, is visualised in 3D, with the Z-axis oriented toward Earth. The intersection of the model's outer shell with the Z-axis is marked, representing the normalised Earthward-directed CME height h_{Earth}. The total model height is normalised to 1, and the Z-axis is colour-coded to depict the relative proportions of its segments below and above the intersection. This serves as a visual representation of the EAR value, corresponding to the height ratio $h_{\mathrm{Earth}}/h_{\mathrm{apex}}$, measured here as approximately 0.840.

DoomsDay Calculator (DDC).

A new approach is developed and implemented in Python 3 to numerically determine h_{Earth} utilising the implementation of the GCS model by Forstner (2024). The complete code is provided in Section A.4, and its functionality is described as follows.

A high-resolution mesh representing the GCS model is generated within a 3D coordinate system, taking into account its spatial position and orientation. This process is performed using the method `gcs_mesh_rotated` from Forstner (2024). The model is inherently defined such that the Z-axis of this coordinate system is directed toward Earth. The apex height used for the mesh is normalised to unity, ensuring that any measured Earthward-directed CME height directly represents the height ratio from Equation 17. The Earthward-directed height h_{Earth} corresponds to the Z-coordinate of the intersection point between the outer shell of the GCS model and the Z-axis. This intersection is numerically approximated by identifying points on the generated rotated mesh that are closest to the Z-axis. To achieve this, a filtering condition is applied, selecting points that satisfy $|X|, |Y| \leq 0.01$. From these selected points forming a narrow column around the Z-axis, the maximum Z-value contained therein is extracted. This value represents the normalised Earthward-directed CME height and the corresponding height ratio, hereafter referred to as the Earthward-directed height to apex-directed height ratio (EAR).

The accuracy of this method, along with other sources of uncertainty at play are discussed in detail in Section 8.3. Figure 32 illustrates the numerical computation of the EAR value for the October 5, 2012 event ID 31. The colour-coded Z-axis, with a normalised height of 1, visually represents the $h_{\text{Earth}}/h_{\text{apex}}$ ratio.

Finally, the EAR serves as a scaling factor to derive the Earthward-directed CME velocity using Equation 17, incorporating the measured apex-directed velocity from the previous chapter. For the event ID 31, with $v_{\text{apex}} \approx 670\,\text{km}\,\text{s}^{-1}$ (see Figure 31) and EAR ≈ 0.84 (see Figure 32), the resulting velocity is $v_{\text{Earth}} \approx 560\,\text{km}\,\text{s}^{-1}$. This value serves as the initial velocity for propagation of the ICME from a defined starting distance.

7.4 Earthward ICME Propagation Modelling

Accurate modelling of ICME propagation depends not only on robust theoretical frameworks but also on precisely measured input parameters that capture both CME properties and their interaction with the surrounding solar wind. This work employs the DBM (see Section 3.4.2) and the MoDBM (see Section 3.4.3) to analyse ICME kinematics, incorporating both CME-specific parameters and those describing its evolution within the ambient solar wind. In particular, implementing the MoDBM requires significant programming effort, as its equation of motion must be solved numerically. The following

sections detail the determination of input parameters for these models and their implementation in Python 3.

7.4.1 Input Parameters of the Propagation Models

This section describes how the input parameters for both the DBM and the MoDBM are measured and derived in detail. The parameters are divided into those common to both models and model-specific parameters. It should be noted that the corresponding uncertainties of the input parameters used in both models are not explicitly mentioned, as incorporating them would require a significantly increased computational and analytical effort. Given that the MoDBM is integrated numerically, a comprehensive uncertainty quantification would considerably extend the scope of this study beyond its intended focus. Nevertheless, a discussion of the potential impact of these uncertainties is presented in Section 8.3.

Parameters Shared by Both the DBM and MoDBM

The parameters common to both models are employed either directly or indirectly in the analytical solution of the DBM (see Equation 7) and in the system of ODEs used in the MoDBM (see Equation 15 and Equation 16). The initial conditions are defined by the initial radial distance r_0, which corresponds to the largest apex height h_{apex} obtained from all GCS reconstructions during the modelling process. In every event analysed, r_0 exceeds $15\,\mathrm{R}_\odot$. The Earthward-directed CME velocity, v_{Earth}, as described in the previous Section 7.3, is adopted as the initial velocity, denoted v_0 or $\frac{\mathrm{d}r}{\mathrm{d}t}$ in the equations mentioned above. The reference start time of propagation, at which the initial distance and velocity are defined, is the time in Universal Time (UT) at which r_0 was obtained from the GCS modelling.
Complementing the initial conditions, several physical and geometric constants describe the CME's dynamic coupling with the solar wind. In particular, the geometrical parameters as obtained from the GCS modelling technique, namely the half angle α and the aspect ratio and κ, characterise the spatial extension of the CME. In the case of the event of October 5, 2012 (ID 31), $\alpha \approx 41°$ and $\kappa \approx 0.37$ are derived (see Figure 29). The CME mass M is computed via the empirical correlation in Equation 11, utilising the apex-directed velocity v_{apex} as derived in Section 7.2. Entering the result from Figure 31, Equation 11 yields $M \approx 5.08 \times 10^{15}\,\mathrm{g}$ for this event. Lastly, a drag coefficient of $c_d = 1$ is assumed in both models, as explained in Section 3.4.2, which is valid since all starting heights lie above the specified threshold.

Parameters Specific to the DBM

Within the DBM, the geometrical parameters α and κ are incorporated in Equation 3

to derive the cross-sectional area A. Although A is not computed as an independent parameter because of its radial dependence, it is used internally in Equation 8 during the calculation of the drag parameter γ. In Equation 8, the mass M, the cross-section A, the drag coefficient c_d, and the ambient solar wind density profile $\rho_w(r)$ from Equation 9 are combined. For convenience, the resulting γ is subsequently replaced by Γ (see Equation 12). In the case of the event ID 31, $\Gamma \approx 0.31\,\mathrm{km}^{-1}$ is obtained.
For both models, information on the ambient solar wind speed w is required. In the DBM, an estimate of w is directly inserted into the analytical solution (see Equation 7). This value is derived from in-situ measurements of the bulk velocity near Earth, with data of the WIND spacecraft (see Section 4.4) retrieved from NASA's OMNIWeb Plus service[16]. To achieve the best possible estimate, w is approximated as the bulk velocity measured shortly before the signature of the ICME appears, approximately one to two hours prior. In cases where a shock signature is present, the speed measured immediately prior to the shock is used. A detailed description of these observational signatures is provided in Section 3.3, with Figure 7 illustrating the measurements corresponding to the October 5, 2012 event (ID 31). For this event, $w \approx 320\,\mathrm{km\,s}^{-1}$ is measured.

Parameters Specific to the MoDBM

The MoDBM requires an additional input parameter to account for solar activity, and characterises the type of the ambient solar wind environment instead of using w directly. One such parameter is the SSN at the time of the event. The SSN is incorporated into the proton density relation described by Equation 14, which reflects more recent scientific findings compared to the DBM (as discussed in Section 3.4.3). This value is provided in the form of the 13-month smoothed monthly total SSN, as published by the Royal Observatory of Belgium using SILSO data[22] spanning from 1749 to the present. In the MoDBM, the measured ambient solar wind speed w is employed to select between two different speed profiles: $w_{\mathrm{med}}^{\mathrm{slow}}$ for a slow solar wind environment and $w_{\mathrm{med}}^{\mathrm{fast}}$ for a fast solar wind environment. As detailed in Section 3.4.3, these profiles assume different values at a radial distance of 1 AU, with $w_0 = 363\,\mathrm{km\,s}^{-1}$ for the slow solar wind and $w_0 = 483\,\mathrm{km\,s}^{-1}$ for the fast solar wind environment (see Equation 13). The selection is made by comparing the measured w (as determined above for the DBM input) to these reference values, thereby establishing which ambient wind environment is present for the propagation of the ICME. Since $w \approx 320\,\mathrm{km\,s}^{-1}$ was measured for the event ID 31, the slow solar wind environment is best applicable in this case. In cases where the measured data indicate a transition between the two types, the profile corresponding to the environment type observed closest in time to the ICME or shock arrival is selected. This is particularly relevant in the case of event ID 36, where the measured w

[22]SSN data (new version): https://www.sidc.be/silso/newdataset (last accessed February 2025)

of $\approx 420\,\mathrm{km\,s^{-1}}$ is right between the ideal values of the two types. Since the data also shows a declining trend close to the shock signature, $w_{\mathrm{med}}^{\mathrm{slow}}$ is chosen (see Table 10).

7.4.2 Implementation of the Models

The propagation models are implemented in Python 3 using both analytical and numerical approaches to simulate the evolution of the ICME front height and velocity. Once the input parameters r_0, v_{Earth}, Γ, and w are established, the analytic solution of the equation of motion is calculated. In this process, a dedicated function computes $r(t)$, and its derivative is used to derive $v(t)$.

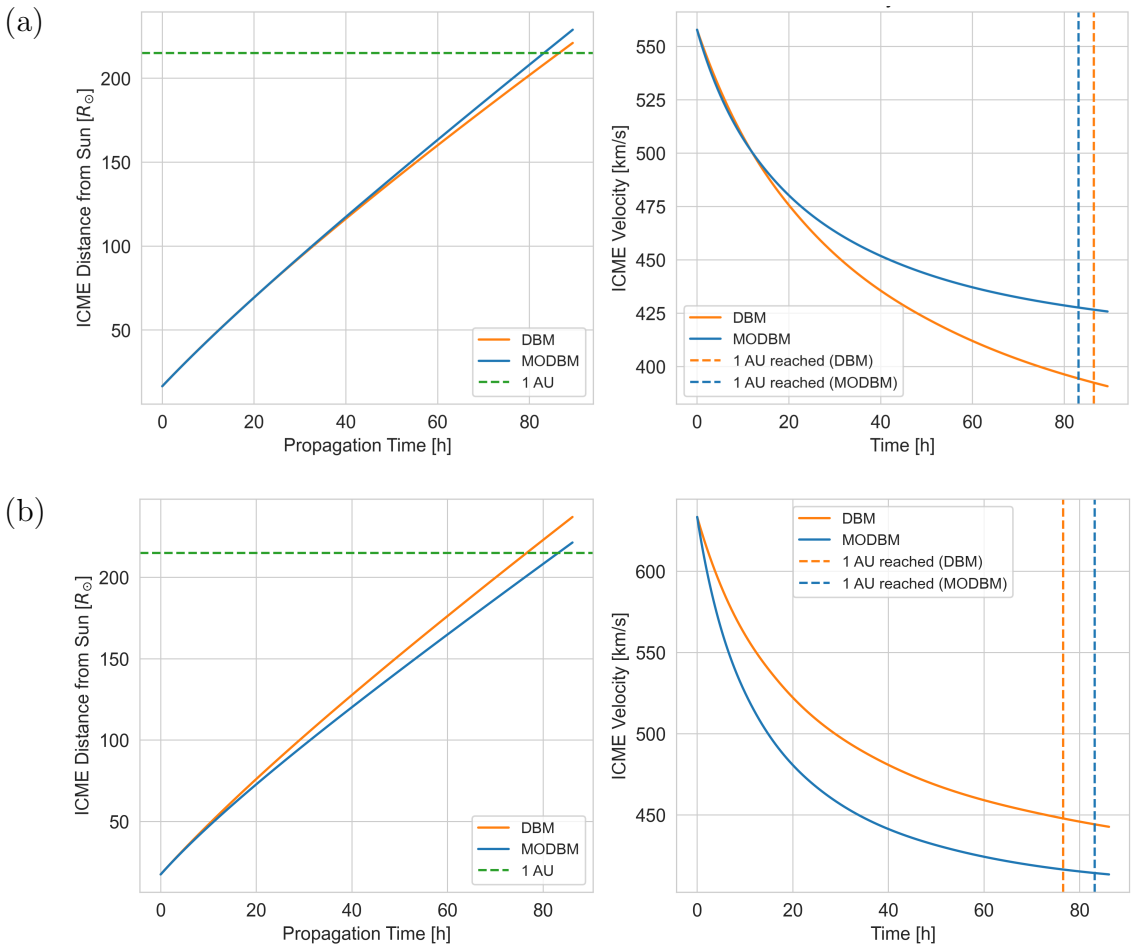

Figure 33: Modelled propagation of the 1D Earthward-directed CME front for two events, observed on (a) October 5, 2012, and (b) April 11, 2013, comparing results obtained using the DBM and MoDBM. The left panels display the radial distance of the CME front from the chosen starting height r_0 during propagation towards Earth, while the right panels illustrate the evolution of the ICME velocity over time. Dashed vertical lines mark the predicted arrival times at Earth's position (1 AU), revealing discrepancies between the models: for (a), the MoDBM predicts an earlier arrival by approximately three hours, whereas for (b), the DBM forecasts an earlier arrival by around 6.5 hours.

The MoDBM demands more effort due to the radial dependence of the drag parameter $\gamma(r)$ in the equation of motion (see Equation 6). Here, the homogeneous, linear second-order ODE is reformulated into a two-dimensional system of first-order differential equations (see Equation 15 and Equation 16). To solve this system, numerical integration with the initial conditions r_0 and v_{Earth} is performed using the `scipy.integrate.odeint` method from the *SciPy* library[21]. To maximise precision, time steps of size 1 second are chosen. The integration yields the functions $r(t)$ and $v(t)$ from r_0 to 1 AU, or time-resolved profiles of the 1D Earthward-directed ICME front height and velocity, from which the respective ICME arrival time at the distance of L_1 of the Sun-Earth system can be derived and then validated against in-situ WIND measurements.
Two results of these simulations are presented in Figure 33 for event IDs 31 and 37. They highlight how varying assumptions in the DBM and MoDBM influence the modelled propagation of ICMEs. For the event on October 5, 2012 in Figure 33(a), notable differences emerge between the models, leading to a predicted arrival time discrepancy of approximately three hours at Earth's orbit. In this case, the MoDBM predicts an earlier arrival compared to the DBM. Interestingly, the scenario is reversed for the event observed on April 11, 2013 in Figure 33(b), where the predicted arrival times differ by more than six hours. A detailed discussion of these results, including insights into how model assumptions and input parameters influence these discrepancies, can be found in Section 8.4.

8 Results and Discussion

This chapter presents the results of the 3D geometric CME modelling, as well as the ICME propagation modelling performed for the five selected events. Moreover, the ICME arrival times predicted by the developed approaches are evaluated against in-situ measurements. Model performance, limitations, and operational potential are discussed, focusing on accuracy, parameter sensitivity, and future improvements.

8.1 Dataset and Event Selection Process

The selection of events is a critical step in this study, as it directly influences the reliability and interpretability of the results. The dataset used in this work, summarised in Table 7, consists of events that enable 3D CME reconstruction from three simultaneous viewpoints, while also featuring distinct ICME signatures measured near Earth. By excluding events with overlapping structures or those likely to engage in interactions with other solar phenomena, the dataset minimises complexities that could otherwise obscure the analysis, providing a clear foundation for evaluating the performance of the models.

Methodological Approach

As introduced in Chapter 5 and Chapter 6, the selection criteria are carefully motivated to build a robust foundation for this analysis. The criteria adopted here, specifically Criterion 2 and Criterion 3, reduced the initial pool of 45 events provided in the list compiled by Kay and Gopalswamy (2017) considerably. Furthermore, due to the high effort associated with the analysis, only five events were selected. Although this small sample size limits the statistical significance of the findings, it enables a highly detailed and controlled evaluation of each event.

Mitigating Event Complexity and Observer Bias

Despite the manual nature of the event selection, potential observer bias is considered negligible because the limited number of events allowed for an in-depth analysis of each case. A controlled environment, in which the performance limits of the GCS+DBM and GCS+MoDBM approaches can be effectively estimated, is successfully created. In this context, the resulting arrival-time errors represent a best-case scenario for isolated events, providing a valuable baseline for disentangling inherent model limitations from other complexity-induced errors.

Dumbović et al. (2018) find a potential "preconditioning effect" being at play in their analyses, meaning a preceding CME "clears the path", significantly lowering γ. In extreme cases, they described a drop to a 10 times lower value than their average values.

However, the strictness of the criteria used here ensures that such effects are not a concern in this work. Interestingly, the discrepancies between results obtained using the dataset defined in this work, compared to those obtained with datasets not specifically biased towards isolated event signatures, could provide valuable insights on the impact of more complex processes, such as CME-CME or ICME-ICME interactions. Nonetheless, it is important to recognise that the criteria defined here cannot guarantee that all events are completely free of interactions with other phenomena, since identifying such interactions by eye remains inherently challenging and unreliable.

Dataset Diversity and Limitations

Examining the dataset reveals a broad range in key parameters. As mentioned in Section 6.3, the dataset includes divers separation angles of the STEREO probes. Moreover, Kay and Gopalswamy (2017) report that the angular widths of these five events range from around 25° to 55°, and their approximate velocities near the Sun span from 460 to 1250 $\mathrm{km\,s^{-1}}$, suggesting a good diversity of CME morphologies when considering the small size of the data set.

The results of the 3D reconstruction and velocity determination performed in this work suggest very similar ranges (see Table 8 and Table 9). However, only one event in the set exceeds 1000 $\mathrm{km\,s^{-1}}$, which limits the ability to draw conclusions about high-speed CMEs and their corresponding interplanetary counterparts. Although events of this type are uncommon, making up less than 5 % of all entries in the *SOHO LASCO CME Catalog* (Gopalswamy et al., 2025), a singular event is likely subject to a specific bias which would heavily influence conclusions drawn about the group as a whole.

Furthermore, the dataset does not include, and therefore under-represents, narrow-type CMEs (Chen, 2011; Yashiro et al., 2004). Notably, event IDs 34 and 36 show no clear flux rope-like signatures in any coronagraph view. Since for most non-narrow CMEs flux rope-like structures are typically observed (Chen, 2011), they are over-represented in this sample.

Next, the selected events occur only during the declining phase of a solar cycle (2011–2013), but this temporal distribution is considered less influential on the CME properties than the implications of the small sample size and the strict selection criteria applied in this work. Expanding the dataset in future studies would help mitigate these biases and provide a more comprehensive understanding of model limitations.

In summary, the event selection process yields a small yet high-quality dataset that minimises confounding factors and provides a robust foundation for evaluating the modelling approaches. The findings from this analysis will feed into subsequent discussions on CME modelling and ICME arrival-time predictions, offering insights into the models' performance under controlled conditions and highlighting areas for future refinement.

8.2 3D Geometric CME Modelling with the GCS Model

The GCS model was employed for 3D reconstruction of CMEs from the three viewpoints of STA, STB and SOHO simultaneously to accurately capture their spatial characteristics, describe their evolution, and serve as a basis for subsequent propagation modelling. In this work, five CMEs were successfully reconstructed using the 'GCS in Python' tool, and the derived parameters for a single reconstruction of each event, together with the corresponding time stamp at which the model was fitted, are listed in Table 8. In addition to that, Table A1 shows all times at which each event was reconstructed and which CME apex heights were obtained. For event IDs 31 and 34, the listed parameters match those of the models illustrated in Figure 29 and Figure 30, respectively. The rest of the obtained GCS model fits are presented in Section A.2.

Table 8: Results of the geometric CME reconstruction using the GCS model. The table lists the derived parameters ϕ (Stonyhurst longitude), θ (latitude), γ (tilt angle), h_{apex} (apex height), κ (aspect ratio), and α (half angle) characterising the model. In addition, the table provides the approximate observation time stamps in UT for the COR2 and C2/C3 data used during the reconstruction. For each event, only one example reconstruction is listed; see Table A1 for the full h_{apex} evolution.

ID	Time Stamp (UT) y/m/d:hm	ϕ [deg]	θ [deg]	γ [deg]	α [deg]	κ -	h_{apex} $R_\odot$
15	2011/09/14:0324	16	21	0	17	0.49	13.99
31	2012/10/05:0724	10	-16	42	41	0.37	14.85
34	2012/11/20:1454	26	19	-29	33	0.64	13.62
36	2013/03/15:0824	348	-9	-72	39	0.42	14.96
37	2013/04/11:1024	349	-2	38	51	0.42	15.69

Python 3 Implementation

The implementation of the GCS model utilised in this work has been validated as error-free by Freiherr von Forstner (2020), who compared the GCS model meshes generated by the Python implementation to the CME signatures in coronagraph images, and the meshes generated from the original IDL implementation. This modern approach enhances older IDL-based workflows by enabling faster processing and reducing manual intervention, despite occasional missing images (see Section 7.1.1). While the GUI allows parameter specification to the hundredth decimal place, values in the table are rounded, as incremental differences are generally indistinguishable—except for h_{apex} and κ, where higher precision remains meaningful.

The unavailability of certain images, even when they are correctly specified via the command line and are present in the instrument data archives, restricts the application

of the model to those timestamps. Consequently, gaps may occur in the data used for determining quantities such as v_{apex}. In addition, the slight differences in image cadences between instruments (see Section 4.5.1 and Section 4.5.2) mean that the timestamps for C2/C3 and COR2 images do not always align perfectly. This misalignment complicates the application of the model when the time intervals between images increase in length. For fast to very fast CMEs, particular care was taken since the model may align precisely with images at the desired timestamp while deviating slightly for others. However, these challenges are manageable with increased experience in using the tool and are not considered major sources of error within this analysis.

Uncertainties Inherent to GCS Modelling

The potentially largest uncertainty arises from the need to interpret the CME's structure and morphology subjectively. This uncertainty is considerably lower when aligning the model across three viewpoints rather than two or one, as projection effects introduce ambiguities that cannot be resolved from a single perspective. As noted by Thernisien et al. (2009), the determination of GCS parameters inherently depends on the modeller's expertise. It should also be noted that it is impossible to derive the "true" parameter values from real observational data (Verbeke et al., 2022).

In an effort to assess approximate error ranges, Verbeke et al. (2022) reconstructed synthetic data—generated with the GCS software—from different viewing configurations, utilising both single and multiple viewpoints. They derived, "as a starting point for quantifying the minimum error," the following error ranges: $\Delta\phi = 11^{\circ}{}^{+18^{\circ}}_{-6^{\circ}}$, $\Delta\theta = 6^{\circ}{}^{+2^{\circ}}_{-3^{\circ}}$, $\Delta\gamma = 25^{\circ}{}^{+8^{\circ}}_{-7^{\circ}}$, $\Delta\alpha = 10^{\circ}{}^{+12^{\circ}}_{-6^{\circ}}$, $\Delta h = 0.6^{+1.2}_{-0.4}$ $R_{\odot}$, and $\Delta\kappa = 0.1^{+0.03}_{-0.02}$. These uncertainties are expected to be reduced in the case of three viewpoints being available. Consequently, in Table 8, the parameter values are preserved in their original form rather than being rounded to directly mirror these error margins, and the margins themselves are not adopted here. Quantifying subjective uncertainties in a manner more appropriate for the reconstructions performed here would considerably expand the scope of this work.

Event-Specific Modelling Challenges

Beyond these general considerations, also event-specific challenges are encountered when applying the GCS model, reflecting the unique characteristics of each CME.

For instance, in event ID 15, the CME shows a clearly discernible flux rope-like structure and no overlapping solar phenomena are observed. The signatures are strong and well-defined in STA, STB, and C2, although the partial Halo signature in C3 is poorly visible at later times. The applied model fits the CME's structure very well.

In event ID 31, the flux rope-like structure is evident with good visibility across all viewpoints. However, a prominent shock front, especially apparent in C3, necessitates

careful exclusion from the fit. The presence of a subsequent small CME, erupting in a distinctly different direction and thus, being very likely to not interact with the event in any way, is easily distinguished in STA and STB, though some caution is required in C2 and C3.

Conversely, event ID 34 presents a non-flux rope-like, more spherical signature. In multiple perspective, coronal streamers overlap with the CME's signature. The use of running difference images greatly aids in distinguishing these features; the GCS model successfully captures the overall 3D spatial extension of the CME, even if it does not align perfectly with its signature throughout.

In event ID 36, the CME exhibits a non-flux rope-like, more spherical and diffuse structure with extensive full-Halo appearances in the perspectives of STA and SOHO. The large, bright shock fronts and overlapping coronal streamers complicate the effort to reach consensus across all viewpoints, although running-difference images prove effective in distinguishing the CME signature.

In contrast, event ID 37 displays a flux rope-like structure, particularly evident in STB's view, yet the overall appearance remains rather diffuse. Here too, the prominent shock front and overlapping coronal streamers pose challenges for a consistent multi-viewpoint fit. In both cases (36 and 37), the fitted models capture the overall 3D spatial extension of the CME despite the inherent difficulties in clearly distinguishing the shock fronts from the CME signatures.

Lastly, the expansion of all CMEs is not perfectly self-similar. As a result, model parameters required iterative adjustments across a sequence of images to achieve an optimal balance in accurately capturing their evolution. Although this was not identified as a significant source of uncertainty in the cases analysed here, it remains an important factor to acknowledge.

Systematic Parameter Discrepancies with Prior Work

A brief comparison of the derived values for parameters α and κ with those reported in Kay and Gopalswamy (2017) reveals notable systematic differences. For event ID 15, the here derived half-angle $\alpha = 17°$ is considerably lower than the reported 25°, while the aspect ratio $\kappa = 0.49$ is substantially higher than their value of 0.15. Similarly, in event ID 31, $\alpha = 41°$ is lower than the reported 52°, and $\kappa = 0.37$ exceeds the corresponding value of 0.19 from Kay and Gopalswamy (2017). In event ID 34, the half-angle values are in closer agreement (33° versus 34°), yet the value of $\kappa = 0.64$ obtained here remains markedly higher than 0.25. For events ID 36 and ID 37, the trends persist, with α values (39° and 51°, respectively) differing from the published values of 65° and 44°, and the κ values from this current work again consistently higher. These discrepancies likely stem from differences in the reconstruction methodologies and the subjective interpretation

of the CME's morphology. Although the overall morphology is captured similarly in both studies, the sensitivity of the derived parameters, especially κ, underscores the importance of considering their uncertainties when comparing results across different approaches.

Implications for Propagation Modelling

The multi-viewpoint GCS reconstructions provide essential inputs for propagation models such as the DBM and MoDBM. Although uncertainties in the derived parameters propagate into other model inputs, such as velocity estimates, and, ultimately, ICME arrival time predictions, the integration of three viewpoints significantly reduces the risk of misinterpreting event characteristics. This approach also minimises projection effects, which are particularly critical for Halo or disk events (see Section 3.3), and enhances the overall accuracy of the reconstructions.
The Python-based workflow streamlines the reconstruction process, enabling efficient handling of multi-spacecraft data. By combining observations from STA, STB, and SOHO, this methodology not only yields accurate reconstructions but also establishes a framework for integrating data from future missions like Vigil (see Section 4.1). The inclusion of L_5 observations will further improve CME detection and forecasting for Earthward-directed events, addressing biases such as overestimated widths and underestimated speeds that are common in traditional approaches (Burkepile et al., 2004).

8.3 ICME Propagation Model Input Parameters

This section presents the results of the input parameter determination for the DBM and MoDBM, which are essential for simulating the propagation of ICMEs toward Earth. The parameters are divided into those shared by both models, listed in Table 9, and those specific to each model, listed in Table 10. Both tables collectively provide the necessary inputs for both models. For more information on this categorisation or details on the parameters themselves, refer to Chapter 7.
The determination of input parameters for the DBM and MoDBM involves inherent uncertainties originating from observational limitations and modelling assumptions. Certain parameters, such as the apex-directed CME velocity v_{apex}, explicitly incorporate uncertainty estimates derived from coronagraph observations and linear fits to height-time profiles. These uncertainties are quantified and integrated into the analyses presented in subsequent chapters.
However, for most other parameters—such as the Earthward-directed velocity v_{Earth}, mass M and drag coefficient Γ—it is highly impractical to give specific estimates of accompanying uncertainties. This is due to (1) the involvement of numerous interde-

Table 9: Results for the input parameters shared by the DBM and MoDBM, including propagation start time (UT), start CME front height r_0, apex-directed velocity v_{apex}, Earthward-directed height to apex-directed height ratio (EAR), initial Earthward-directed CME velocity v_{Earth} (at starting height r_0), and mass M.

ID	Start Time (UT) y/m/d:hm	r_0 $R_\odot$	v_{apex} km s^{-1}	EAR -	v_{Earth} km s^{-1}	M 10^{15} g
15	2011/09/14:0354	15.52 ± 0.25	610 ± 50	0.83	500	4.84
31	2012/10/05:0754	16.52 ± 0.25	670 ± 40	0.84	560	5.08
34	2012/11/20:1539	16.52 ± 0.25	730 ± 50	0.79	570	5.32
36	2013/03/15:0854	18.08 ± 0.25	1210 ± 140	0.92	1120	7.74
37	2013/04/11:1054	17.45 ± 0.25	650 ± 50	0.98	630	5.0

pendent and difficult-to-quantify factors, and/or (2) the extensive computational and analytical resources required for propagating these errors, especially in the case of the MoDBM, where numerical integration is performed. Propagating uncertainties for these parameters would significantly broaden the scope of this study beyond its intended limits.

Table 10: Model-specific parameters for the DBM and MoDBM. DBM inputs: drag parameter Γ (see Equation 12) and ambient solar wind speed w. MoDBM inputs: ambient solar wind environment type (per Equation 13) and 13-month smoothed international sunspot number (SSN).

	DBM		MoDBM	
ID	w km s^{-1}	Γ km^{-1}	w-Type -	SSN -
15	370 ± 10	0.13	w^{slow}	86.6
31	320 ± 10	0.31	w^{slow}	85.8
34	315 ± 10	0.32	w^{slow}	87.7
36	420 ± 10	0.20	w^{slow}	84.4
37	390 ± 10	0.48	w^{slow}	84.3

By focusing on parameter determination and model comparison explicitly, this work prioritises its core objectives. Nevertheless, the potential implications of these uncertainties are considered and discussed in the following sections.

8.3.1 Apex-Directed CME Velocity Estimates

The apex-directed velocity, v_{apex}, derived from linear fits to height-time profiles (see Section 7.2), serves as a critical input parameter for CME propagation models. To ensure reliable velocity estimates, the quality of the linear fits and systematic uncertainties must be thoroughly evaluated.

Chi-Squared Analysis of Linear Fits

The goodness-of-fit for each velocity determination is quantified using the chi-squared statistic via

$$\chi^2 = \sum_{i=1}^{N_t} \frac{(h_{\mathrm{apex},\,i} - f(t_i))^2}{\sigma^2_{h_{\mathrm{apex}}}} \tag{18}$$

where $\sigma_{h_{\mathrm{apex}}} = 0.25\,\mathrm{R}_\odot$ represents the assumed uncertainty in the GCS-derived apex heights. This value lies near the lower limit of literature-suggested errors (see previous section) but is justified by the observed stability in the GCS-derived values for $h_{\mathrm{apex}} \geq 11\,\mathrm{R}_\odot$ (see Section 3.4.1).

For the analysed events, χ^2 values range from 0.01 to 1.00 (see Section A.3). A value of $\chi^2 \approx 1$, as seen for event ID 31 (see Figure 31), confirms that the assumed height uncertainty aligns well with the residuals of the linear model. Values of $\chi^2 \ll 1$ (e.g., 0.01 for event ID 15 in Figure A4) indicate residuals smaller than $\sigma_{h_{\mathrm{apex}}}$, suggesting either overestimated height uncertainties or exceptionally stable CME propagation. The majority of events exhibit χ^2 close to 1, supporting the validity of the linear velocity assumption within the observed height range.

Occasional gaps in the height-time data, caused by missing coronagraph images or misaligned instrument cadences (see Section 7.1.1), naturally limit the theoretical precision of velocity determinations. However, the achieved χ^2 values suggest that the practical impact of gaps on velocity estimates is minimal.

Systematic Biases and Velocity Underestimation

While the χ^2 analysis validates the internal consistency of the fits, systematic biases in v_{apex} remain. Studies by Verbeke et al. (2022) and Vršnak et al. (2004) indicate that velocity estimates derived from heights below $13\,\mathrm{R}_\odot$ systematically underestimate true CME speeds by up to $-20\,\mathrm{km\,s^{-1}}$ due to residual acceleration. For faster CMEs ($v_{\mathrm{apex}} > 1000\,\mathrm{km\,s^{-1}}$), errors exceeding $100\,\mathrm{km\,s^{-1}}$ are expected.

In this work, the systematic bias is mitigated by ensuring at least two height measurements exceed $13\,\mathrm{R}_\odot$ for every event (see Table A1). Consequently, the underestimation is expected to remain below the $-20\,\mathrm{km\,s^{-1}}$ threshold reported by Verbeke et al. (2022). They suggest adopting a 3% or $50\,\mathrm{km\,s^{-1}}$ error margin, these values are not directly applied here due to complexities in comparing height thresholds across studies. Instead, the fitting-derived uncertainties (ranging $\sim 40 - 140\,\mathrm{km\,s^{-1}}$; Section A.3) are directly used, because the margins of error are assumed generous enough to inherently account for both statistical scatter and the smaller systematic bias.

Implications for Propagation Modelling

The GCS-derived apex heights, combined with linear fitting, yield robust v_{apex} estimates suitable for ICME propagation models. The agreement between χ^2 values and the assumed $\sigma_{h_{\text{apex}}}$ validates both the fitting methodology and the linear velocity assumption. Systematic biases, though possibly present, are minimised through the employment of a minimum height threshold. These results ensure that the input velocities capture the CME dynamics with high accuracy, forming a reliable foundation for subsequent propagation analyses.

8.3.2 Earthward-Directed CME Velocity Estimates

The Earthward-directed velocity, v_{Earth}, derived from the Earthward-Apex Ratio (EAR) and apex-directed velocity via Equation 17, is directly used in both ICME propagation models employed in this work. Given its pivotal role, understanding and quantifying the uncertainties associated with v_{Earth} is essential, particularly as these uncertainties directly influence model reliability and accuracy.

Key Uncertainty Sources

The total uncertainty in v_{Earth} is governed by:

- **GCS modelling errors / v_{apex} fitting errors**: Dominant factor, introducing $\sim 40-140\,\text{km}\,\text{s}^{-1}$ scatter in v_{apex} (see Section 8.3.1), as well as difficult-to-quantify and interdependent errors arising from the interplay of all parameters governing the GCS model, further discussed in Section 8.2, except for the models apex height.
- **Assumption of self-similar expansion**: Although self-similarity across their evolution is a characteristic of most CMEs (Low, 2001), deviations are not uncommon, especially during early phases of evolution (Mrotzek, 2019). Evaluating the self-similarity of the expansion of each event was however not part of the analysis conducted in this work, which is why this potential uncertainty is not further quantified or considered.
- **Numerical computation method**: Considered negligible, as justified below.

Robustness of the Numerical EAR Computation Method

The EAR is calculated by filtering points from the GCS mesh that closely align with the Earthward direction (Z-axis). This procedure, implemented using Python 3, is detailed further in Section 7.3. To optimise computational efficiency without sacrificing precision, the selected cross-sectional area of this Earthward-aligned column

around the Z-axis is deliberately restricted to less than 0.1 % of the total mesh area. Systematic uncertainties introduced by mesh resolution variations were examined by testing multiple mesh configurations. These tests showed that improvements in accuracy become insignificant when the mesh resolution exceeds approximately 1000 vertices per component. Since 1500 vertices per component are used here (see Section A.4), systematic uncertainty from mesh resolution is deemed negligible. Thus, in determining EAR and v_{earth} values, errors predominantly arise from uncertainties inherent to the GCS modelling technique and the subsequent calculation of the apex-directed velocity. Additionally, also the uncertainties linked to the assumption of self-similar expansion cannot be quantified meaningfully here, resulting in no specific errors for the EAR values being derived here.

Propagation of GCS Modelling and Apex Velocity Uncertainties

The Earthward velocity v_{Earth} inherits uncertainties from many interconnected sources, such as (1) the geometric parameters of the GCS model and (2) the apex-directed velocity v_{apex}. At first, it might seem like the EAR ($h_{\text{Earth}}/h_{\text{apex}}$) is governed by the GCS model's apex height and its error. However, it is only governed by the other GCS model's parameters and their uncertainties, namely the models geometric (the tilt angle γ, half-angle α, and aspect ratio κ) and positional parameters ϕ (longitude) and θ (latitude). These parameters collectively define the flux rope's orientation and shape, determining where the GCS shell intersects the Earthward-directed Z-axis (see Section 7.3). For instance, errors in γ yield a different rotation of the structure, thus shifting the intersection point and altering the measured EAR value. Moreover, deviations in α or κ may modify the models curvature near the Z-axis. Also, the interdependency of these parameters during fitting, where adjustments to ϕ or θ may compensate for errors in γ or κ, makes isolating their individual contributions to the uncertainty of the EAR values highly difficult.
The uncertainty arising from v_{apex} can however be quantified, derived from linear fits to height-time profiles (see Section 8.3.1). However, unquantified errors in ϕ, θ, and the geometric GCS parameters also indirectly influence v_{apex} by distorting the reconstructed height evolution. For example, a misaligned longitude ϕ could bias the perceived propagation direction, affecting both h_{apex} and v_{apex}. A comprehensive error propagation analysis would, for example, require probabilistic sampling of the entire GCS parameter space, which tremendously exceeds the scope of this work.

Implications for Propagation Modelling

The Earthward-directed velocity, v_{Earth}, resolves a critical limitation in propagation models that rely solely on velocities measurements from the CME apex. Apex velocities

inherently fail to capture the directional dependence of CME expansion, leading to systematic errors in arrival-time predictions. By contrast, v_{Earth} directly quantifies the Earth-impacting component of the CME's kinematics through the EAR, which links the CME's geometry to its propagation under the self-similar expansion assumption. This assumption, which holds for most CMEs (Low, 2001), ensures that v_{Earth} aligns physically with the CME's 3D structure. The numerical computation of EAR eliminates subjective visual estimations, replacing them with an automated, reproducible method that enhances both accuracy and operational readiness for missions like ESA's Vigil. The integration of v_{Earth} into forecasting workflows marks a pivotal advancement in space weather preparedness. Furthermore, the Python 3-based implementation (see Section A.4) ensures seamless compatibility with modern GCS tools and future multi-viewpoint and Vigil-like data streams. While deviations from self-similar expansion remain a potential uncertainty, the methodology's robustness for the events selected in this work establishes it as a foundational step toward real-time forecasting.

8.3.3 Further Shared and Model-Specific Input Parameters

CME Mass Estimates

The empirical correlation in Equation 11 offers a practical and efficient method for estimating CME mass directly from apex-directed velocities, the results of which are entered in Table 9. As highlighted by Pluta et al. (2018), this correlation is particularly well-suited for estimating the mass of intense CMEs observed in coronagraph images, making it an ideal choice for the events analysed in this work. However, this approach is not without its limitations. By relying solely on apex-directed velocity, the correlation neglects other classical indicators of mass, such as the spatial distribution of CME material. This simplification means the method may fail to capture event-specific variations, such as variations in electron density or non-self-similar expansion, which can lead to systematic biases in mass estimates.

A significant drawback of this method is its direct dependence on the apex-directed velocity, which can be problematic for CMEs exhibiting strong early-stage acceleration or deceleration (Vršnak et al., 2004). Such dynamic behaviour can distort the velocity-mass relationship, leading to inaccurate mass estimates. Moreover, mass and cross-sectional area A are tightly coupled through γ via Equation 8). During the analysis for this work, one event not included in the final dataset exhibited an unusual combination of characteristics: a relatively small spatial extension but an exceptionally high speed. This difference created a mismatch between the parameters A and M, as the high speed led to an overestimated mass via the empirical correlation. Such an overestimation could result in significant errors in arrival time predictions, as the derived mass would not align with the CME's actual spatial extent, thereby distorting the drag forces and

propagation dynamics in the model. This highlights a key limitation of relying solely on apex-directed velocity for mass estimation, particularly for events with atypical kinematic or geometric properties. Additionally, uncertainties in GCS parameters, such as the model height, propagate into the apex-directed velocity determination, further compounding errors in mass estimation. While these interdependencies introduce significant uncertainties, a detailed analysis of their propagation would extend beyond the scope of this work.

To address these limitations, more sophisticated approaches, such as those employed by Pluta et al. (2018), could be integrated. These methods decouple mass estimates from velocity proxies, reducing the influence of dynamic effects on mass determination. However, such approaches come at the cost of increased computational and operational complexity, sacrificing the primary advantage of the empirical correlation: its simplicity and efficiency. Particularly for events observed stereoscopically, where initial CME speed measurements are most reliable (Pluta et al., 2018), as those analysed in this work, the correlation remains a valuable tool for rapid and reasonably accurate space weather forecasting. Looking ahead, multi-viewpoint data from upcoming missions like Vigil could further mitigate these challenges, providing a more robust foundation for applying this method while maintaining its operational advantages.

Drag Parameter Estimates

The formulation of the drag parameter γ (see Equation 8) ties γ's uncertainty to errors in the cross-sectional area A (from GCS modelling and Equation 3) and mass M. A notable distinction between the DBM and MoDBM lies in their treatment of solar wind density profiles. The MoDBM employs a refined profile, $\rho_w(r) \propto r^{-2.11}$, which reduces γ at larger heliocentric distances compared to the DBM's simpler r^{-2} dependence. This refinement better aligns with in-situ observations of wind deceleration trends, and is illustrated in Figure 11.

The calculated Γ values for all events in accordance with Equation 12 are within the expected range of $\Gamma = 0.1 - 2$ km^{-1} statistically derived by Vršnak et al. (2013) for magnetic ejecta. This provides validation for the input parameters, suggesting that the chosen methodology aligns with the DBM's formulation. Given that the computation of γ follows a similar approach in both models—despite the MoDBM not yielding a constant value—the same conclusion applies to it as well.

A significant limitation of the DBM is its assumption of a constant γ, which struggles to accurately model CMEs propagating through dynamic solar wind environments. While the MoDBM improves upon this by incorporating a more accurate $\rho_w(r)$, it still does not account for other complexities, such as non-uniform solar wind structures or interactions with transient features. For example, a CME expanding into a high-density solar wind

stream would experience stronger drag forces than predicted by either model, potentially leading to errors in the arrival time. The models can be further improved by accounting for complex processes when they occur, a challenge that could be significantly mitigated with data from ESA's Vigil mission. In particular, the MoDBM's adaptable framework demonstrates potential for refinement, offering a pathway to incorporate additional physical effects. Future improvements could alse focus on refining the drag coefficient c_d, which is currently assumed to be 1 in both models given their simplifying assumptions.

Ambient Solar Wind Speed and Environment Type Estimates

The ambient solar wind speed w is estimated from in-situ measurements near L_1 taken prior to the ICME's (or corresponding shock's) signature being measured. The results are listed in Table 10. This value is directly entered into the DBM, while the MoDBM classifies the ambient solar wind environment type, $w_{\mathrm{med}}^{\mathrm{slow}}$ or $w_{\mathrm{med}}^{\mathrm{fast}}$.

The values for w are extracted from WIND data with an assumed readout error of $\pm 10\,\mathrm{km\,s^{-1}}$. The DBM's use of a single constant value for w in propagation modelling is a significant simplification. The solar wind is inherently dynamic, with variations in speed and density occurring over both time and space. Additionally, the "point-in-time" approach of a single measurement risks misrepresenting spatially or temporally varying conditions regardless. The MoDBM's binary classification partially addresses this by assigning distinct $w(r)$ profiles, but it oversimplifies edge cases where the solar wind transitions between regimes. Thus, misclassifying the ambient environment also introduces systematic biases. For instance, assigning $w_{\mathrm{med}}^{\mathrm{slow}}$ in the case of a ICME entering a fast stream could over-/under-predict drag forces, resulting in arrival time errors.

While the employed event selection criteria in this work (see Section 6.1) aimed to exclude phenomena heavily preconditioning the ambient solar wind, such as prior shocks or ICMEs "clearing" the path for the event of interest, or interacting directly with it (Lugaz et al., 2012), other processes may still alter ρ_w and w profiles. For example, an ICME propagating through less uniform solar wind, featuring e.g. fast streams or current sheet crossings, experiences varying drag forces that cannot be captured by the approach chosen in this work.

This sensitivity underscores the need for real-time solar wind monitoring, as well as incorporating more accurate profiles into the approaches. Vigil will provide similar measurements and could greatly aid in improving forecasts in that regard. To give an alternative, the new generation of the ELlipse Evolution model based on HI observations (ELEvoHI) model (Hinterreiter et al., 2021) describes a drag force dependent on time and spatial dimensions along the CME front, more adaptable to these processes. Moreover, it could make use of future Vigil data, which will also feature a HI (see Section 4.1).

8.4 Forecasted ICME Arrival Times and Propagation Modelling

The ICME arrival time predictions derived from the DBM and MoDBM exhibit varying degrees of accuracy when compared to in-situ measurements. As listed in Table 11 and Table 12, and visualised in Figure 34, both models achieved comparable mean absolute errors of 3.73 h (DBM) and 3.84 h (MoDBM), with root mean square errors of 4.00 h and 5.13 h, respectively.

Table 11: ICME arrival time (AT) prediction results from the propagation modelling with the DBM and the MoDBM together with the real arrival times measured in-situ as reported by Kay and Gopalswamy (2017).

ID	$AT_{in-situ}$ y/m/d:hm	$AT_{DBM} - AT_{in-situ}$ h:m	$AT_{MoDBM} - AT_{in-situ}$ h:m
15	2011/09/17:1535	−2:44	−0:46
31	2012/10/08:1800	+4:19	+1:00
34	2012/11/24:1200	−5:37	−9:55
36	2013/03/17:1500	−4:27	−2:30
37	2013/04/14:1700	−1:33	+5:01

These results strongly improve upon the 12.9 h reported on average for GCS+DBM implementations (Shi et al., 2015), as well as the 12 h as a rough average when forecasting from a single viewpoint[13]. Most notably, they are also far more accurate than the mean absolute error benchmark of 9.8 ± 2.0 h established for many different forecasting approaches (Vourlidas et al., 2019). The small root mean squared errors also reflect the controlled environment, e.g. due to the event selection criteria (see Section 6), which minimised confounding factors such as possible misinterpretation of the events true nature or CME-CME interactions. The indirect influence of selecting 'clean' events on the results should not be underestimated, as for example (Shi et al., 2015) feature a number of events violating Criterion 2 of the event selection process used in this work, namely their event IDs 3, 6, 8, 9 and 13.

Table 12: Statistical evaluation of ICME arrival-time prediction errors in Table 11 from the DBM and MoDBM. Metrics include the mean absolute error (MAE), mean error (ME), and root mean square error (RMSE), expressed in hours. Negative values of ME indicate that the models, on average, predict ICME arrivals earlier than observed in-situ.

Model	MAE h	ME h	RMSE h
DBM	3.73	−2.01	4.00
MoDBM	3.84	−1.43	5.13

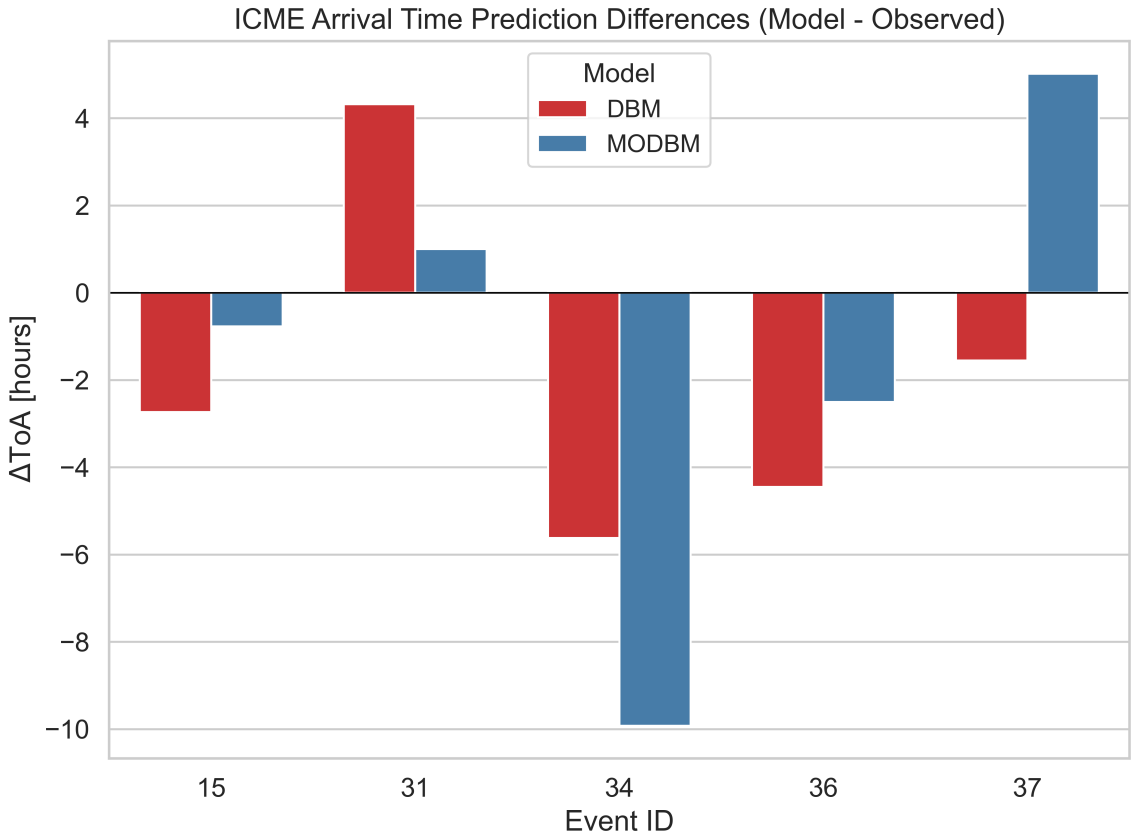

Figure 34: The bar plot illustrates the differences in ICME time of arrival (ΔToA) predictions between the DBM and the MoDBM compared to in-situ observations as reported by Kay and Gopalswamy (2017). Positive values indicate a later predicted arrival compared to observations, while negative values signify an earlier predicted arrival. The results demonstrate the varying accuracy of both models across different events, with the MoDBM exhibiting a slightly larger variance overall.

Validating In-Situ ToA Measurements Against Literature

To obtain the real ToAs for the ICME events, high resolution in-situ measurements from the WIND spacecraft shifted to the bow-shock nose were examined, similar to those presented in Figure 7. Cross-validation with the ToAs derived by Kay and Gopalswamy (2017) confirmed the robustness of the WIND measurements, with only small differences in the determined arrival time of < 10 min for all events. Since the authors considered both data from the WIND and ACE missions, their measurements are adopted here for higher accuracy and are listed in Table 11. It should be noted that the inherent limitation of single-point in-situ measurements—only capturing a very small, localised and potentially not representative part of the ICME—remains a fundamental uncertainty.

Model Runtime, Performance and Event-Specific Discrepancies

The MoDBM employs numerical integration with a fine 1-second time step to solve its system of differential equations as detailed in Section 7.4.2, a process that is typically associated with significantly higher computational demands. However, leveraging an optimised solver enables remarkably efficient execution. In the current implementation, the MoDBM completes its simulations in under a second per event on standard desktop/laptop hardware. The DBM, benefiting from its analytical closed-form solution, requires negligible computation time (< 0.1 seconds), resulting in a combined runtime of less than one second for both models. This also demonstrates the practicality of both approaches for operational use, and even for probabilistic ensemble modelling scenarios (e.g. Dumbović et al. (2018)) requiring rapid computation times.
The DBM systematically underestimated arrival times, yielding a negative mean error value, while the MoDBM showed a reduced bias in that regard. This trend is reversed for event-based deviations: the MoDBM predicted event ID 37 5.02 h later than observed, whereas the DBM underestimated it by -1.55 h. Event ID 37 featured the highest α value (51°) in the GCS reconstructions (see Table 8), amplifying errors in drag force calculations due to the non-linear dependence on $\tan(\alpha)$ in Equation 3. Similarly, events ID 34 and 36, which lacked clear flux-rope signatures in coronagraph images (see Figure 30), produced the largest errors (nearly 10 h for MoDBM), underscoring the sensitivity of both models to the precision of the reconstructions.

Impact of Solar Wind and Drag Parametrisation

The MoDBM's incorporation of a more accurate radial solar wind density profile $\rho_w(r)$ improved physical realism but introduced ambiguity in edge cases. For event ID 36, where the measured ambient solar wind speed of 420 km s^{-1} lay between the MoDBM's predefined slow and fast regimes, an error of only -2.5 h was produced, which would have been significantly higher if $w_{\text{med}}^{\text{fast}}$ had been chosen. This case shows that observing the trend (described in Section 7.4.1) rather than just a single or averaged measurements taken immediately before the ICME signature is helpful in selecting the appropriate solar wind regime. By contrast, the DBM's assumption of constant Γ simplified computations but failed to capture deceleration effects in variable solar wind conditions, as seen in the case of event ID 31 in Figure 33(a), where the DBM predicts a much later ToA than the MoDBM and is less accurate in doing so.

Implications for Operational Forecasting

The results demonstrate the immense potential of stereoscopic GCS reconstructions coupled with drag-based models for operational forecasting. The MoDBM's marginally higher mean absolute error compared to the DBM suggests that increased physical

precision does not universally guarantee improved accuracy, particularly when input parameters (e.g., GCS parameters) are uncertain. However, the MoDBM framework provides a flexible foundation for integrating future advancements. One example of such an advancement describing/predicting the ambient solar wind speed more accurately throughout the heliosphere could be the widely adopted Wang-Sheeley-Arge model (Arge and Pizzo, 2000).

Data from the upcoming Vigil mission can help overcome key limitations by enabling continuous multi-viewpoint observations and further improving the accuracy of GCS reconstructions. Enhanced solar wind monitoring at L_5 can refine the $w(r)$ and $\rho_w(r)$ profiles while also allowing for the incorporation of more complex processes into the models. Utilising more accurate real-time solar wind forecasts, which future Vigil data might also provide, can address the current limitation of single-point measurements. Finally, these advancements, along with the already high accuracy of the developed approaches, provides a strong foundation for a reliable operational method to forecast Earthward-directed CMEs, especially when combined with data from the Vigil mission.

9 Conclusion and Outlook

This work developed and evaluated combined frameworks for CME reconstruction and ICME arrival-time forecasting, integrating multi-viewpoint coronagraph observations with drag-based propagation models, demonstrating their suitability for use with future coronagraph data from ESA's Vigil mission. Through systematic analysis of five events specifically selected to isolate model limitations from event-based complexities, the results demonstrate significant improvements in ICME forecasting accuracy over established benchmarks and similar approaches alike. Additionally, the extended analyses underscored how important multi-perspective observations are in decreasing the likelihood of misinterpreting more complex events, thus reinforcing the operational value of the additional perspective the future ESA Vigil mission will provide at L_5.

Key achievements include:

- Introduction of the MoDBM, incorporating updated radial solar wind density profiles and distinct ambient wind speed regimes, demonstrating adaptability to emerging scientific insights while retaining computational efficiency.
- Development and implementation of an integrated workflow combining multi-viewpoint GCS reconstruction with drag-based propagation models, in line with the expected data usage for ESA's Vigil mission.
- Development of event selection criteria that distinguish model limitations from event-specific complexities, enabling a controlled evaluation of forecasting accuracy for isolated CME-ICME pairs.
- Demonstration and validation of the reconstruction-propagation approaches through detailed analysis of five well-constrained events, achieving mean absolute arrival-time errors of approximately 3.7–3.8 h. This marks a notable advancement compared to traditional single-viewpoint methodologies, and clearly surpasses the previously established barrier of 9.8 ± 2.0 h (Vourlidas et al., 2019), highlighting how incorporating data from additional perspective, such as from ESA's Vigil mission, could further enhance forecasting reliability.

The comparable accuracy of the DBM and MoDBM underscores the potential of drag-based approaches while revealing shared limitations. Both models exhibit systematic early arrival biases, suggesting challenges in capturing initial velocities or acceleration/deceleration trends. While the MoDBM's refined solar wind density profile improved physical realism, its sensitivity to manual slow/fast solar wind regime classification introduces some limitation. Future implementations could integrate real-time solar wind predictions like the Wang-Sheeley-Arge (WSA) model (Arge and Pizzo, 2000),

eliminating the need for oversimplified wind profiles, specifically in the case of the DBM. Such integration would not only enhance physical accuracy but also overcome the operational limitation of relying on solar wind speed measurements taken only shortly before ICME arrival near Earth, making the framework truly usable in real-time forecasting scenarios.

A comprehensive error propagation analysis of the GCS parameter space could quantify interdependencies between geometric parameters and their impact on propagation modelling, e.g. through velocity estimates. Alternative reconstruction approaches, such as the 2D flattening cone DBM (Dumbović et al., 2021), may reduce impact of these uncertainties, and could explore the capabilities of incorporating non-self-similar expansion dynamics. Current efforts that could be of interest here are, for example, attempts to automate the application of the GCS model, with the ultimate goal of reducing subjectivity within the fitting process.

The framework's adaptability extends beyond reconstructions. Comparative studies with empirical (Paouris et al., 2021), MHD (Millward et al., 2013), or HI-based models (Hinterreiter et al., 2021) could identify specific areas for improvement. The success of HI observations in tracking CME fronts highlights opportunities to integrate Vigil's future HI data for real-time trajectory updates—a capability not yet explored in this work.

The methodology described here could alternatively be used to systematically study whether the models predict an ICME to 'hit' or 'miss' Earth, a parameter which can be of high interest (Vourlidas et al., 2019). This could refine assessments of CME orientation accuracy and deflection effects (Kay et al., 2016).

Finally, the established dataset of isolated CME-ICME pairs can be extended easily through applying the defined event selection criteria, and, moreover, function as a baseline for evaluating model performance in controlled conditions. Future studies may use it to compare models, as well as isolate model limitations from common event-based complexities.

10 Bibliography

Acuña, M., Ogilvie, K., Baker, D., Curtis, S., Fairfield, D., and Mish, W. (1995). *The Global Geospace Science Program and its investigations*. Space Science Reviews, 71:5–21.

Andrews, M. D. (2002). *The Front-to-Back Asymmetry of Coronal Emission*. Solar Physics, 208(2):317–324.

Arge, C. N. and Pizzo, V. J. (2000). *Improvement in the prediction of solar wind conditions using near-real time solar magnetic field updates*. Journal of Geophysical Research, 105(A5):10465–10480.

Aschwanden, J. M. (1966). *Physics of the Solar Corona - An Introduction with Problems and Solutions*. Springer-Verlag, Berlin.

Biermann, L. (1951). *Kometenschweife und solare Korpuskularstrahlung*. Zeitschrift für Astrophysik, 29:274.

Billings, D. E. (1966). *A guide to the solar corona*. Academic Press, New York.

Bosman, E. (2017). *3-D Modeling of Coronal Mass Ejections with STEREO/SECCHI Data*. Ph.D. dissertation, Georg-August-Universität Göttingen.

Bothmer, V. (2006). *The Solar Atmosphere and Space Weather*. Solar System Update, pages 1–53.

Bothmer, V. and Schwenn, R. (1998). *The structure and origin of magnetic clouds in the solar wind*. *Annales Geophysicae*, 16(1):1–24.

Bothmer, V. and Zhukov, A. (2007). *The Sun as the prime source of space weather*. In Bothmer, V. and Daglis, I. A., editors, *Space Weather - Physics and Effects*, pages 31–102. Springer-Verlag Berlin Heidelberg.

Bougeret, J.-L., Kaiser, M. L., Kellogg, P. J., Manning, R., Goetz, K., Monson, S. J., Monge, N., Friel, L., Meetre, C. A., Perche, C., Sitruk, L., and Hoang, S. (1995). *WAVES: The radio and plasma wave investigation on the wind spacecraft*. Space Science Reviews, 71(1-4):231–263.

Brueckner, G., Howard, R., Koomen, M., Korendyke, C., Michels, D., Moses, J., Socker, D., Dere, K., Lamy, P., Llebaria, A., Bout, M., Schwenn, R., Simnett, G., Bedford, D., and Eyles, C. (1995). *The large angle spectroscopic coronagraph (LASCO)*. Solar Physics, 162:357–402.

Burkepile, J. T., Hundhausen, A. J., Stanger, A. L., St. Cyr, O. C., and Seiden, J. A. (2004). *Role of projection effects on solar coronal mass ejection properties: 1. A study of CMEs associated with limb activity*. Journal of Geophysical Research: Space Physics, 109(A3):A03103.

Burlaga, L., Sittler, E., Mariani, F., and Schwenn, R. (1981). *Magnetic loop behind an interplanetary shock: Voyager, Helios, and IMP 8 observations*. Journal of Geophysical Research, 86(A8):6673–6684.

Burlaga, L. F., Behannon, K. W., and Klein, L. W. (1987). *Compound streams, magnetic clouds, and major geomagnetic storms*. Journal of Geophysical Research: Space Physics, 92(A6):5725–5734.

Burlaga, L. F., Klein, L., Sheeley Jr., N. R., Michels, D. J., Howard, R. A., Koomen, M. J., Schwenn, R., and Rosenbauer, H. (1982). *A magnetic cloud and a coronal mass ejection*. Geophysical Research Letters, 9(12):1317–1320.

Burrell, A. G., Halford, A., Klenzing, J., Stoneback, R. A., Morley, S. K., Annex, A. M., Laundal, K. M., Kellerman, A. C., Stansby, D., and Ma, J. (2018). *Snakes on a Spaceship—An Overview of Python in Heliophysics*. Journal of Geophysical Research: Space Physics, 123(12):10,384–10,402.

Burt, J. and Smith, B. (2012). *Deep Space Climate Observatory: The DSCOVR mission*. In 2012 IEEE Aerospace Conference, pages 1–13.

Cane, H. V. and Richardson, I. G. (2003). *Interplanetary coronal mass ejections in the near-Earth solar wind during 1996–2002*. Journal of Geophysical Research: Space Physics, 108(A4).

Cargill, P. J. (2004). *On the Aerodynamic Drag Force Acting on Interplanetary Coronal Mass Ejections*. Solar Physics, 221(1):135–149.

Carrington, R. C. (1859). *Description of a Singular Appearance seen in the Sun on September 1, 1859*. Monthly Notices of the Royal Astronomical Society, 20:13–15.

Carroll, B. W. and Ostlie, D. A. (2006). *An introduction to modern astrophysics and cosmology*. Pearson.

Chen, J. (1996). *Theory of prominence eruption and propagation: Interplanetary consequences*. Journal of Geophysical Research: Space Physics, 101(A12):27499–27519.

Chen, P. F. (2011). *Coronal Mass Ejections: Models and Their Observational Basis*. Living Reviews in Solar Physics, 8(1):1.

Colaninno, R. C. (2012). *Investigation of the Forces that Govern the Three-Dimensional Propagation and Expansion of Coronal Mass Ejections from Sun to Earth*. Ph.D. dissertation, George Mason University.

Colaninno, R. C. and Vourlidas, A. (2009). *First Determination of the True Mass of Coronal Mass Ejections: A Novel Approach to Using the Two STEREO Viewpoints*. The Astrophysical Journal, 698(1):852–858.

Connelly, J. N., Bizzarro, M., Krot, A. N., Nordlund, Å., Wielandt, D., and Ivanova, M. A. (2012). *The Absolute Chronology and Thermal Processing of Solids in the Solar Protoplanetary Disk*. Science, 338:651–655.

Cremades, H. and Bothmer, V. (2004). *On the three-dimensional configuration of coronal mass ejections*. Astronomy and Astrophysics, 422:307.

Domingo, V., Fleck, B., and Poland, A. I. (1995). *The SOHO Mission: an Overview*. Solar Physics, 162(1-2):1–37.

Droege, W. and Schlickeiser, R. (1986). *Particle Acceleration in Solar Flares*. Astrophysical Journal, 305:909.

Dumbović, M., Čalogović, J., Martinić, K., Vršnak, B., Sudar, D., Temmer, M., and Veronig, A. (2021). *Drag-Based Model (DBM) Tools for Forecast of Coronal Mass Ejection Arrival Time and Speed*. Frontiers in Astronomy and Space Sciences, 8.

Dumbović, M., Čalogović, J., Vršnak, B., Temmer, M., Mays, M. L., Veronig, A., and Piantschitsch, I. (2018). *The Drag-based Ensemble Model (DBEM) for Coronal Mass Ejection Propagation*. The Astrophysical Journal, 854(2):180.

Forbes, T. G. (2000). *A review on the genesis of coronal mass ejections*. Journal of Geophysical Research: Space Physics, 105(A10):23153–23165.

Forstner, J. L. (2024). *GCS in Python*. https://doi.org/10.5281/zenodo.12668802. V0.2.3.

Freeland, S. L. and Handy, B. N. (1998). *Data Analysis with the SolarSoft System*. Solar Physics, 182(2):497–500.

Freiherr von Forstner, J. L. (2020). *Multipoint observations of ICMEs in the inner heliosphere: Forbush decreases and remote sensing*. Ph.D. dissertation, Christian-Albrechts-Universität zu Kiel.

Freiherr von Forstner, J. L., Dumbovi´c, M., Möstl, C., Guo, J., Papaioannou, A., Elftmann, R., Xu, Z., Christoph Terasa, J., Kollhoff, A., Wimmer-Schweingruber,

R. F., Rodríguez-Pacheco, J., Weiss, A. J., Hinterreiter, J., Amerstorfer, T., Bauer, M., Belov, A. V., Abunina, M. A., Horbury, T., Davies, E. E., O´Brien, H., Allen, R. C., Bruce, A. G., Berger, L., Boden, S., Cernuda Cangas, I., Eldrum, S., Espinosa Lara, F., Gómez Herrero, R., Hayes, J. R., Ho, G. C., Kulkarni, S. R., Jeffrey Lees, W., Martín, C., Mason, G. M., Pacheco, D., Prieto Mateo, M., Ravanbakhsh, A., Rodríguez Polo, O., Sánchez Prieto, S., Schlemm, C. E., Seifert, H., Tyagi, K., and Yedla, M. (2021). *Radial evolution of the April 2020 stealth coronal mass ejection between 0.8 and 1 AU - Comparison of Forbush decreases at Solar Orbiter and near the Earth*. Astronomy & Astrophysics, 656:A1.

Garaud, P. (2020). *The Tachocline Revisited*. In Astrophysics and Space Science Proceedings, pages 207–220. Springer International Publishing.

Gloeckler, G., Balsiger, H., Bürgi, A., Bochsler, P., Fisk, L. A., Galvin, A. B., Geiss, J., Gliem, F., Hamilton, D. C., Holzer, T. E., Hovestadt, D., Ipavich, F. M., Kirsch, E., Lundgren, R. A., Ogilvie, K. W., Sheldon, R. B., and Wilken, B. (1995). *The Solar Wind and Suprathermal Ion Composition Investigation on the Wind Spacecraft*. Space Science Reviews, 71(1-4):79–124.

Gopalswamy, N. (2007). *Properties of Interplanetary Coronal Mass Ejections*, pages 145–168. Springer New York, New York, NY.

Gopalswamy, N., Akiyama, S., Yashiro, S., and Mäkelä, P. (2010). *Coronal Mass Ejections from Sunspot and Non-Sunspot Regions*. In Hasan, S. and Rutten, R. J., editors, *Magnetic Coupling between the Interior and Atmosphere of the Sun*, pages 289–307, Berlin, Heidelberg. Springer Berlin Heidelberg.

Gopalswamy, N., Michałek, G., Yashiro, S., Mäkelä, P., Akiyama, S., Xie, H., and Vourlidas, A. (2025). *The SOHO LASCO CME Catalog - Version 2*. arXiv e-prints.

Gosling, J. T. (1990). *Coronal Mass Ejections and Magnetic Flux Ropes in Interplanetary Space*, pages 343–364. American Geophysical Union (AGU).

Harris, C. R., Millman, K. J., van der Walt, S. J., Gommers, R., Virtanen, P., Cournapeau, D., Wieser, E., Taylor, J., Berg, S., Smith, N. J., Kern, R., Picus, M., Hoyer, S., van Kerkwijk, M. H., Brett, M., Haldane, A., del Río, J. F., Wiebe, M., Peterson, P., Gérard-Marchant, P., Sheppard, K., Reddy, T., Weckesser, W., Abbasi, H., Gohlke, C., and Oliphant, T. E. (2020). *Array programming with NumPy*. Nature, 585(7825):357–362.

Hathaway, D. H. (2025). *NASA MSFC Solar Physics Group: Overview and Research*. https://solarscience.msfc.nasa.gov/index.html. Curators: Mitzi Adams and Jessie Duncan. Last accessed: March 2025.

Hinterreiter, J., Amerstorfer, T., Temmer, M., Reiss, M. A., Weiss, A. J., Möstl, C., Barnard, L. A., Pomoell, J., Bauer, M., and Amerstorfer, U. V. (2021). *Drag-Based CME Modeling With Heliospheric Images Incorporating Frontal Deformation: ELEvoHI 2.0*. Space Weather, 19(10).

Howard, R. A., Michels, D. J., Sheeley, N. R., and Koomen, M. (1982). *The observation of a coronal transient directed at earth*. The Astrophysical Journal, 263.

Howard, R. A., Moses, J. D., Vourlidas, A., Newmark, J. S., Socker, D. G., Plunkett, S. P., Korendyke, C. M., Cook, J. W., Hurley, A., Davila, J. M., Thompson, W. T., St Cyr, O. C., Mentzell, E., Mehalick, K., Lemen, J. R., Wuelser, J. P., Duncan, D. W., Tarbell, T. D., Wolfson, C. J., Moore, A., Harrison, R. A., Waltham, N. R., Lang, J., Davis, C. J., Eyles, C. J., Mapson-Menard, H., Simnett, G. M., Halain, J. P., Defise, J. M., Mazy, E., Rochus, P., Mercier, R., Ravet, M. F., Delmotte, F., Auchere, F., Delaboudiniere, J. P., Bothmer, V., Deutsch, W., Wang, D., Rich, N., Cooper, S., Stephens, V., Maahs, G., Baugh, R., McMullin, D., and Carter, T. (2008). *Sun Earth Connection Coronal and Heliospheric Investigation (SECCHI)*. Space Science Reviews, 136(1-4):67–115.

Howard, R. A., Vourlidas, A., and Stenborg, G. (2023). *The evolution of our understanding of coronal mass ejections*. Frontiers in Astronomy and Space Sciences, 10.

Howard, T. A. and Tappin, S. J. (2009). *Interplanetary Coronal Mass Ejections Observed in the Heliosphere: 3. Physical Implications*. Space Science Reviews, 147(1-2):89–110.

Hundhausen, A. J., Sawyer, C. B., House, L., Illing, R. M., and Wagner, W. J. (1984). *Coronal mass ejections observed during the solar maximum mission: Latitude distribution and rate of occurrence*. J. Geophys. Research, 89:2639–2646.

Illing, R. M. E. and Hundhausen, A. J. (1985). *Observation of a coronal transient from 1.2 to 6 solar radii*. Journal of Geophysical Research: Space Physics, 90(A1):275–282.

Jackson, J. D. (1975). *Classical electrodynamics*. New York: Wiley.

Kaiser, M. L., Kucera, T. A., Davila, J. M., St. Cyr, O. C., Guhathakurta, M., and Christian, E. (2008). *The STEREO Mission: An Introduction*. Space Science Reviews, 136(1-4):5–16.

Kay, C. and Gopalswamy, N. (2017). *Using the Coronal Evolution to Successfully Forward Model CMEs' In Situ Magnetic Profiles*. Journal of Geophysical Research: Space Physics, 122(12):11,810–11,834.

Kay, C., Opher, M., Colaninno, R. C., and Vourlidas, A. (2016). *USING ForeCAT DEFLECTIONS AND ROTATIONS TO CONSTRAIN THE EARLY EVOLUTION OF CMEs*. The Astrophysical Journal, 827(1):70.

Kay, C., Opher, M., and Evans, R. M. (2013). *FORECASTING A CORONAL MASS EJECTION'S ALTERED TRAJECTORY: ForeCAT*. The Astrophysical Journal, 775(1):5.

Kay, C. and Palmerio, E. (2024). *Collection, Collation, and Comparison of 3D Coronal CME Reconstructions*. Space Weather, 22(1):e2023SW003796. e2023SW003796 2023SW003796.

Kivelson, M. G. and Russell, C. T. (1995). *Introduction to Space Physics*. Cambridge University Press.

Kouloumvakos, A. (2025). *PyThea: A software package to reconstruct the 3D structure of CMEs and shock waves*. https://doi.org/10.5281/zenodo.14860537. V1.1.0.

Lavraud, B., Liu, Y., Segura, K., He, J., Qin, G., Temmer, M., Vial, J. C., Xiong, M., Davies, J. A., Rouillard, A. P., Pinto, R., Auchère, F., Harrison, R. A., Eyles, C., Gan, W., Lamy, P., Xia, L., Eastwood, J. P., Kong, L., Wang, J., Wimmer-Schweingruber, R. F., Zhang, S., Zong, Q., Soucek, J., An, J., Prech, L., Zhang, A., Rochus, P., Bothmer, V., Janvier, M., Maksimovic, M., Escoubet, C. P., Kilpua, E. K. J., Tappin, J., Vainio, R., Poedts, S., Dunlop, M. W., Savani, N., Gopalswamy, N., Bale, S. D., Li, G., Howard, T., DeForest, C., Webb, D., Lugaz, N., Fuselier, S. A., Dalmasse, K., Tallineau, J., Vranken, D., and Fernández, J. G. (2016). *A small mission concept to the Sun-Earth Lagrangian L5 point for innovative solar, heliospheric and space weather science*. Journal of Atmospheric and Solar-Terrestrial Physics, 146:171–185.

Leblanc, Y., Dulk, G. A., and Bougeret, J. L. (1998). *Tracing the Electron Density from the Corona to 1 au*. Solar Physics, 183:165–180.

Lepping, R. P., Acuña, M. H., Burlaga, L. F., Farrell, W. M., Slavin, J. A., Schatten, K. H., Mariani, F., Ness, N. F., Neubauer, F. M., Whang, Y. C., Byrnes, J. B., Kennon, R. S., Panetta, P. V., Scheifele, J., and Worley, E. M. (1995). *The Wind Magnetic Field Investigation*. Space Science Reviews, 71(1–4):207–229.

Liu, Y. D., Luhmann, J. G., Kajdič, P., Kilpua, E. K., Lugaz, N., Nitta, N. V., Möstl, C., Lavraud, B., Bale, S. D., Farrugia, C. J., and Galvin, A. B. (2014). *Observations of an extreme storm in interplanetary space caused by successive coronal mass ejections*. Nature Communications, 5(1).

Low, B. C. (2001). *Coronal mass ejections, magnetic flux ropes, and solar magnetism*. Journal of Geophysical Research: Space Physics, 106(A11):25141–25163.

Low, B. C., Munro, R. H., and Fisher, R. R. (1982). *The initiation of a coronal transient*. Astrophysical Journal, 254:335–342.

Lugaz, N., Farrugia, C. J., Davies, J. A., Möstl, C., Davis, C. J., Roussev, I. I., and Temmer, M. (2012). *THE DEFLECTION OF THE TWO INTERACTING CORONAL MASS EJECTIONS OF 2010 MAY 23–24 AS REVEALED BY COMBINED IN SITU MEASUREMENTS AND HELIOSPHERIC IMAGING*. The Astrophysical Journal, 759(1):68.

Lyot, B. (1939). *The study of the solar corona and prominences without eclipses (George Darwin Lecture, 1939)*. Monthly Notices of the Royal Astronomical Society, 99:580.

Mays, M. L., Thompson, B. J., Jian, L. K., Colaninno, R. C., Odstrcil, D., Möstl, C., Temmer, M., Savani, N. P., Collinson, G., Taktakishvili, A., MacNeice, P. J., and Zheng, Y. (2015). PROPAGATION OF THE 2014 JANUARY 7 CME AND RESULTING GEOMAGNETIC NON-EVENT. The Astrophysical Journal, 812(2):145.

Millward, G., Biesecker, D., Pizzo, V., and de Koning, C. A. (2013). *An operational software tool for the analysis of coronagraph images: Determining CME parameters for input into the WSA-Enlil heliospheric model*. Space Weather, 11(2):57–68.

Mrotzek, N. (2019). *Analysis of Coronal Mass Ejection Kinematics and Dependencies on Source Region Properties*. Ph.D. dissertation, Georg-August-Universität Göttingen.

NASA (2005). *Wind Probe*. https://commons.wikimedia.org/wiki/File:Wind_probe.jpg. Public domain image from NASA via Wikimedia Commons.

Paouris, E., Vourlidas, A., Papaioannou, A., and Anastasiadis, A. (2021). *The CME arrival prediction with the Effective Acceleration Model: Further testing with heliospheric imaging observations*. In EGU General Assembly Conference Abstracts, EGU General Assembly Conference Abstracts, pages EGU21–10254.

Parker, E. N. (1958). *Dynamics of the Interplanetary Gas and Magnetic Fields.* Astrophysical Journal, 128:664.

Pluta, A. (2018). *White-Light Mass Determination and Geometrical Modelling of Coronal Mass Ejections*. Ph.D. dissertation, Georg-August-Universität Göttingen.

Pluta, A., Mrotzek, N., Vourlidas, A., Bothmer, V., and Savani, N. (2018). *Combined geometrical modelling and white-light mass determination of coronal mass ejections*. Astronomy & Astrophysics, 623.

Raychaudhuri, P. (2004). *Variability of Coronal Mass Ejections*. Proceedings of the International Astronomical Union, 2004(IAUS226):211–212.

Richard, R. L., El-Alaoui, M., Ashour-Abdalla, M., and Walker, R. J. (2002). *Interplanetary magnetic field control of the entry of solar energetic particles into the magnetosphere*. Journal of Geophysical Research (Space Physics), 107(A8):1184.

Richardson, I. and Cane, H. (2024). *Near-Earth Interplanetary Coronal Mass Ejections Since January 1996*. Harvard Dataverse. https://doi.org/10.7910/DVN/C2MHTH. V2.

Richardson, I. G. and Cane, H. V. (2010). *Near-Earth Interplanetary Coronal Mass Ejections During Solar Cycle 23 (1996 - 2009): Catalog and Summary of Properties*. Solar Physics, 264(1):189–237.

Schmidt, W. and Bothmer, V. (1996). Stereoscopic viewing of solar coronal and interplanetary activity. Advances in Space Research, 17(4):369–376. Solar Flare, Coronal and Heliospheric Dynamics.

Schwabe, H. (1844). *Sonnenbeobachtungen im Jahre 1843. Von Herrn Hofrath Schwabe in Dessau*. Astronomische Nachrichten, 21(15):233.

Schwenn, R. (1990). *Large-Scale Structure of the Interplanetary Medium*. In Schwenn, R. and Marsch, E., editors, Physics of the Inner Heliosphere I: Large-Scale Phenomena., page 99. Springer-Verlag Berlin Heidelberg New York.

Schwenn, R. (2006). *Space Weather: The Solar Perspective*. Living Reviews in Solar Physics, 3(1):2.

Sheeley, N. R., Howard, R. A., Koomen, M., Michels, D. J., Schwenn, R., Mühlhäuser, K.-H., and Rosenbauer, H. (1985). *Coronal mass ejections and interplanetary shocks*. Journal of Geophysical Research, 90:163–175.

Shi, T., Wang, Y., Wan, L., Cheng, X., Ding, M., and Zhang, J. (2015). *PREDICTING THE ARRIVAL TIME OF CORONAL MASS EJECTIONS WITH THE GRADUATED CYLINDRICAL SHELL AND DRAG FORCE MODEL*. The Astrophysical Journal, 806(2):271.

Shibata, K. and Magara, T. (2011). *Solar Flares: Magnetohydrodynamic Processes*. Living Reviews in Solar Physics, 8(1):6.

Shibata, K., Masuda, S., Shimojo, M., Hara, H., Yokoyama, T., Tsuneta, S., Kosugi, T., and Ogawara, Y. (1995). *Hot-Plasma Ejections Associated with Compact-Loop Solar Flares*. The Astrophysical Journal, 451(2):L83.

Siscoe, G., Bothmer, V., and Daglis, I. (2007). *Space weather forecasting historically viewed through the lens of meteorology*. In Bothmer, V. and Daglis, I. A., editors, *Space Weather - Physics and Effects*, pages 5–30. Springer-Verlag Berlin Heidelberg.

Stix, M. (2004). *The Sun : An Introduction*. Springer-Verlag Berlin Heidelberg New York. Also Astronomy and Astrophysics Library.

Stone, E. C., Frandsen, A. M., Mewaldt, R. A., Christian, E. R., Margolies, D., Ormes, J. F., and Snow, F. (1998). *The Advanced Composition Explorer*. Space Science Reviews, 86:1–22.

The SunPy Community, Barnes, W. T., Bobra, M. G., Christe, S. D., Freij, N., Hayes, L. A., Ireland, J., Mumford, S., Perez-Suarez, D., Ryan, D. F., Shih, A. Y., Chanda, P., Glogowski, K., Hewett, R., Hughitt, V. K., Hill, A., Hiware, K., Inglis, A., Kirk, M. S. F., Konge, S., Mason, J. P., Maloney, S. A., Murray, S. A., Panda, A., Park, J., Pereira, T. M. D., Reardon, K., Savage, S., Sipőcz, B. M., Stansby, D., Jain, Y., Taylor, G., Yadav, T., Rajul, and Dang, T. K. (2020). *The SunPy Project: Open Source Development and Status of the Version 1.0 Core Package*. The Astrophysical Journal, 890:68–.

Thernisien, A. F. R. (2011). *Implementation of the Graduated Cylindrical Shell Model for the Three-dimensional Reconstruction of Coronal Mass Ejections*. The Astrophysical Journal Supplement, 194(2):33.

Thernisien, A. F. R., Howard, R. A., and Vourlidas, A. (2006). *Modeling of Flux Rope Coronal Mass Ejections*. The Astrophysical Journal, 652(1):763–773.

Thernisien, A. F. R., Vourlidas, A., and Howard, R. A. (2009). *Forward modeling of coronal mass ejections using STEREO/SECCHI data*. Solar Physics, 256:111–130.

Thompson, W. T. (2006). *Coordinate systems for solar image data*. Astronomy and Astrophysics, 449(2):791–803.

Tousey, R. (1973). *The solar corona.* In Space Research Conference, volume 2, pages 713–730.

Venzmer, M. S. and Bothmer, V. (2018). *Solar-wind predictions for the Parker Solar Probe orbit*. Astronomy and Astrophysics, 611:A36.

Verbeke, C., Leila Mays, M., Kay, C., Riley, P., Palmerio, E., Dumbović, M., Mierla, M., Scolini, C., Temmer, M., Paouris, E., Balmaceda, L. A., Cremades, H., and Hinterreiter, J. (2022). *Quantifying errors in 3D CME parameters derived from synthetic data using white-light reconstruction techniques*. Advances in Space Research.

Verbeke, C., Mays, M. L., Temmer, M., Bingham, S., Steenburgh, R., Dumbović, M., Núñez, M., Jian, L. K., Hess, P., Wiegand, C., Taktakishvili, A., and Andries, J. (2019). *Benchmarking CME Arrival Time and Impact: Progress on Metadata, Metrics, and Events*. Space Weather, 17(1):6–26.

von Rosenvinge, T. T., Barbier, L. M., Karsch, J., Liberman, R., Madden, M. P., Nolan, T., Reames, D. V., Ryan, L., Singh, S., Trexel, H., Winkert, G., Mason, G. M., Hamilton, D. C., and Walpole, P. (1995). *The Energetic Particles: Acceleration, Composition, and Transport (EPACT) investigation on the WIND spacecraft*. Space Science Reviews, 71(1-4):155–206.

Vourlidas, A. (2015). *Mission to the Sun-Earth L5 Lagrangian Point: An Optimal Platform for Space Weather Research*. Space Weather, 13(4):197–201.

Vourlidas, A., Patsourakos, S., and Savani, N. (2019). *Predicting the geoeffective properties of coronal mass ejections: current status, open issues and path forward*. Philosophical transactions. Series A, Mathematical, physical, and engineering sciences, 377:20180096.

Vršnak, B., Ruždjak, D., Sudar, D., and Gopalswamy, N. (2004). *Kinematics of coronal mass ejections between 2 and 30 solar radii* - What can be learned about forces governing the eruption?* Astronomy and Astrophysics, 423(2):717–728.

Vršnak, B., Žic, T., Vrbanec, D., Temmer, M., Rollett, T., Möstl, C., Veronig, A., Čalogović, J., Dumbović, M., Lulić, S., Moon, Y. J., and Shanmugaraju, A. (2013). *Propagation of Interplanetary Coronal Mass Ejections: The Drag-Based Model*. Solar Physics, 285(1-2):295–315.

Webb, D. F. and Howard, R. A. (1994). *The solar cycle variation of coronal mass ejections and the solar wind mass flux*. Journal of Geophysical Research, 99(A3):4201–4220.

Webb, D. F. and Hundhausen, A. J. (1987). *Activity Associated with the Solar Origin of Coronal Mass Ejections*. Solar Physics, 108(2):383–401.

Wolf, R. (1856). *Mittheilungen über die Sonnenflecken I*. Astronomische Mitteilungen der Eidgenössischen Sternwarte Zurich, 1:3–13.

Xue, X. H., Wang, C. B., and Dou, X. K. (2005). *An ice-cream cone model for coronal mass ejections*. Journal of Geophysical Research: Space Physics, 110(A8).

Yashiro, S., Gopalswamy, N., Michalek, G., St. Cyr, O. C., Plunkett, S. P., Rich, N. B., and Howard, R. A. (2004). *A catalog of white light coronal mass ejections observed by the SOHO spacecraft*. Journal of Geophysical Research: Space Physics, 109(A7).

Zhao, X. and Dryer, M. (2014). *Current status of CME/shock arrival time prediction*. Space Weather, 12(7):448–469.

Zurbuchen, T. and Richardson, I. (2006). *In-Situ Solar Wind and Magnetic Field Signatures of Interplanetary Coronal Mass Ejections*. Space Science Reviews, 123.

A Appendix

A.1 Data for Estimation of Apex-Directed CME Velocities

Table A1: All observation times at which the GCS model was applied, along with the corresponding derived CME apex heights. The approximate timestamps (in UT) are taken from the COR2 and C2/C3 coronagraphs and might not match perfectly between the instruments. Other model parameters remain consistent with those listed in Table 8 for each event.

ID	Date (UT) y/m/d	Time Stamp (UT) h:m	h_{apex} $\mathrm{R}_{\odot}$
15	2011/09/14	02:39	11.61
		02:54	12.39
		03:24	13.99
		03:54	15.52
31	2012/10/05	06:24	11.5
		06:39	12.06
		06:54	12.95
		07:24	14.85
		07:54	16.52
34	2012/11/20	14:24	11.83
		14:39	12.84
		14:54	13.62
		15:24	15.63
		15:39	16.52
36	2013/03/15	08:24	14.96
		08:39	16.74
		08:54	18.08
37	2013/04/11	09:24	12.39
		09:54	14.13
		10:24	15.69
		10:54	17.45

A.2 Supplementary GCS Model Fits Obtained from 3D Geometric CME Modelling

All images shown here were created with the 'GCS in Python' tool. Image processing and data origin are detailed in Section 7.1.1.

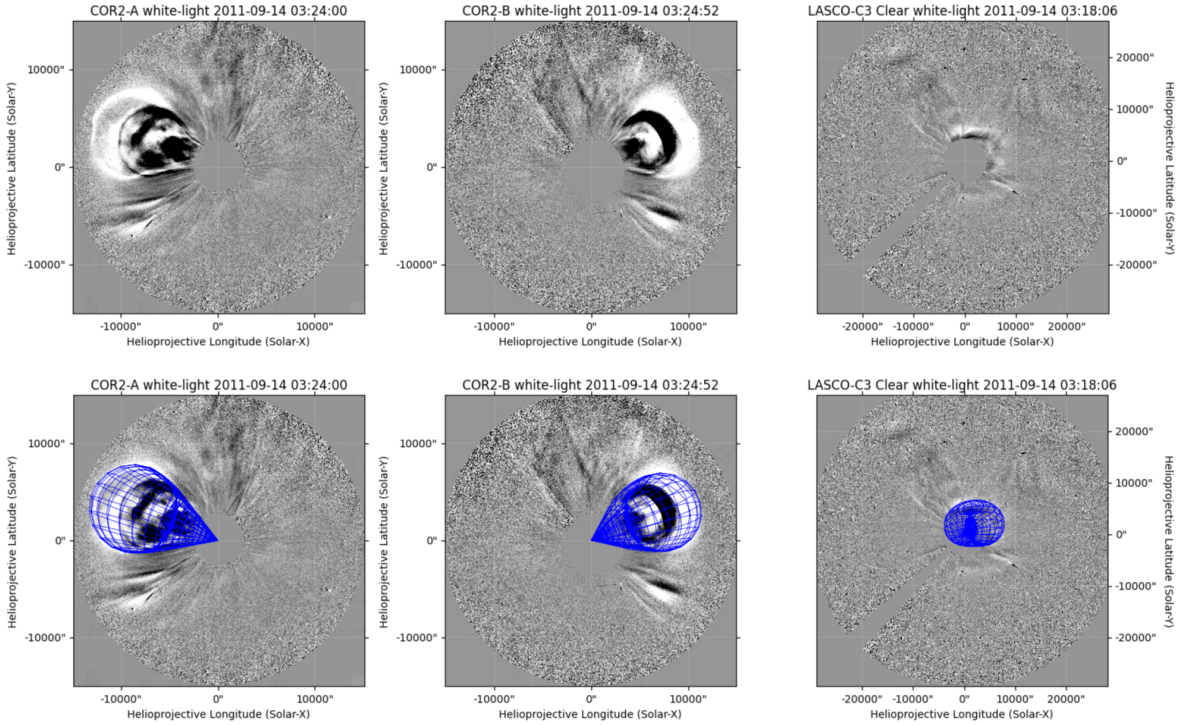

Figure A1: Application of the GCS model to event ID 15, observed simultaneously by (left to right) COR2A, COR2B, and C3 at around 03:24 UT on September 14, 2011. The model fits the CME's leading edge quite well, capturing the overall spatial extension of the CME. The presented images are running-difference images.

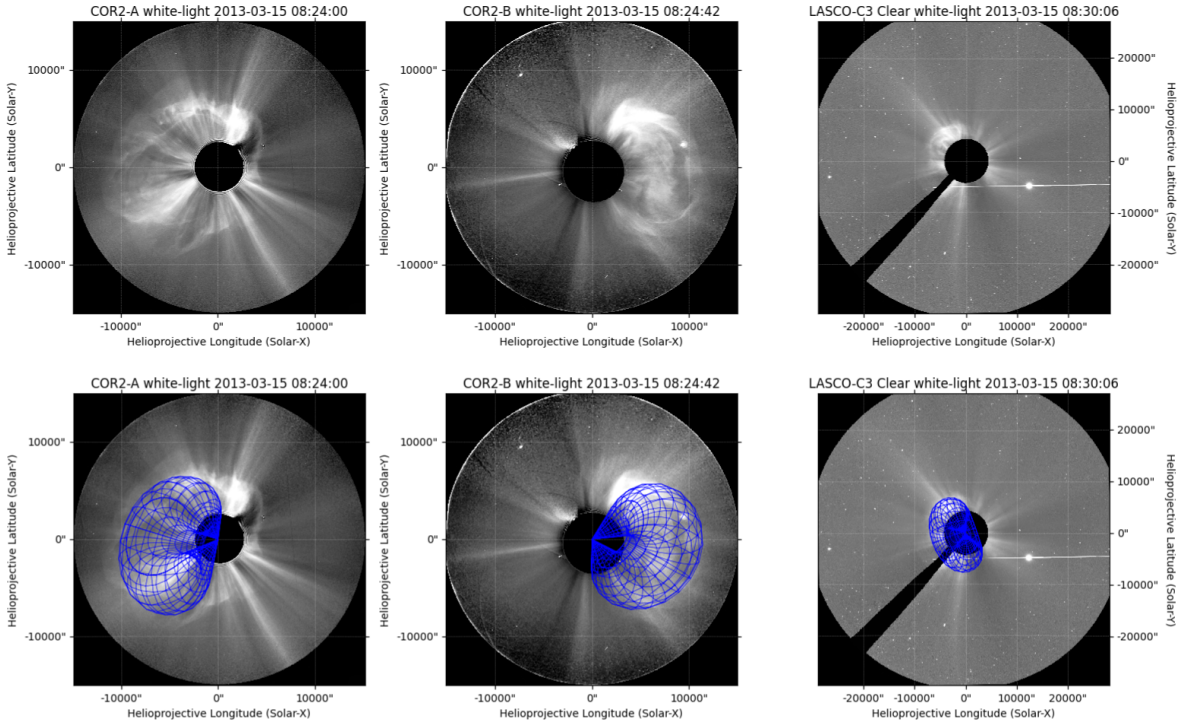

Figure A2: Application of the GCS model to event ID 36, observed simultaneously by (left to right) COR2A, COR2B, and C3 at around 08:24 UT on March 15, 2013. The fitted model excludes the shock front and aligns well with the outer part of the CME's leading edge, but not perfectly everywhere.

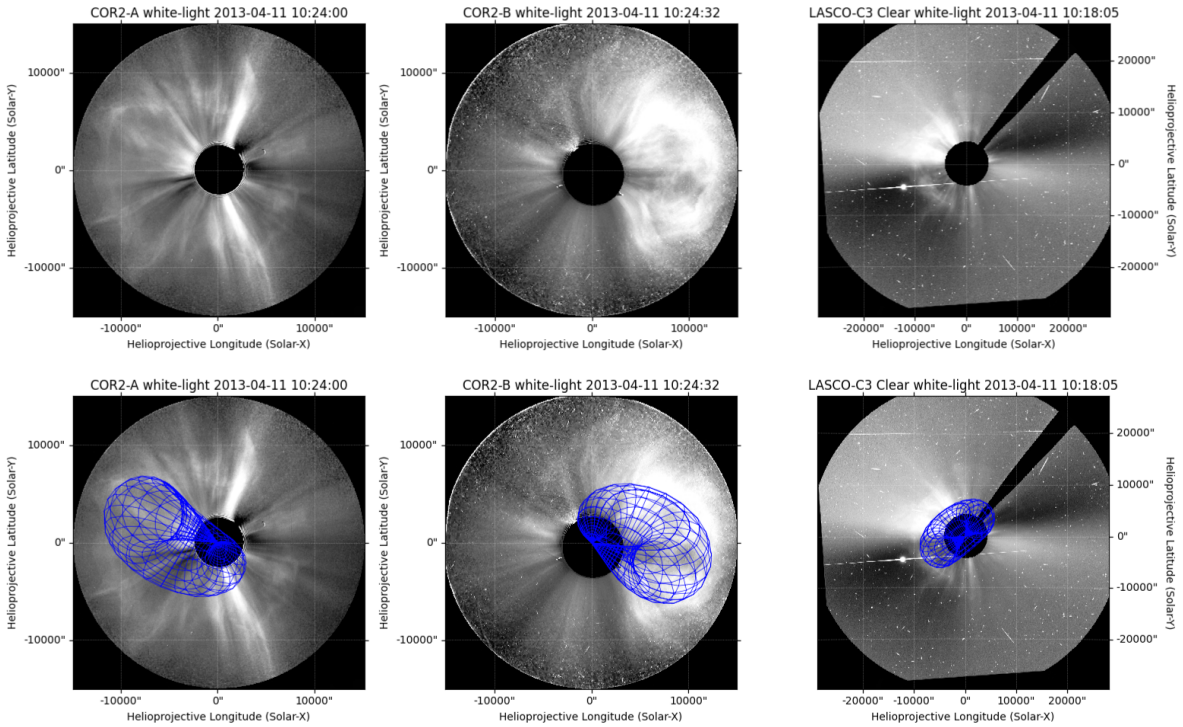

Figure A3: Application of the GCS model to event ID 37, observed simultaneously by (left to right) COR2A, COR2B, and C3 at around 10:24 UT on April 11, 2013. The bright shock front is successfully excluded by the model, yet it struggles to strike a good compromise between the different perspectives.

A.3 Supplementary Height-Time Profiles with Fitted Apex-Directed CME Velocity

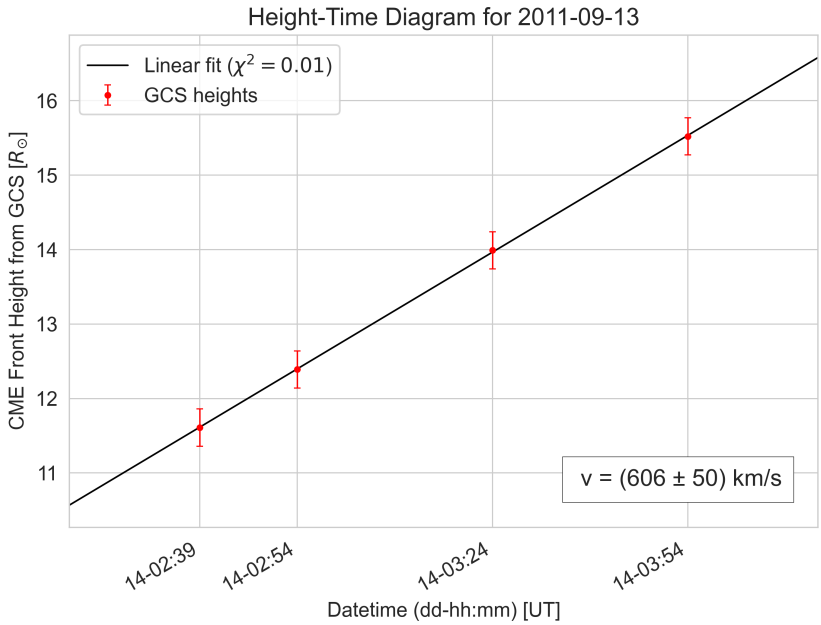

Figure A4: The apex heights of the September 13, 2012 event, modelled via the GCS technique, are plotted against observation times from coronagraph data. A least-squares linear fit, $f(t) = v \cdot t + b$, is applied, where v represents the apex-directed CME velocity. Height uncertainties of $\pm 0.25\,\mathrm{R}_\odot$ are assumed.

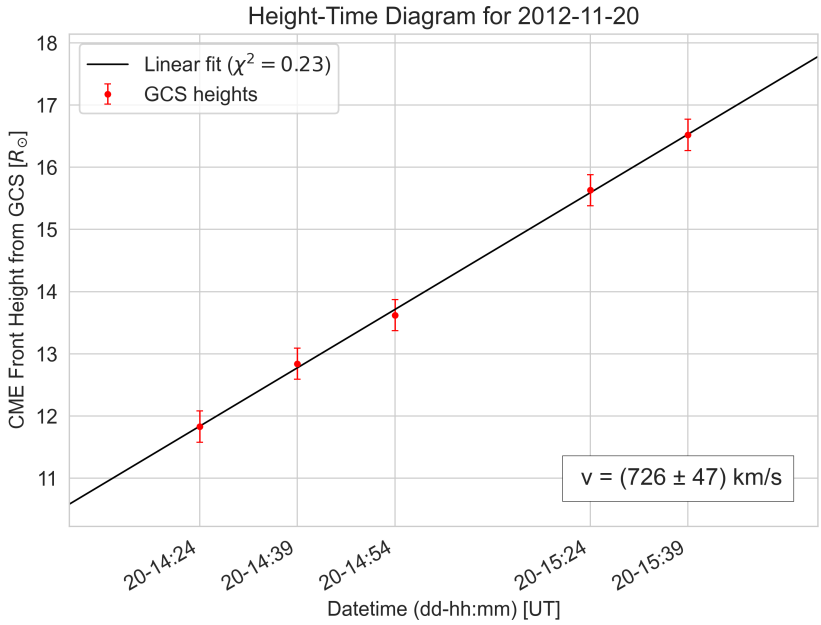

Figure A5: The apex heights of the November 20, 2012 event, modelled via the GCS technique, are plotted against observation times from coronagraph data. A least-squares linear fit, $f(t) = v \cdot t + b$, is applied, where v represents the apex-directed CME velocity. Height uncertainties of $\pm 0.25\,\mathrm{R}_\odot$ are assumed.

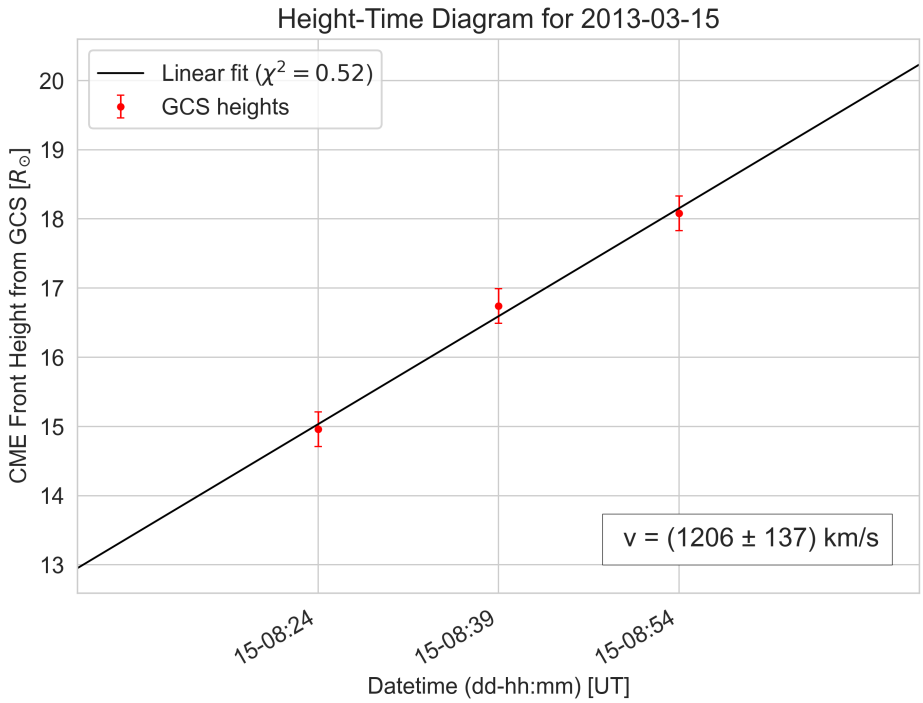

Figure A6: The apex heights of the March 15, 2013 event, modelled via the GCS technique, are plotted against observation times from coronagraph data. A least-squares linear fit, $f(t) = v \cdot t + b$, is applied, where v represents the apex-directed CME velocity. Height uncertainties of $\pm 0.25\,\mathrm{R}_\odot$ are assumed.

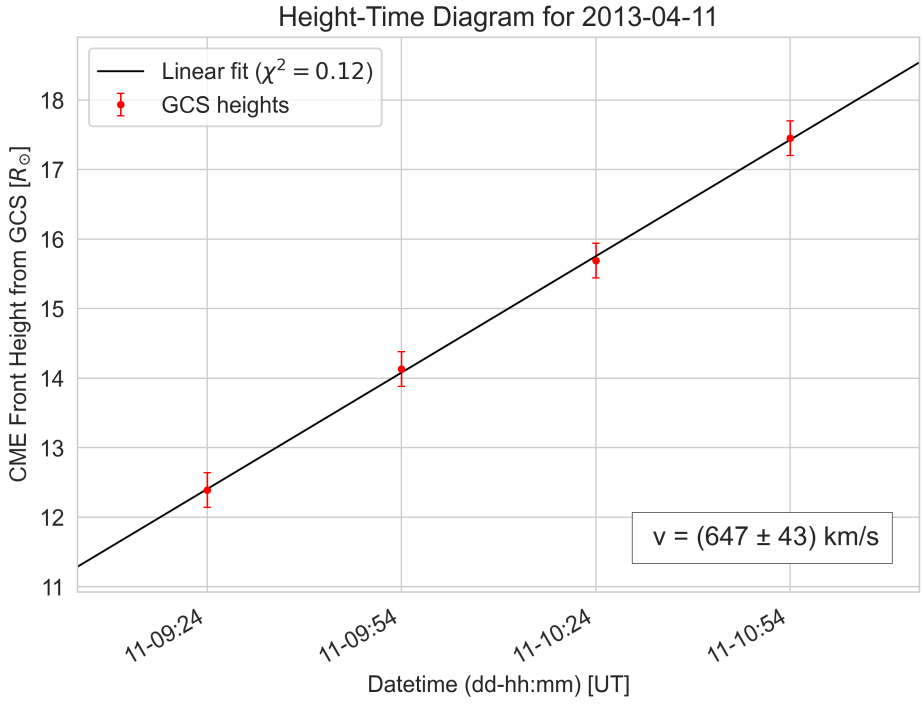

Figure A7: The apex heights of the April 11, 2013 event, modelled via the GCS technique, are plotted against observation times from coronagraph data. A least-squares linear fit, $f(t) = v \cdot t + b$, is applied, where v represents the apex-directed CME velocity. Height uncertainties of $\pm 0.25\,\mathrm{R}_\odot$ are assumed.

A.4 Numerical Computation of the EAR Implemented in Python 3

The implementation was carried out using Python 3.12. It relies on the 'NumPy' library V2.2 (Harris et al., 2020) for efficient numerical computations. Additionally, the 'gcs' package was installed following the official instructions provided in the GitHub repository at https://github.com/johan12345/gcs_python.

```python
# Compute the EAR

import numpy as np
from gcs.geometry import gcs_mesh_rotated

# Define GCS model parameters
alpha = np.radians(45)      # Half-angle
kappa = 0.3                 # Aspect ratio
lat = np.radians(-15)       # Heliographic latitude
lon = np.radians(12.5)      # Stonyhurst longitude
tilt = np.radians(-60)      # Tilt angle

# Define mesh resolution
# (higher value increases accuracy and computational cost)
vertices = 1500

# Generate the GCS mesh
# (accounts for orientation/rotation in 3D space)
big_mesh, _, _ = gcs_mesh_rotated(
    alpha, 1, vertices, vertices, vertices, kappa, lat, lon, tilt
)

# Extract the maximum Z value along the Earthward-directed axis
z_axis_column = ((np.abs(big_mesh[:, 0]) <= .01) &
                 (np.abs(big_mesh[:, 1]) <= .01))
max_z_in_column = np.max(big_mesh[z_axis_column, 2])

# Output the computed EAR
print("EAR =", max_z_in_column)
```

Acknowledgements

Zuallererst möchte ich mich bei meinem Betreuer Dr. Volker Bothmer bedanken, der mir nicht nur eine sehr nahe und konstruktive Betreuung hat zukommen lassen, sondern auch keinerlei Mühen gescheut hat, aufkommende Probleme und Zweifel meinerseits aus dem Weg zu räumen. Ich habe mich nie lange überwältigt gefühlt, und das schätze ich sehr. Ich bin ihm außerdem dankbar für die zahlreichen Erfahrungen, die ich während meines Masters sammeln durfte, was ich nicht für selbstverständlich erachte.

Weiterhin danke ich Prof. Dr. Ansgar Reiners nicht nur dafür, als Zweitgutachter für diese Arbeit zu fungieren, sondern auch dafür, mir mit großer Rücksicht individuelle Möglichkeiten eröffnet zu haben.

Dr. Iulia Chifu danke ich für ihre wertvollen Ratschläge und ihr großes Engagement, welches auch über meine Arbeit hinausging.

Für die Unterstützung bei der Korrektur dieser Arbeit danke ich besonders Dr. Iulia Chifu, Dorian Didier Feisel, Christian Schultz, Johanna Müller und Marie Lotta Maring.

Zudem danke ich meinen Freunden, Eltern, Großeltern und Geschwistern, die mir immer zur Seite standen und mich in heißen Phasen unterstützt und motiviert haben.

Ich möchte meiner Physiklehrerin Dr. Kerstin Reinecke herzlich dafür danken, dass sie mein Interesse an der Physik durch fantastische Unterrichtseinheiten geweckt, und es über mehrere Schuljahre hinweg gefördert hat.

I acknowledge the use of ChatGPT[1], developed by OpenAI, specifically models GPT-4o (gpt-4o-2024-08-06) and o1-preview (o1-preview-2024-09-12), for assisting with writing and testing code, and improving the grammar and style of my writing throughout this thesis.

[1] https://chat.openai.com/chat

Eigenständigkeitserklärung

"Ich versichere, dass ich die Arbeit selbständig und ohne Benutzung anderer als der angegebenen Hilfsmittel angefertigt habe. Alle Stellen, die wörtlich oder sinngemäß aus Veröffentlichungen oder anderen Quellen entnommen sind, sind als solche kenntlich gemacht. Die schriftliche und die elektronische Form der Arbeit stimmen überein. Ich stimme der Überprüfung der Arbeit durch eine Plagiatssoftware zu."

Ort, Datum

Unterschrift